EXPERIMENTAL STUDIES ON METHANE HYDRATE FORMATION

IN UNIFORM POROUS MEDIA

A Dissertation

by

JEREMY JOHN ADAMS

Submitted to the Office of Graduate and Professional Studies of
Texas A&M University
in partial fulfillment of the requirements for the degree of

DOCTOR OF PHILOSOPHY

Chair of Committee,	I. Yucel Akkutlu
Co-Chair of Committee,	George J. Moridis
Committee Members,	Maria A Barrufet
	Scott A. Socolofsky
Head of Department,	Jeff Spath

August 2020

Major Subject: Petroleum Engineering

ABSTRACT*

Methane hydrate is a fascinating physical occurrence of methane and water in solid-state Methane Hydrates have been under investigation for several decades due to its importance in energy and environment, and its various applications in physical sciences and technologies. I developed models in the laboratory to gain insight into (i) secondary hydrate formation in the porous medium, which involves crystallization with hysteresis, and (ii) multi-phase (gas-water) occurrence and flow in the presence of hydrates in the porous medium. In the first part, methane hydrate is formed in a sand pack that undergoes cooling-heating cycles over a range of temperatures. Five cycles are designed so that hysteresis can be observed in the sand pack. Each cycle has a different melting temperature which, leads to varying intensity of temperature relaxation effect on the hysteresis. Evidence of hysteresis is observed in three separate temperature readings of thermocouples. The formation of hydrates is dependent on the thermal cooling rate of the sand pack, and the melting temperature of the previous cycle. A temperature increase is observed in the whole system, and this increase is driven by temperature peaks indicating significant hydrate formation near the thermocouples. These peaks have substantial effects on the entire system. By comparing each cycle's temperature peaks, hysteresis is observed at the temperature readings of the short thermocouple. The same hysteresis pattern follows for the location of the temperature peaks. A new mechanistic

ii

model, following the residual cage theory, is proposed for the prediction of secondary hydrate formation time as a function of the melting temperature.

In the second part, methane hydrate is formed in the sand pack in a transparent x-ray vessel. The gas relative permeability in the presence of methane hydrate is measured using two different steady-state flow experiments: single-phase (gas) flow, multi-phase (water-gas) simultaneous flow. Water and gas co-flow experiments cause issues that complicate the results, while the single-phase gas flow method gives good results. Therefore, in measuring relative permeability in the presence of gas hydrates, single-phase gas flow measurements are recommended. A new empirical equation is given correlating the relative permeability to hydrate saturation.

ACKNOWLEDGMENTS

I would like to thank my committee chair, Dr. Akkutlu, co-chair Dr. Moridis, and my committee members, Dr. Barrufet, and Dr. Socolofsky, for their guidance and support throughout the course of this research.

Thanks also go to my friends and colleagues and the department faculty and staff for making my time at Texas A&M University a great experience.

Finally, thanks to my mother, Lisa Adams, and father Thomas Adams, Ph.D., for their encouragement of my studies.

CONTRIBUTORS AND FUNDING SOURCES

Contributors

This dissertation was supervised by a committee consisting of Dr. Yucel Akkutlu [Advisor], Dr. George Moridis [Co-Advisor], and Dr. Maria Barrufet of the Department of Petroleum Engineering and Dr. Scott Socolofsky of the Department of Civil Engineering.

The first part of the dissertation was completed in the Yuri F. Makogon Gas Hydrate Laboratory located in the Harold Vance Department of Petroleum Engineering using a setup that has previously been developed by Dr. Brice Kim working under co-supervision of Drs. Yucel Akkutlu and Yuri Makogon. I gratefully acknowledge their contribution to my research on the hysteresis.

Lawrence Berkeley National Laboratory in California opened its doors to me during the fall of 2019. It allowed me to access to their facilities to perform my research presented in the second part of my dissertation on the multi-phase flow in a porous medium in the presence of methane hydrate. In particular, I am grateful to Dr. Timothy Kneafsey and Dr. Sharon Borglin of Lawrence Berkeley National Laboratory for offering their time and knowledge during my study. Their support and patience during my visit to the Laboratory have made a significant impact in my thesis. I will never forget this generosity.

Funding Sources

NOMENCLATURE

a_i	Coefficients for Equilibrium Pressure Polynomial
a, b	Coefficients of Redlich-Kwong Equation of State
A_s	Surface Area of Hydrate Particles (m^2)
Δ_T	Internal Temperature Minus External Temperature; (C)
DP/Dt	Derivative of Measured Pressure with Respect to Time (psi/hr)
DQ/Dt	Hydrate Formation Rate (kg/sec)
erf	Error Function
$\tanh$	Hyperbolic Tangent
E_A	Activation Energy (J/mole)
$g(\rho)$	Radial Distribution Function
k_o	Intrinsic Reaction Rate Constant (Mole/(m sec))
k_g	Effective Gas Permeability of the Sand Pack (Darcy)
k_{rg}	Relative Gas Permeability of the Sand Pack (dimensionless)
k_{rw}	Relative Water Permeability of the Sand Pack (dimensionless)
m_W	Mass of Water
m_H	Mass of Hydrate
P	Measured pressure (psi)
P_{CH_4}	Partial pressure of methane in the gas phase (psi)
P_{eq}	Pressure shift of P_{Phase} (psi)

$P_{shift,melt}$	Shift in P_{eq}; (psi)
P_{eq}^*	New equilibrium pressure; (psi)
Q	Volumetric Flow rate; (ml/min)
Q_{sp}	Q function at stationary point
R	Universal gas constant, L.psi / K.mol
S_w	Average Water Saturation in the Sand Pack (dimensionless)
S_H	Average Hydrate Saturation in the Sand Pack (dimensionless)
T	Temperature; (C)
$T_{\max,melt}$	Maximum Melting Temperature; (C)
T_{Phase}	Equilibrium Phase Line Temperature; (C)
$T_{shift\ melt}$	Temperature Shift of T_{Phase}; (C)
T_{eq}^*	New Equilibrium Temperature; (C)
V	Total System Volume, (L)
$\bar{V}$	Molar volume; (L/mole)
v	Molar volume; (L/mole)
Δp	Pressure Difference Between Experimental and Equilibrium Values:(psi)
Δt_{init}	Cycle 1 Formation Time Minus Cycle i Formation Time; (sec)
ρ	Molar Density (1/v)
ρ_{vox}	Voxel Density, (g/cm^3)
$\emptyset_{eq}$	Fugacity Coefficient Inside Hydrate Cage

$\emptyset$	Fugacity Coefficient of Free Gas
γ_w	Activity Coefficient for Hydrate
f^0	Partial Fugacity Coefficient
λ_2	Number of Gas Molecules Per Water Molecule
λ_1	Number of Linked Cavities Per Water Molecule
a_w	λ_1/λ_2
λ	Shape parameter for Brooks' and Cory, and Li and Horne
χ_{A_i}	Fraction of Sight A Not Bonded to Other Sights of Component i
$\Delta^{A_i B_j}$	Association Strength between sight A of component i and Sight B of component j
η	Reduced Density
β	Cross Association Coefficient
A^r	Residual Helmholz
n	Moles
n_i	Moles of Component i
F(V)	Objective Function for Determining Total System Volume

TABLE OF CONTENTS

LIST OF FIGURES

LIST OF TABLES

CHAPTER I *

INTRODUCTION*

1.1 Characteristics of Methane Hydrate

Methane hydrates consist of clathrates of water and methane, which are ice-like in appearance. Other hydrocarbons and gases also form clathrates, but most of the clathrates in nature are formed with methane. Three different types of crystals are formed, depending on the amounts of the water and gas molecules. The most common form in nature is *Structure I Clathrate,* which has a crystal structure of $5^{12}6^2$. The crystal structure forms a cage in which one methane molecule resides. This formation has a set of chemical equations that can be used to show that the water and gas content are not stoichiometric.

The methane hydrate deposits are located mainly on the continental shelf of the oceans, and in the tundra of the far north. Estimates of the amount of methane gas in the form of hydrate deposits in the world are, by conservative estimates, double the current global hydrocarbon reserves, including oil and gas combined; thus, it is of great interest to many countries that have access to methane hydrates to exploit them as an alternative energy resource (Moridis et al., 2009). However, the need to understand the fundamental physics of formation and dissociation in the hydrate-bearing formations is paramount to the natural gas production. Countries with limited energy resources, such as Japan and South Korea, have significant methane hydrate reserves off their coasts. This, then, would allow similar countries--and even those with various

energy resources such as the United States, Russia, and China-- to benefit from methane hydrates.

Just a few methods of gas production have been considered using test wells, laboratory experiments, and numerical simulation models. The production methods are depressurization, thermal dissociation, and chemical dissociation. Thermal dissociation has been discussed in the literature theoretically using numerical simulations and was found to be an inefficient method due to the large volumetric heat capacity values of the water and the rock [Moridis, G. J., Collett, 2009]. Hence, a large amount of energy is needed to increase the temperature of the formation sufficient to destabilize the hydrate. Chemical dissociation is done by injecting specific chemical agents that can reduce the melting temperature of the hydrate, thus dissociating it. But the considered chemicals are expensive, and they only work in the injected area with the required level of chemical concentration. Unfortunately, injection is local, and there will be areas where the chemical cannot reach. The most efficient production method proposed so far is depressurization. This is mainly due to not having to exert or introduce an excessive amount of energy to dissociate the hydrate. Depressurization at the well can be achieved downhole with the submersible pumps that are traditionally used in the oil fields for the removal of water and gas or using for the artificial lifting of the fluids. Another advantage of the depressurization method is that pressure transient is a diffusive phenomenon that can reach far into the reservoir and dissociate the hydrate in a relatively much larger drainage volume. At the same time, the other methods have trouble reaching far into the reservoir. Also as shown in figure 1.1, melting followed by pressure drops
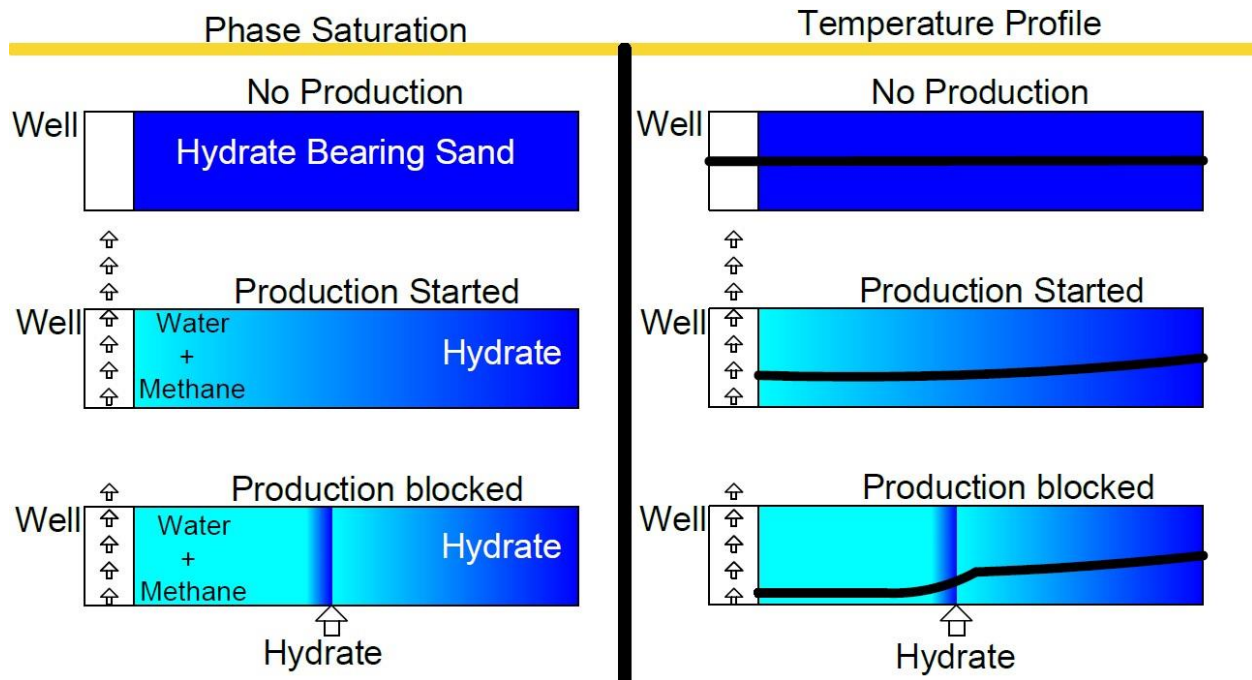
Figure I.1: Phase Saturation on the left and temperature profile on the right.

creates a two-phase flow region with new and improved flow paths that are necessary to transmit

the gas through the formation. A vital disadvantage though to the depressurization is that the

hydrate can easily re-form in the two-phase region in the formation during the production.

Methane hydrate dissociation is endothermic and therefore causes the surrounding area to the

melting interface to cool.

Depending on the rate of depressurization, due to the temperature going back into the hydrate

stability zone, or due to the hydrate stability zone moving to a higher temperature, i.e.,

hysteresis, methane hydrate can re-form. The effects that hysteresis has on the phase diagram can

be seen in Figure I-1. On the far end, even ice can form and combine this with the hydrate re-

formation, the existing flow paths in the reservoir can be blocked, and there is not much that can

be done economically to rectify the issue. Figure I-1 shows the saturation and pressure profiles

during the depressurization method. The diagram clearly shows the hydrate melting zone (or the

interface) and the two-phase region located in between the well and the interface. In my research

presented in this dissertation, the focus will be on this two-phase region, where water-gas co-exist in the presence of hydrate with varying levels of saturations in the formation.

In the past few years, test wells have been drilled into the hydrate-bearing formations, and the production monitored (Moridis et al., 2009). During the production, however, sand was produced along with the gas, which indicated the unconsolidated nature of the formation (Yamamoto et al., 2014). Another issue is the cooling effect that results when producing the hydrate gas using the depressurization method. While it is not observed directly in the field, the laboratory results exist corroborating this effect (McGuire, 1981; Moridis, Kowalsky, & Pruess, 2007; Oyama, Konno, Masuda, & Narita, 2009; Seol & Myshakin, 2011). This result is an effect of the nature of methane hydrate: it generates heat when forming and absorbs heat when melting. Thus, the temperature in the formation in the two-phase region near the wellbore decreases during the production. This cooling can re-form methane hydrate and even freeze the water in the formation (McGuire, 1981). In this chapter, I will describe this cooling effect and how hydrates behave after the initial melting due to depressurization —and, if once the re-formed hydrate is melted again, how that, too, is affected. This cycle can repeat, and it is of practical interest --as well as a scientific curiosity-- to find out whether the hydrate is becoming easier to form, or whether the re-formation conditions stay the same; and if it is forming easier, then what controls this change in behavior. In bulk hydrate formation, an effect has previously been observed in which the formation of the hydrate is easier than that of the initial formation; this was called hysteresis
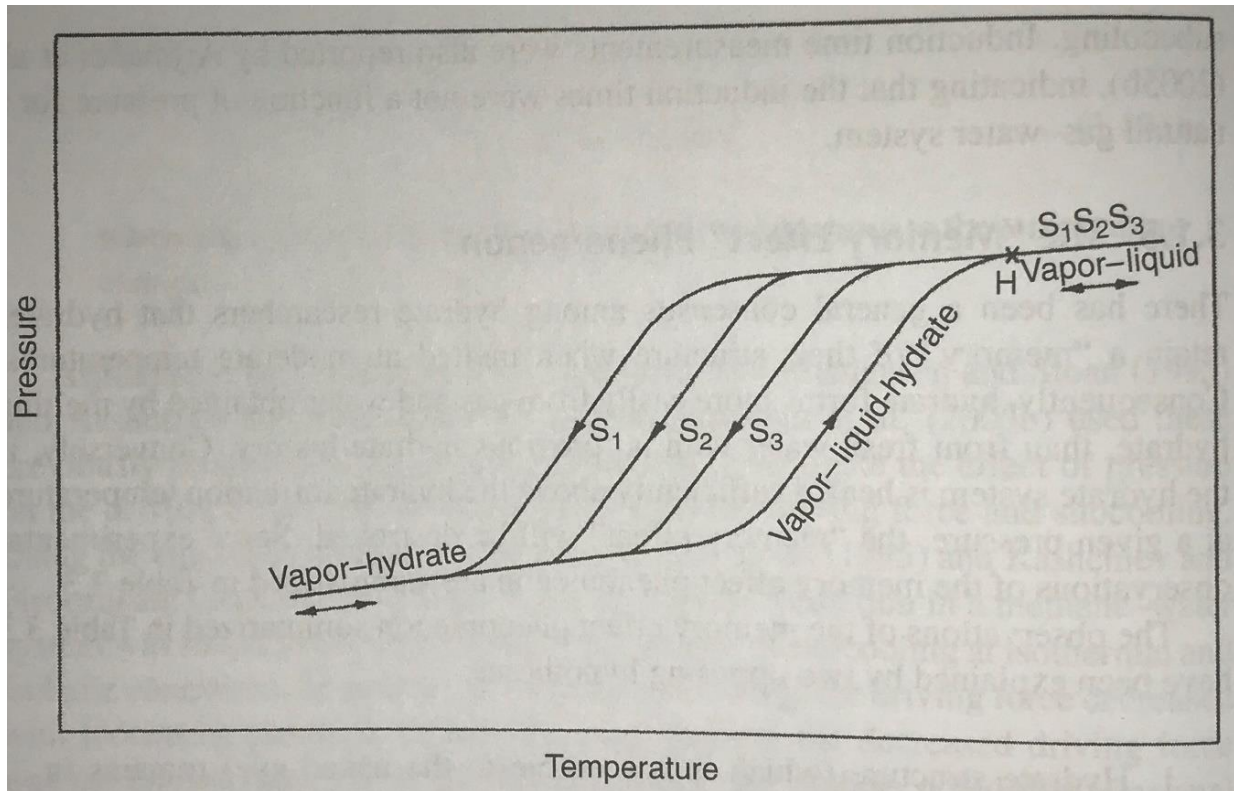
Figure I.2: Hysteresis during three cycles, in a bulk isochoric system. [Sloan Jr, Koh, 2007]. (Lekvam & Ruoff, 1997). But the current scientific knowledge in the case of hydrate formation in the porous medium is limited (Kim & Akkutlu, 2017).

Hysteresis of methane hydrate has been studied in bulk samples extensively (Roger, 2000; Ohmura et al., 2003; Buchanan et al., 2005; Lee, Susilo et al., 2005; Rees et al., 2011;). In most of the cases, the study was completed in a stirred-tank reactor so that the crystallization and melting develop homogeneously, and the heat transfer does not affect the system behavior. The experiments targeting the hysteresis were also seen in systems that have compounds other than methane, thus showing that hysteresis has been observed in many clathrate systems, not just methane, thus strengthening the idea (Ohmura et al., 2003). And another study has used a large time-scale molecular dynamics simulation to describe the hysteresis (Rodger, 2000). Thus, hysteresis is an important feature to capture when there are multiple hydrate forming and melting

cycles. Figure I.2 is an example of how hysteresis affects the phase diagram. Each loop in figure I.2 represents the hydrates getting easier to form, where S1 is the initial formation cycle, and S3 is the last.

A hypothetical example is that the hydrate begins forming in a container, say in 10 minutes, but if one were to melt that same hydrate and form it again under the same cooling rate, the hydrate forms in 8 minutes instead of 10. This means there is a mechanic that reduces the barrier to the hydrate formation. There are two theories on what this mechanic is: one is the memory effect of the water, which is thought to be in the form of partially-melted hydrate cages that form microscopic scale nucleation sites; the other is more gas availability near the nucleation sites in the form of dissolved gas in water. Either of these or both, can be used to explain the hysteresis behavior. In this dissertation, I would like to present an experimental approach that forms and melts methane hydrates in a sand pack under similar cooling rates. The objective is to determine where in the porous medium and when the hydrate forms; and determine if the cooling rate influences the formation time. If there is a difference in the formation time due to cooling rate, and there is a difference in formation time under similar cooling rates, then there are two mechanics that help form hydrates: the mechanics of hysteresis, and the mechanics of cooling rates. We will focus on the former case; a future study will be needed in the latter case. In the final part of Chapter 3, we propose an empirical approach to shift the P-T diagram due to the hysteresis and a reaction modeling approach, including the hysteresis during the reservoir-scale simulation of hydrate gas production.

In the second part of the dissertation, I will focus on gas flow in the two-phase region in the formation shown in Figure I.1 as the quality of natural gas production. I will use the sand pack model in the laboratory for the purpose and measure permeability and saturations of the sand

pack. In reservoir simulation technologies, it is a common practice to capture multi-phase flow dynamics using relative permeability curves.

But before we continue further, let us review the concept of relative permeability as it was introduced in the petroleum engineering literature. Although the theory of single-phase flow based on Darcy law is complete, the theory of multiphase flow is incomplete due to complexities associated with the nature of the problem, i.e., complex boundaries of the pore network and due to the presence of interfaces separating the immiscible fluids. Petroleum engineers avoid these latter difficulties by making a fundamental assumption: during multi-phase flow in porous media, each phase follows its path, obeying its own Darcy law. Then, one can write Darcy's equation for each phase, say the gas phase in a gas-water flow in the x-direction, as follows:

$$q_{g,x} = \frac{k_{gx} A_x \Delta P_g}{\mu_g L} \qquad \text{where} \quad k_{g,x} < k_x \qquad \text{I-1}$$

Here, note that the permeability in the equation is the effective gas permeability, which not only includes the absolute permeability, but also the saturation-dependence of the flow. If the gas saturation is high effective permeability improves, and flow rate for gas also increases proportionally. However, note that the effective permeability value is always less than the
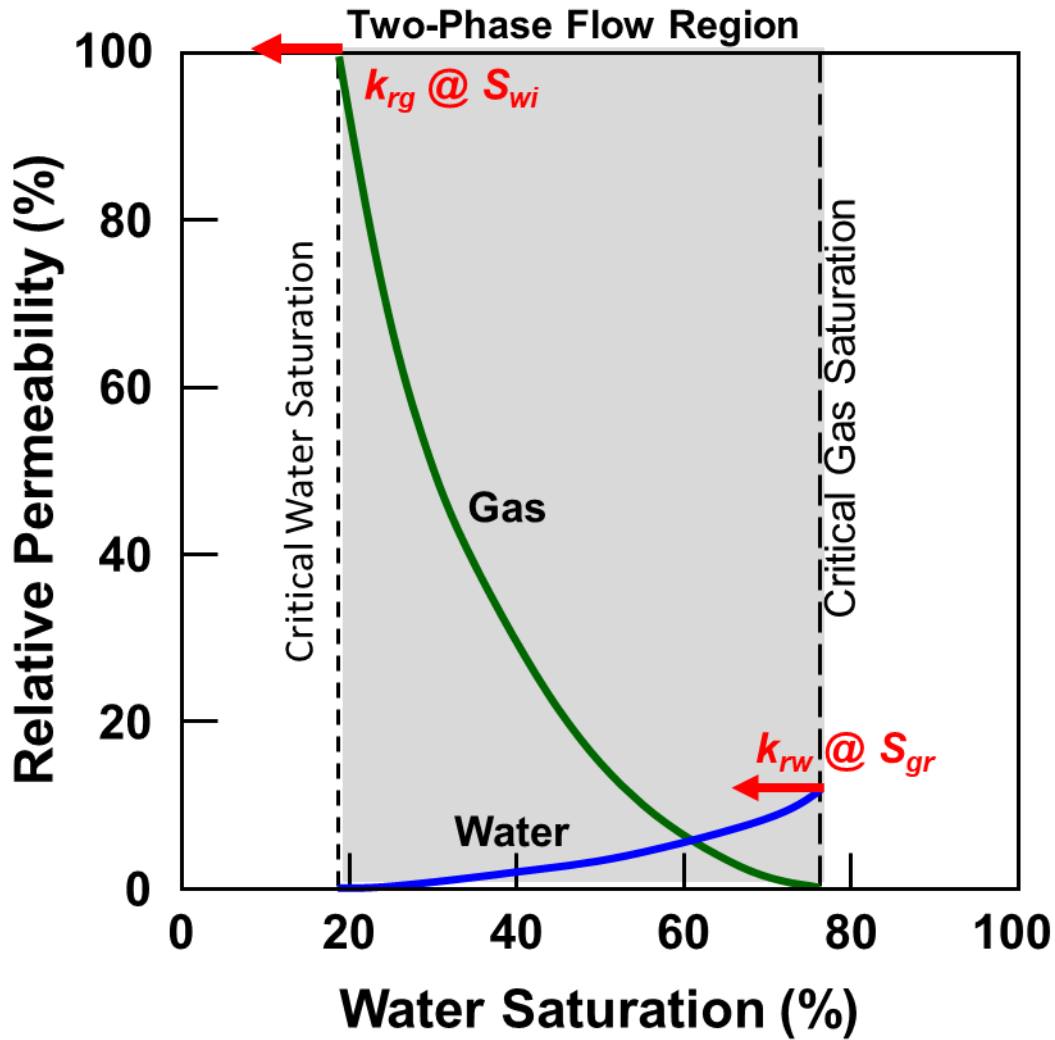
Figure I.3: Typical Relative Permeability Curves.

absolute permeability at Sg=1.0. Petroleum engineers proposed to partition the effective permeability to its two major components:

$$k_{g,x} = k_x \times k_{rg} \qquad\qquad \text{I-2}$$
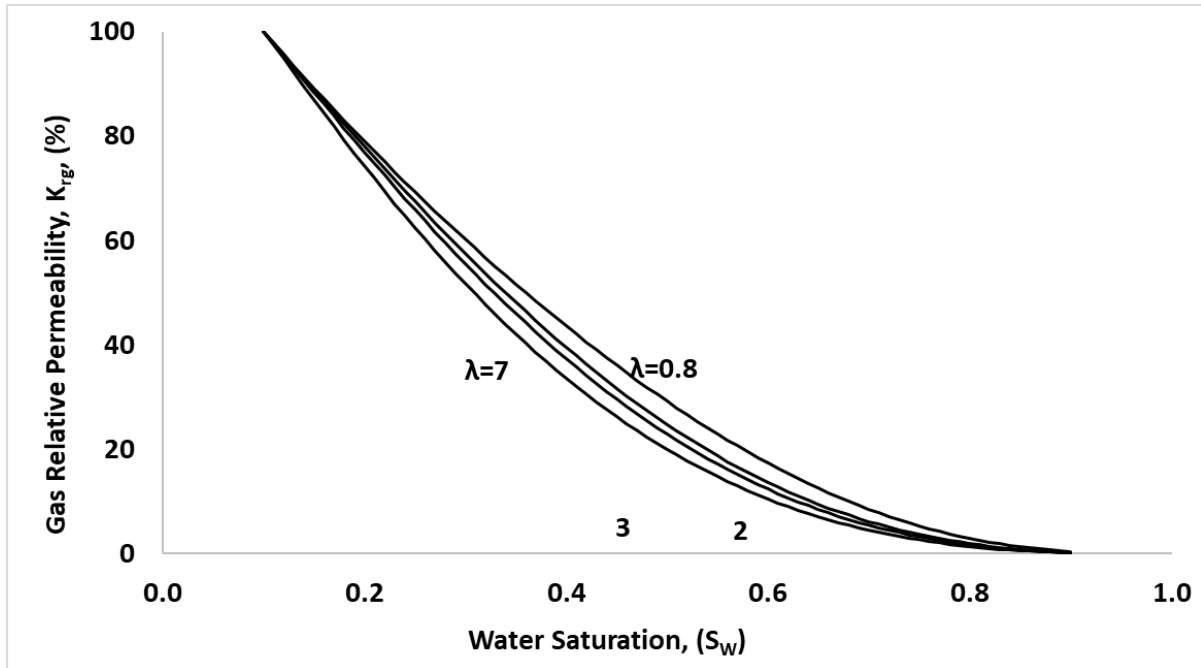
Figure I.4: Brooks and Corey Type curves [Brooks, Corey, 1964].

In this equation, the first parameter on the right-hand-side is the absolute permeability of the rock, and the second parameter is the relative permeability. Inserting this product into Darcy's equation for the gas phase results in:

$$q_{g,x} = \frac{k_x k_{rg} A_x \Delta P_g}{\mu_g L}$$ I-3

In essence, relative permeability becomes a reduction in permeability. The typical form relative permeability takes is seen in Figure I-3. The shaded region represents the mobile region where both water and gas can flow. Outside of these regions is the single-phase region, where the other non-mobile phase is at the irreducible water saturation. The irreducible water/gas saturation is the saturation of the phase where no matter how much of the other phase is flown threw, that phase saturation doesn't change. There are ways to change this irreducible saturation values, but it would be through either chemical or thermal means.

However, the nature of these curves is not well established for the simulation of methane flow and production from the hydrate-bearing formations. The current relative permeability curves are based on correlations developed in the absence of hydrates, and they may not be suitable for the representation of the flow.

Equations I-3 and I-4 and Figure I-4 are the Brooks and Corey correlations for relative permeability of two-phase flow and their corresponding plot for the gas phase. Note that there is a relative permeability equation for each phase; thus, when calculating the flow of the system, each phase must be treated separately using Darcy law and then calculate the total flow.

$$k_{rw} = \left(\frac{S_w - S_{wirr}}{1 - S_{wirr}}\right)^{\frac{2+3\lambda}{\lambda}} \qquad \text{I-3}$$

$$k_{rg} = \left(\frac{1 - S_w}{1 - S_{wirr}}\right)^2 \left[1 - \left(\frac{S_w - S_{wirr}}{1 - S_{wirr}}\right)^{\frac{2+\lambda}{\lambda}}\right] \qquad \text{I-4}$$

λ and S_{wirr} are the two key parameters for fitting the relative permeability curves of the system. S_{wirr} is the irreducible water saturation, and in a gas-water system, one minus its value is the gas saturation at which only the gas flows. This sets the boundaries of the dynamic saturation profile. λ is a shape parameter, which correlates to the grain size distribution and sphericity of the porous media. A value of the shape factor equal to 7.5 corresponds to a pack of glass beads, whereas a value of 7 is for a well-sifted sand pack, and finally, values of 0.7-1.5 for grains with size and sphericity changing significantly within the sample. Another model is the one developed by Li et al. [Li, Kewen, and Roland N. Horne, 2004]. This model was developed using a fractal description of the rock and then translated to the capillary pressure and water saturation along with the shape parameter λ. The maximum and entry capillary pressures were chosen to be quite low since it was sand. There were no measurements of capillary pressure in my study, so an
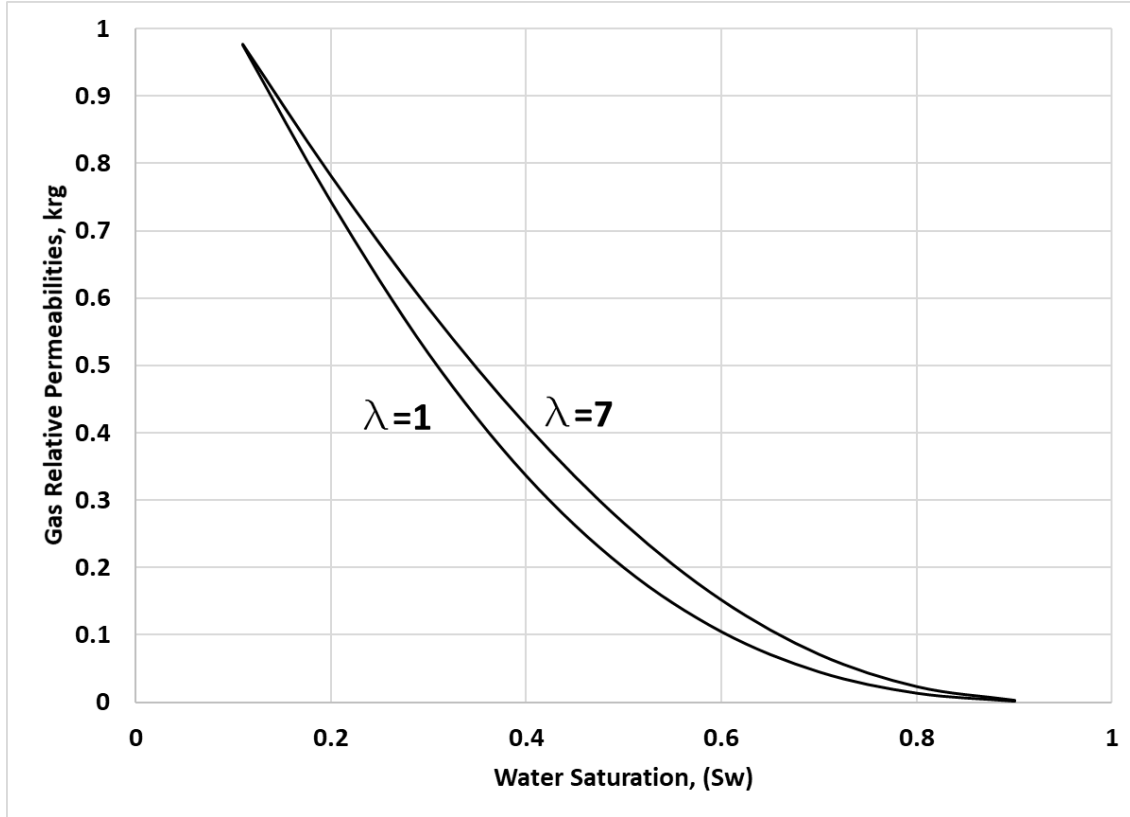
Figure I.5: Li and Horne Type Curves.

estimate had to be used. For this example, 45 MPa and 6 MPa were used for $P_{c,m}$ and P_e, which

came from the paper by Plug and Bruining, [Plug and Bruining, 2007]

$$k_{rw} = \frac{S_{we}^{\frac{2+\lambda}{\lambda}} - \beta^{\frac{2+\lambda}{\lambda}}}{\alpha^{\frac{2+\lambda}{\lambda}} - \beta^{\frac{2+\lambda}{\lambda}}} (S_w^*)^2 \qquad \text{I-5}$$

$$k_{rg} = \frac{\alpha^{\frac{2+\lambda}{\lambda}} - S_{we}^{\frac{2+\lambda}{\lambda}}}{\alpha^{\frac{2+\lambda}{\lambda}} - \beta^{\frac{2+\lambda}{\lambda}}} (1 - S_w^*)^2 \qquad \text{I-6}$$

where

$$S_{we} = P_{c,m}^{-\lambda} - \left[P_{c,m}^{-\lambda} - P_e^{-\lambda}\right] S_w^* \qquad \text{I-7}$$

and

$$S_w^* = \frac{S_w - S_{w,irr}}{1 - S_{w,irr}} \qquad \text{I-8}$$

$$\alpha = P_e^{-\lambda} \qquad \text{I-9}$$

11

$$\beta = P_{c,m}^{-\lambda} \qquad\qquad \textbf{I-10}$$

$$\lambda = 2 - D_f \qquad\qquad \textbf{I-11}$$

Li et al. (2004) model can be reduced to the Brooks and Cory correlations by assuming that $P_{c,m}$ goes to infinity, and this happens when the fractal dimension D_f is two or less. As Figure I.5 shows, the shape is very similar to that of the Brooks' and Corey correlation but has the additional step of calculating the maximum capillary pressure and the entry capillary pressure values.

IN my study, methane hydrate will be formed in a sand pack in the laboratory in multiple temperature stages, ranging from no hydrate at higher temperature to the level of a desired hydrate saturation, when the porous medium is no longer permeable, at a low enough temperature. Both mass balance and x-ray computed tomography (CT) will be used to predict the average saturations in the sand pack. Effective permeability and relative permeability values for gas will be measured at each stage.

To better understand the relative permeability to gas in the presence of methane hydrate, I conducted a series of flow experiments at the Lawrence Berkeley National Laboratory, California. The setup includes a pressure vessel transparent to x-rays so that a CT scanner can be used to image the system while the tests are being conducted. Four tests are conducted to measure the effective permeability of packed sand for gas. The relative gas permeability is predicted using the gas permeability data. The relative permeability to water has large fluctuations; we therefore show only the gas permeability data.

Current methods in the literature for conducting relative permeability measurements in the presence of hydrate vary, from natural hydrate samples and CT scanning (Delli et al., 2014;

Johnson et al.,2011) to measure capillary pressure in a sand pack (Delli et al., 2014, Pini et al., 2013), to using CT scanning in a horizontal vessel and measuring the saturations and differential pressures (Seol et al., 2011, Kneafsey et al., 2010), but all have the same trends controlling hydrate saturations and mitigating its formation during testing. Natural hydrate samples are challenging to perform any experiment on, especially the flow and permeability experiments (Johnson et al., 2011). The flow measurements suffer from non-homogeneous saturations, which creates uncertainties in the permeability calculations since the underlying assumptions are that the saturations are uniform (Honarpour et al., 1988). To get around this problem, the use of uniform sand packs is considered. The sand is packed in such a way that its density variations are not too large so that, when hydrate is formed, its porosity and permeability are uniform. When the hydrate saturation is as uniform as possible, the permeability experiments can be conducted for gas effective permeability. The flowing gas needs to be colder than the equilibrium temperature of hydrate formation. When relative permeability is needed, however, a few additional effects occur: hydrate start to form or melt during the flow if the pressure changes rapidly, and the trick is to keep the hydrate formation rate as slow as possible thus mitigating the effects, though this is easier said than done (Rees et al., 2011). Hydrate when forming causes volume of the capillaries contributing to flow to shrink, thus increasing the capillary pressure of the sand pack. During the hydrate crystallization, changes in the capillary characteristics do not develop uniformly but are driven by the local saturations and flow characteristics (Rees et al., 2011). The capillary pressure developing due to the hydrate formation creates a drive, which forces water in the sand pack to the hydrate rich zones. This causes a no-flow zone for gas by having low-permeability regions that are saturated with hydrate and water. Consequently, the low water saturation or "dry" and high-permeability regions are what is measured during the

13

flow experiments. This does not mean that hydrate relative permeability experiments cannot be done, it just means that new ways of mitigating these local effects need to be found.

CHAPTER II *

EXPERIMENTAL SET UP AND LABORATORY PROCEDURE*

2.1 Phase Equilibria

In Figure II.1, a diagram of the hydrate cell used in the laboratory is shown. The cell is made of stainless steel and has a maximum working pressure of 10,000 psi. The sand is in volume A in the cell. In this region, the cell has three thermocouples and one pressure transducer that records the pressure, P1. Volume B is filled with water, which is used to apply a uniform force to a steel piston (seen as grey and black) to keep the sand compressed. The upper side of the cell in Figure II.1 is made of copper and is used to promote a heat transfer that is similar to the walls. While the copper has much larger thermal conductivity, the thickness is much greater than the walls, so the copper provides a similar heat flow as the steel walls. At the bottom, the plug is stainless steel and is much thinner than its copper counterpart. Not shown are the lines that provide the water and methane gas to the system, and there is a vacuum line that can be added to the system as well.

The first step in running the experiment is to have the ingredients: dry sand that is oven-baked, distilled water, and pure methane. 1,100 ml of the sand is added to volume A in the cylinder from the top, in which the thermocouples are added as well. The thermocouples run through the copper plug into the sand pack, as shown in Figure II.1, in Volume A. They are placed at different locations in the sand pack. A short thermocouple reaches 3 cm into the sand pack and is
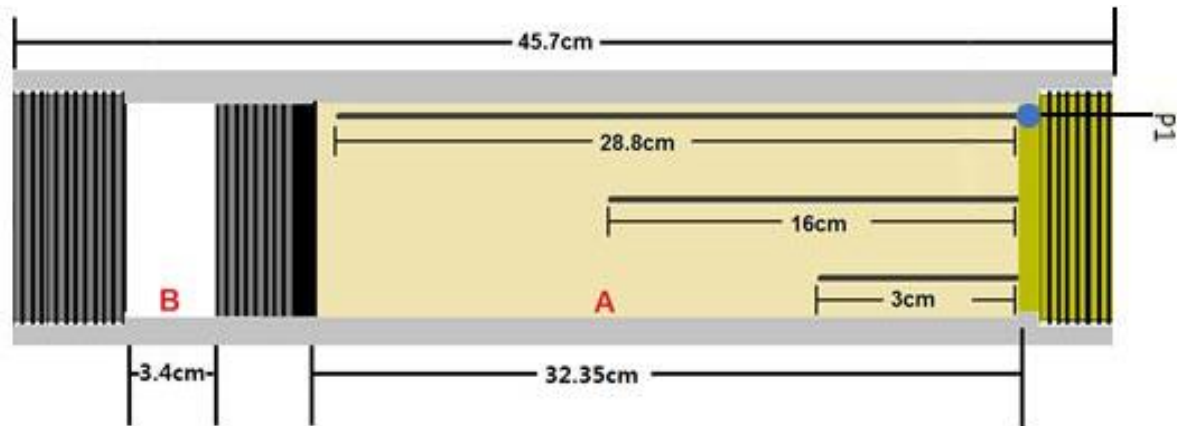
Figure II.1 The diagram of the cell used in the study of methane hydrate formation. (A) Sand pack including a pressure transducer and three thermocouples: Short, Medium, and Long; (B) Hydraulic cylinder used for the compaction of the sand. Cell stands vertically in a thermally insulated refrigerator during the measurements such that the pressure transducer and the thermocouples are located at the top. Reprinted with permission from "Modeling of Hydrate Formation Hysteresis in Porous Media" by Authors' Jeremy Adams, I. Yucel Akkutlu, George Moridis, 2019. Society of Petroleum Engineers, Copyright [2019] by Society of Petroleum Engineers.

1 cm from the edge of the sand pack. The next thermocouple is in the center of the pack, 16 cm from the copper plug, nearly exactly halfway between the sand pack and the steel piston and is labeled the "medium" thermocouple. The last thermocouple is located 180 degrees opposite to the short thermocouple and is 1 cm from the wall and 28.8 cm from the copper top and is labeled as the "long" thermocouple. The final component before sealing the system is a tube that runs down the sand pack (1 cm from the edge of the sand pack) past the long thermocouple and is used to add the water to the system. With these in place, the copper top is screwed on, and the cell is set vertically in a specially designed and calibrated refrigerator. Next, all the supporting lines are hooked up, and the data acquisition is set up.

After all the connections are air-tight, the system is put under a vacuum for three hours; this ensures that there is only a trace amount of nitrogen in the system and that, if there is any water (moist) in the rest of the system, it is removed. Putting a vacuum on the whole system is important due to the hydraulic portion of the cylinder (Figure II.1, Volume B), which requires no

compressibility in the chamber in order to be able to reach a high pressure. Once the vacuum is established, the hydraulic cylinder is pressurized, and the sand is compacted. 4,500 psi pressure is applied so that there is no movement of the sand grains during the hydrate formation, and a consistent porosity is maintained throughout the sand pack. Once the pressure has leveled off, 100 ml water is added to the system through the tube. The advantage of introducing water with the tube is that it brings the water up evenly from the bottom of Volume A and helps us maintain a uniform water saturation in the water-filled portion of the sand pack.

Next, the methane is added to the sand pack slowly so that there is minimal disturbance of the water. Following, the sand pack is sealed off, and the pressure and temperature are allowed to equalize for one day at a temperature of 25 degrees Celsius (C) before any cooling is applied. Once a day has elapsed, the system is cooled to 1 C and held there for at least one day. The cooling period ends when the pressure stops decreasing (there may be a very small drop, 1 or 2 psi after 2 hours, but it will be considered leveled off at this point), which indicates at this time that there is minimal hydrate formation. The system is then heated to 17 C, and this is the end of Cycle 1. For Cycle 2, the system is kept at 17 C for another day, and the temperature is again brought down to 1 C and kept there for a day; it is then heated to 25 C, at which it sits for one day. The rest of the thermal cycles are given in Figure II.2, and they follow the same logic as Cycles 1 and 2. For each cycle, the temperature for the short, medium, and long thermocouples, along with the pressure for the transducer is recorded at one-second intervals. After the five cycles are complete, the system is taken apart, the sand is dried, and the experiment is repeated
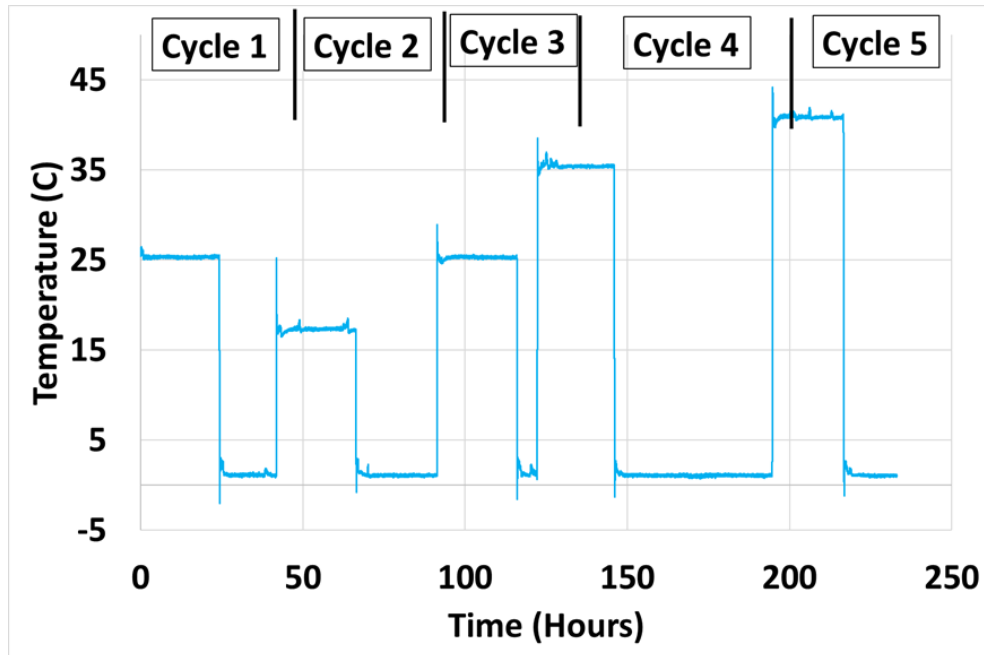
Figure II.2 Recorded refrigerator temperature history showing the thermal cycles the sand pack is exposed. Cycle 1 starts when the sand pack under thermal equilibrium initially at 25 C is cooled down to 1 C, followed by heating up to 17 C; Cycle 2 starts when the sand pack under thermal equilibrium at 17 C is cooled down to 1 C, etc. Reprinted with permission from "Modeling of Hydrate Formation Hysteresis in Porous Media" by Authors' Jeremy Adams, I. Yucel Akkutlu, George Moridis, 2019. Society of Petroleum Engineers, Copyright [2019] by Society of Petroleum Engineers.

from the beginning. The experiment is repeated twice more for three experiments. Although it was time-consuming, the repetition was necessary to reproduce the results and quantify the error in the pressure and temperature measurements.

<div align="center">

2.2 Relative Permeability

</div>

Previous studies have shown that injection of the inert gases causes dissociation of the hydrate during the flow measurements and influences the average saturations at which the relative permeability is measured. To predict the relative permeability in the presence of hydrate, the hydrate saturation must stay the same for all the ratios of the volumes of the flowing phases. Therefore, one important consideration for the measurements is the requirement to have stable hydrate saturation during the flow measurement stage. To accomplish this, the pressure of the

18

system needs to be just below the dissociation pressure, or right at it, thus preventing the formation of new hydrate.

The excess gas method (more gas stoichiometrically than water) is used in the sand pack so that all water is converted to hydrate. The pore volume is estimated from a spread sheet using the grain size distribution. The grain size distribution of the sand used is as follows: 49.4% 60 mesh, 43.2% 70 mesh, 4.1% 80 mesh, 3.1% 50 mesh, 0.1% 80. The sand is weighed, and water is added to the desired level using an accurate scale. The sand and water are mixed thoroughly and left to sit overnight in a plastic bag. Next, a sleeve 2 inches diameter by 8 inches in length is chosen. The end caps for the sleeve are chosen, and the inlet side is coated with silicon high vacuum grease to prevent the leaks. A stainless wire is then wrapped around the sleeve at the end cap. The inlet and outlet of the end caps are filled with steel wool to act as a filter and not let the sand into the auxiliary lines and pumps. Then the sleeve is filled with the sand; this is done by taking a spoonful of sand and tamping it down. There are 60 tamps per spoonful. This is repeated until the sleeve is filled with six inches of sand. Next, the outlet end cap is installed in the same manner as the inlet end cap. The filled sleeve is attached to the head of the pressure vessel, and a high-pressure plastic tube is routed from the outlet to the head. Next, the inside of the pressure vessel is coated with the same high vacuum silicone grease to prevent corrosion. Once completed, the vessel head is installed with the sleeve attached.

There are four different main lines that are installed to the vessel head, the gas inlet, the gas outlet, the water inlet, and the confining pressure, see Figure II.3. Transducers and valves are placed on each line, and a manifold between the gas inlet and the gas outlet is joined by a differential Azbil pressure transmitter. The water injection is placed after the differential pressure transmitter measurement point. On the outlet side, a volume 3/8-inch T fitting (the splitter, which

is oriented vertically) is used to prevent two-phase flow effects from affecting the differential pressure transmitter. The inlet gas and the inlet water lines are routed through a heat exchanger to chill the injected fluids, so that hydrate dissociation does not occur.

The vessel has a sleeve filled with a ratio of 1:1 propylene glycol water mixture to flow through so that the temperature of the sand pack can be controlled.

Figure II.3 shows the layout of the experimental apparatus used for the study. All the connecting lines are 1/8-inch stainless steel Swagelok 5,000-psi-rated lines. The setup is built on a general electric medical CT scanner, and the sample is scanned initially and scanned each time a change in the saturations is expected to take place due to flow or hydrate formation.

In Figure II.3, the separator used is a T fitting between the differential pressure transmitter and the outlet. The gas-phase rises to the top, and the water is separated downwards toward the volume of the outlet pump. While the separator works reasonably well, it can cause pressure build-up in the gas phase during the flow measurements. This can cause complications in pressure response. This type of setup, when the T separator is vertical, can create a Trompe (a type of air compressor without any moving parts). This contributes to the pressure oscillations that are seen in Figure II.4 (Azzi et. al., 2010). While this buildup will affect the system, due to
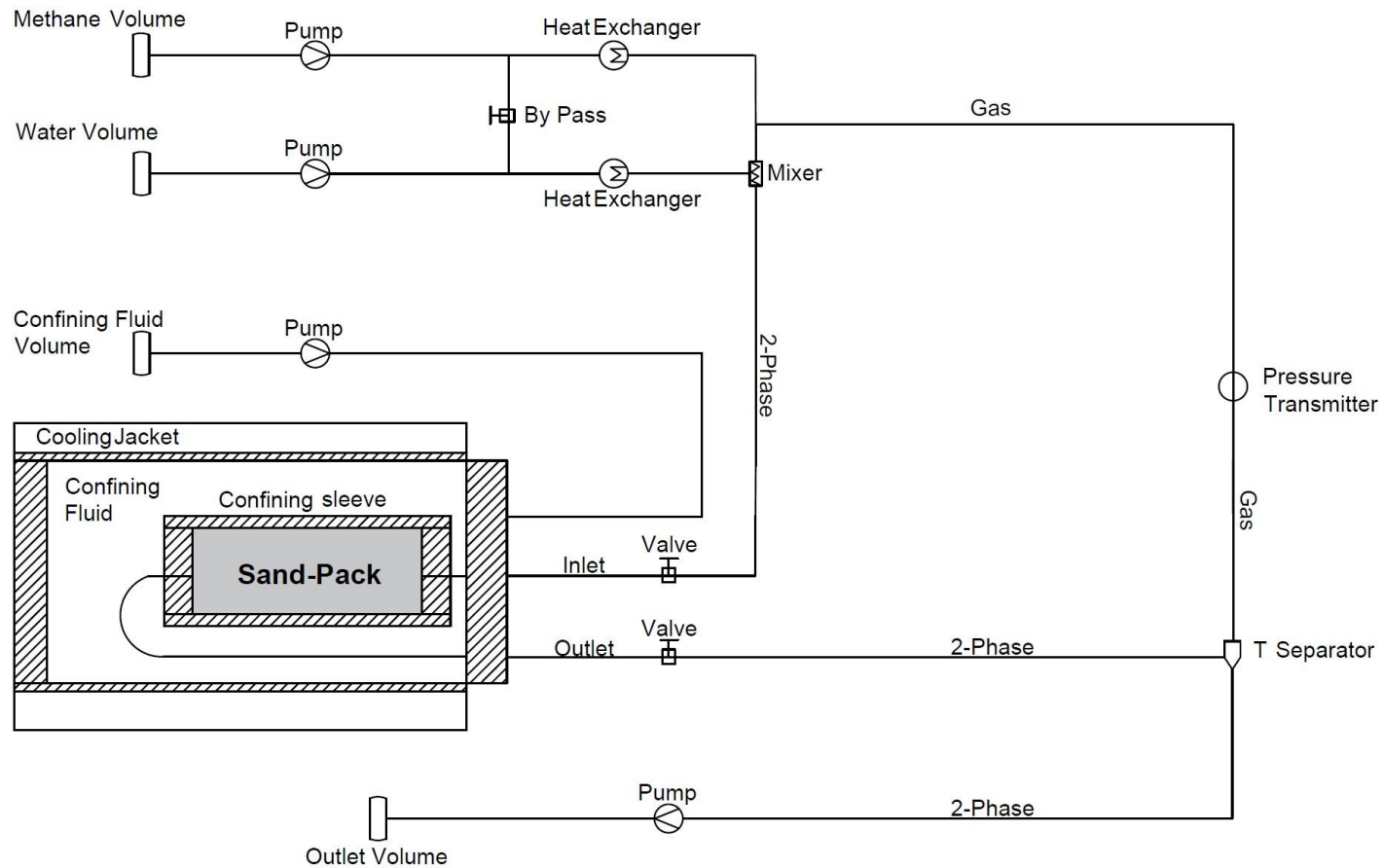
Figure II.3 Diagram showing the laboratory setup of the sand pack for flow experiments and the auxiliary units, including the syringe pumps, differential pressure transmitter, gas-water mixer, and the splitter. Reprinted with permission from "Modeling of Hydrate Formation Hysteresis in Porous Media" by Authors' Jeremy Adams, I. Yucel Akkutlu, George Moridis, 2019. Society of Petroleum Engineers, Copyright [2019] by Society of Petroleum Engineers.
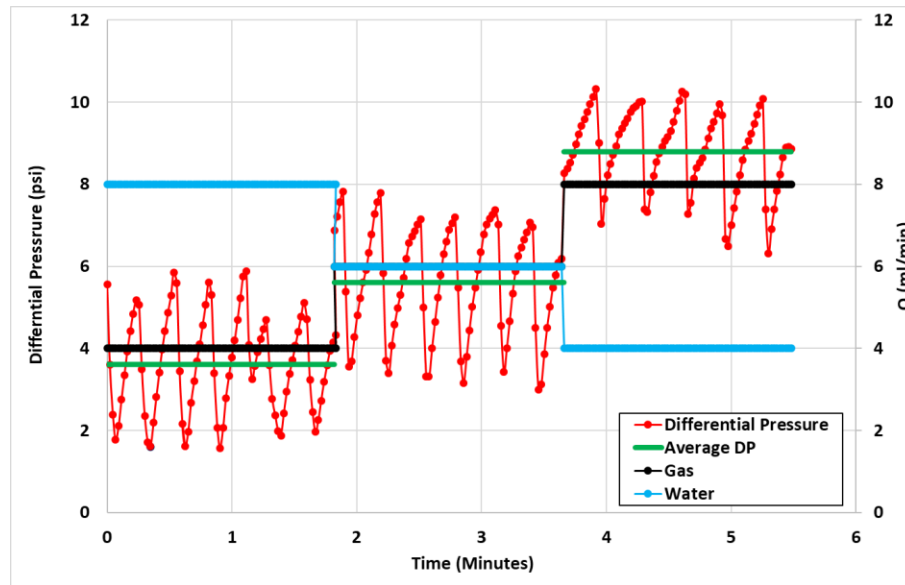
Figure II.4 Differential pressure versus time when the steady-state flow is reached. The secondary y-axis showing the flow rates of the gas and water is on the right. The green line represents the data used for the gas relative permeability estimation using Darcy's law.

the low volumes and low head pressure on the sand pack, its magnitude is expected to be

low relative to the pressure values measured during the experiment.

2.2.1 Experimental Procedure

The experimental procedure involves steady-state flow measurements and has three

main parts: (i) single-phase (gas) flow measurements at room temperature in the

absence of hydrates, (ii) gas flow measurements at low temperatures with hydrates, and

(iii) multi-phase *

flow measurements where a fixed ratio of gas and water flow rates is injected. Each part

includes the measurement of effective gas permeability, followed by the relative gas

permeability.

For all the flow experiments, the initial steps are as follows:

1. The first step is to check the assembly for leaks by pressurizing the lines to 100 psi initially. To test the lines at higher pressure, the sand pack is isolated from the other lines at the inlet and outlets of the vessel. Then, each line and fitting are checked with soapy water at the operating pressure of 500psi, where a leaky component produces bubbles. If leaks are found, they are dealt with by tightening the fittings. Then the system is returned to atmospheric pressure, and a vacuum is placed on the system. Next, the system is pressurized with low-pressure carbon dioxide to flush the nitrogen out of the system, and any nitrogen out of solution, since CO_2 is preferentially dissolved and displaces nitrogen molecules in water. Next, another vacuum is placed on the system, and the system is flushed with methane gas. The vacuum and methane injection thus remove the CO_2 gas and provide an environment for pure methane hydrate formation to occur.

2. The sand pack is next needed to be pressurized to operating conditions at 500 psi pore pressure and 600 psi confining pressure. A pressure difference of 100 psi is kept for the sand pack. The pore pressure and confining pressure are increased by 50 psi increments. The confining pressure is controlled manually so that the fluctuations are kept in the 25-45 psi range during pressurization.

3. Once the sample is pressurized, the system is left to equilibrate for a few hours; this allows the stress field in the sand pack to stabilize. Once the setup is ready, the initial CT scan is performed, and the corresponding images are saved.

Now, we perform the first part of the flow experiments, i.e., the steady-state single-phase (gas) flow experiment. This test is performed at room temperature.

4. Before beginning the gas flow, the zero differential pressure point needs to be established, so the differential pressure transmitter is closed in at the manifold and the data recorded for a few minutes, this is to provide a zero of the system. Then, the transmitter is opened to the system, and the upstream and downstream bypass valve is closed. The inlet and outlet pumps are set to constant flow, inlet injecting at a constant rate, and outlet drawing at a constant rate.

5. Steady-state flow measurements are performed. The applied gas flow rates in ml/min are as follows: 20, 25, 40, 45, all the while, the pressure difference, delta P, is measured. After the gas flow is completed at these rates, the sand pack is scanned, and the images saved.

6. Once the pressure and flow rate data are collected, the permeability of the sand pack is estimated using Darcy's equation of flow for ideal gases:

$$\frac{Q}{A} = \frac{k}{\mu}\left(\frac{p_1^2 - p_2^2}{2*L*p_2}\right) \qquad \text{Eq. II-1}$$

Eq. II-2 is used in graphical format as a straight line. When q/A versus $(p_1^2 - p_2^2)/(2p_2L)$ is plotted, the slope is equal to k/μ, and it can be used to solve for the permeability if the methane viscosity at the room temperature is known.

7. The next step is to repeat the flow measurements at different rates when the sand pack is cooled so that the methane hydrate crystals form in the sand pack. To form

24

hydrate, we perform the following steps: at the operating pressure of 500 psi, the system is cooled down to 2 degrees Celsius to initiate the hydrate crystallization. The cooling process is observed by keeping track of the temperature change in the system. When the cooling is complete, to determine if the hydrate is finished forming, the gas volume is recorded. If there is no change in the inlet volume of the pump, then hydrate formation is considered complete, or at the least, the crystallization is occurring at a very low rate. Following the hydrate formation, the flow is considered at a fixed rate, as we did in Step 5 in the absence of hydrate. Finally, the sand pack is scanned again.

8. Steps 5-6 are repeated with the sand pack in the presence of hydrates.

The above section outlines the steps for single-phase (gas) flow at a fixed saturation of water and methane hydrate. In order to see the impact of hydrates on the flow, the hydrate saturation needs to be increased, but this must be done in the sand pack in a uniform fashion. We ensure this with the following steps:

9. Water and gas were simultaneously injected at an equal and constant rate of 6 ml/minute. Co-injection continued until three pore volumes of water were filtrated through the sand pack. At the end of co-injection, the data is collected for the effective gas permeability. Step 9 was repeated twice, and these two steps produced intermediate hydrate saturation. When there is hydrate present in the sand pack, the rates measured ranged in between 0.25 ml/min to 6 ml/min. The procedure continues

until the water injection, and hydrate formation resulted in no flow. This final stage will be the case when hydrate saturation reached no-flow conditions; thus, the measurements were stopped for the single-phase (gas) flow.

10. Finally, the steady-state multiphase flow experiments were conducted at 20 degrees Celsius when a total (water + gas) flow rate of 12 ml/min was flowed through the sand pack. The gas/water flow rate ratios applied during the experiments were 8/4, 6/6, and 4/8 ml/min. Three pore volumes of water were injected to ensure that steady-state was reached. Figure II.4 shows the flow rates applied and the differential pressure values measured in time during the steady-state multiphase flow experiments.

There are oscillations in pressure that are quite large; this is due to two phenomena. Firstly, the tubes that injected the fluids are 1.45 mm in diameter, and for the two-phase flow, this results in capillary tube effects, thus causing fluctuation. Secondly, the outlet has the two phases flow out into a T-junction, which was shown as the fluid separator in FigureII.2. A T-type separator can act as trompe. A trompe is a device that separates gas and water due to buoyancy, causing the gas to build pressure in the gas-only region if there is no outlet, where the gas pressure limit is the pressure head of the water. Historically this device was used as a water compressor in mines and thus was useful, but here it produces oscillations in the pressure transducer response.

The selected data points in Figure II.4 shows the smooth data (shown in green) near the middle to the end of each flow rate; this allows for equilibration of the saturations; thus, the pressure drop. Taking this data, the relative permeability can be calculated using Darcy's law. Next, we measure the effective gas permeability in the presence of hydrate and compared to the effective permeability with no hydrate, as discussed earlier in Figure II.3 and Figure II.4.

At the end of the injection period for each ratio, the sand pack was scanned, and the images saved. The resulting data is then used to calculate the effective gas permeability at different saturations.

11. Next, the relative gas permeability is calculated from the effective gas permeability data. The gas relative permeability at saturation S_w is defined in our study as the effective permeability k_g at that saturation divided by the permeability at the irreducible water saturation $k_{g\,@S_{w,irr}}$:

$$\boldsymbol{k_{rg}} = \frac{\boldsymbol{k_g}}{\boldsymbol{k_{g\,@S_{w,irr}}}} \qquad\qquad \textbf{Eq. II-2}$$

2.2.2 Theoretical Basis for the Experiment*

The reason for this approach with multiple cycles of heating and cooling is to determine the effect known as hysteresis. Hysteresis describes a path-dependent phenomenon in the form of a time series. This effect is seen during methane hydrate formation as differences in the initial formation times, and at different locations on the pressure-

temperature phase diagram, i.e., the difference in sub-cooling, and the difference in equilibrium pressure and current pressure. The cycles connect the physical phenomena by creating a continuous data set in which the mass and volume of the system stay constant. This provides an environment where the only independent variable is the temperature, and any observed differences in hydrate formation behavior are either due to a change in cooling rate or due to hysteresis.

The objective is to find hysteresis in a porous medium, and thus the discovery of dependence on thermal rate was secondary to this objective. The determining factor of hysteresis is when hydrate starts to form, and especially when significant formation occurs. In bulk hydrate formation, the only importance is the initial formation time, due to the nucleation event being singular. But in a porous medium, the nucleation process is spatially distributed and can be countless. Thus, the need appears for including the location at which significant formation is observed. In the case of initial formation, the formation data is based on the phase diagram, and equilibrium conditions are assumed because no simulation work is used to calculate a deviation from the equilibrium. The point of significant hydrate formation is determined by the recorded temperature data. Hydrate has a heat of enthalpy of 438 J/g. The cooling of a system produces a monotonously decreasing temperature profile unless there is internal heating in the system, in which there can be an increase in the local temperature of the system. A temperature increase in the time series indicates rapid hydrate formation, and the

inflection point is the point when the hydrate heat generation rate is equal to the cooling rate of the system. The determination of significant hydrate formation is then the time that the heat generated is equal to the heat loss of the system. This point can be observed easily on the recorded temperature time series, and the recorded pressure versus temperature plots as an inverse of the slope. All these features will be shown in the following sections, accompanied by a detailed explanation of each cycle. Further, a quantitative approach will be introduced to consistently determine the initial hydrate formation time.

CHAPTER III *

DISCUSSION AND RESULTS*

3.1 Analysis of Experimental Results in Phase Equilibria

3.1.1 Time Series of Temperature

In the corresponding analysis, the time series for the short and medium thermocouples are shown; there is a long thermocouple, which will be briefly described--but since no significant amount of hydrate can form in its surrounding, it is not mentioned hereafter.

Figure III.1 shows the measured temperature history of the short and medium thermocouples during each cycle. For the first 24 hours, the system is in thermal equilibrium, and the temperature at the very beginning is higher than the room temperature because the sand had not been out of the oven for very long. After a day, the temperature readings settled within a degree and a half of each other. During the cooling phase, starting around the 24th hour, the temperature profiles for each thermocouple are given. Clearly, there is a distinct behavior that is observed at hour 18.3, when the temperature increases, rather than decrease, during the cooling. This is due to hydrate
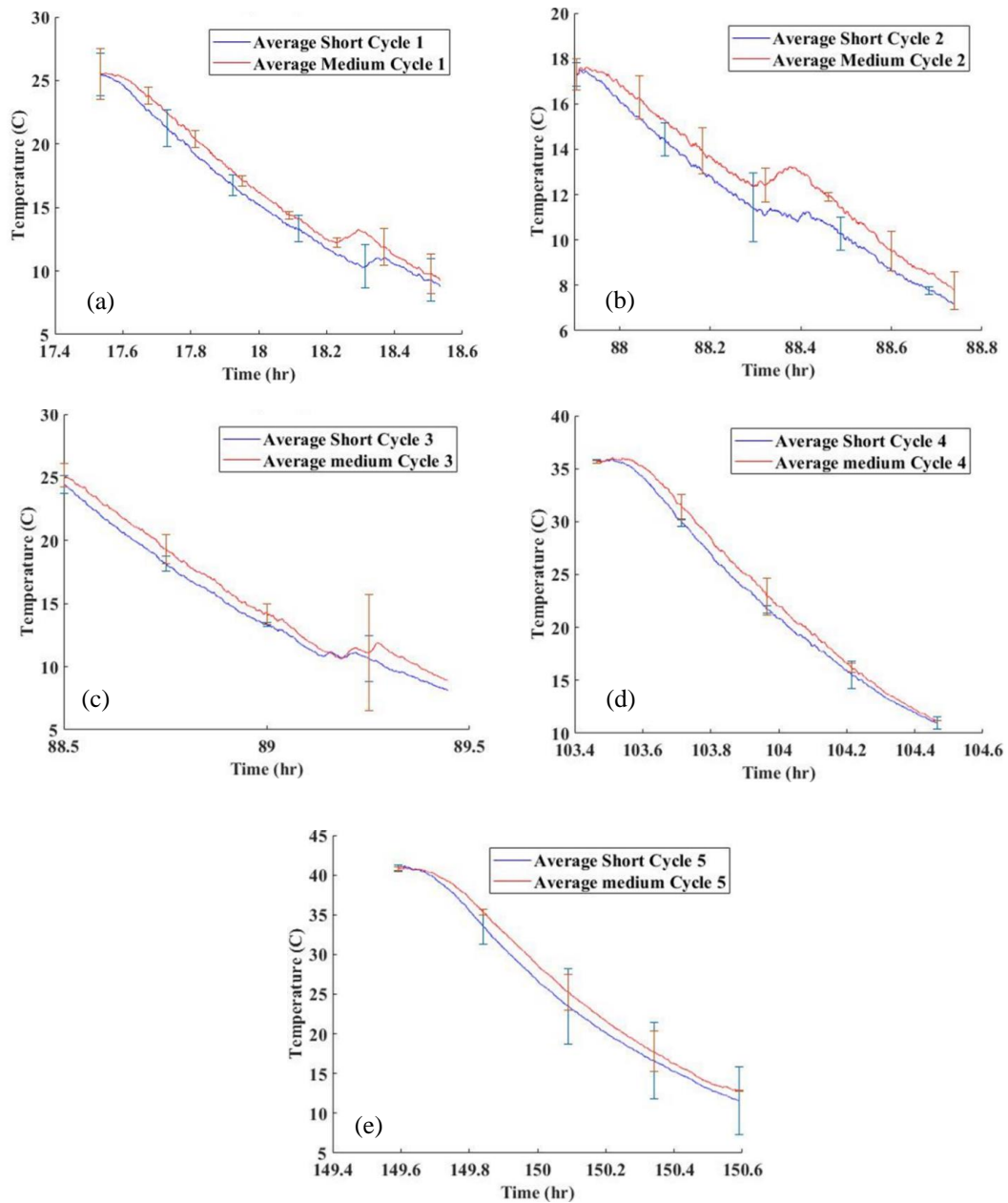
Figure III.1 The recorded temperature history of the short (blue) and medium (red) thermocouples during cycles. bars are 90% confidence bounds. Reprinted with permission from "Modeling of Hydrate Formation Hysteresis in Porous Media" by Authors' Jeremy Adams, I. Yucel Akkutlu, George Moridis, 2019. Society of Petroleum Engineers, Copyright [2019] by Society of Petroleum Engineers.

formation. At this time, the refrigerator temperature is roughly 1.5 C, and the only heat source is the crystallization. Given that the heat generation for hydrate is 438 J/g, and the average specific heat capacity of the surroundings is around 2,000 J/kg-C, the amount of hydrate formed is significant. (Gupta, Lachance, Sloan, & Koh, 2008). There is at least a 1 C increase for the middle thermocouple and a half degree increase for the short thermocouple. Based on this information only, one can estimate what the water saturation distribution in the sand pack looks like. Since the water was added from the bottom of the sand using the tube, and the sand being unconsolidated, the saturation transition zone in between the water and gas phases is short. Hence, the water should be mostly localized to the long thermocouple and the medium thermocouple. This means that the short thermocouple at the upper portion of the sand receives much less water, the medium has more. Focusing on the medium thermocouple, now there are obvious thermal effects in Figure III.1 are due to the hydrate formation. There are responses in the temperature that both fluctuate and linger longer than that of the short or long thermocouples. This is important later, when determining the initial hydrate formation times.

Continuing to Cycle 2, Figure III.1 shows the same type of graph, and sheds light on what happens when the hydrate formed is only melted to 17 C. A note here is that the thermal gradient Cycle 2 experiences is uniquely different than the other cycles, which can be seen clearly in the analysis section of the pressure versus temperature profiles. It is stated here since the medium thermocouple is also unique with four major temperature

peaks--one being earlier than the short thermocouple, and another three peaks in rapid succession. These peaks, rather spikes, make the analysis of this cycle more complicated, and it is most likely a feedback response to the generated heat. The hydrate cell is in a thermally insulated system, where the hydrate-generated heat can increase the overall temperature of the system. This has previously been reported in other publications as well, and in one particular work (Linga, et al., 2009), it was shown that the magnitude of the temperature spike is proportional to how thermally-insulated the system was. This makes for an interesting experiment, since most natural hydrates are not in a thermally conductive system, while many laboratory setups are. The referenced experiment also demonstrated that there could be a feedback loop in the system. While, in this case, the amount of hydrate in the sand is not enough to melt the hydrate, in a natural system, it is foreseeable that this type of situation can occur. Having enough to melt the hydrate in a natural system, it is foreseeable that this type of situation can occur. Having completed the discussion of cooling, looking at the heating side for Cycles 1 and 2 in Figure III.1, there is a significant temperature drop near the hydrate melting temperature of 15 C, (roughly the melting temperature for the pressure in this particular system) which has the effect of re-forming hydrate, even ice, if enough hydrate is melted. This is due to the system being thermally confined.

One of the major reasons that this experiment was designed, to begin with, is to be able to determine if hydrates became easier to form when repeated cycles of melting and forming are conducted. Based on the experimental data, it certainly seems that this is

true. The temperature spikes in Cycles 2 and 3 show that they are more aggressive than in the first cycle. These aggressive temperature spikes are indicative of earlier hydrate formation, i.e., a faster hydrate formation rate. Cycle 3 temperature behavior includes the same trend during cooling. Furthermore, as the cycles continue, the short thermocouple has only one peak and is similar in size to the other peak for the small thermocouple. The long thermocouple shows a reduced trend, and only a small increase in temperature at the same time as the large second peak of the medium thermocouple--indicating that it is the heat transfer, not hydrate formation.

The reduced magnitude of the medium thermocouple temperature spikes is shown for Cycle 4 and is prolonged over an hour, rather than being sharp as in Cycles 2 and 3. This indicates that there was a reduction in the hydrate formation rate. One of the ideas in hysteresis is that there are partially melted clusters of clathrates that form nucleation sites for the subsequent cycle to form hydrate easier, but these nucleation sites can be destroyed when the temperature in the sand rises above a certain point. In this case, the temperature for the start of the relaxing effect was 35 C.
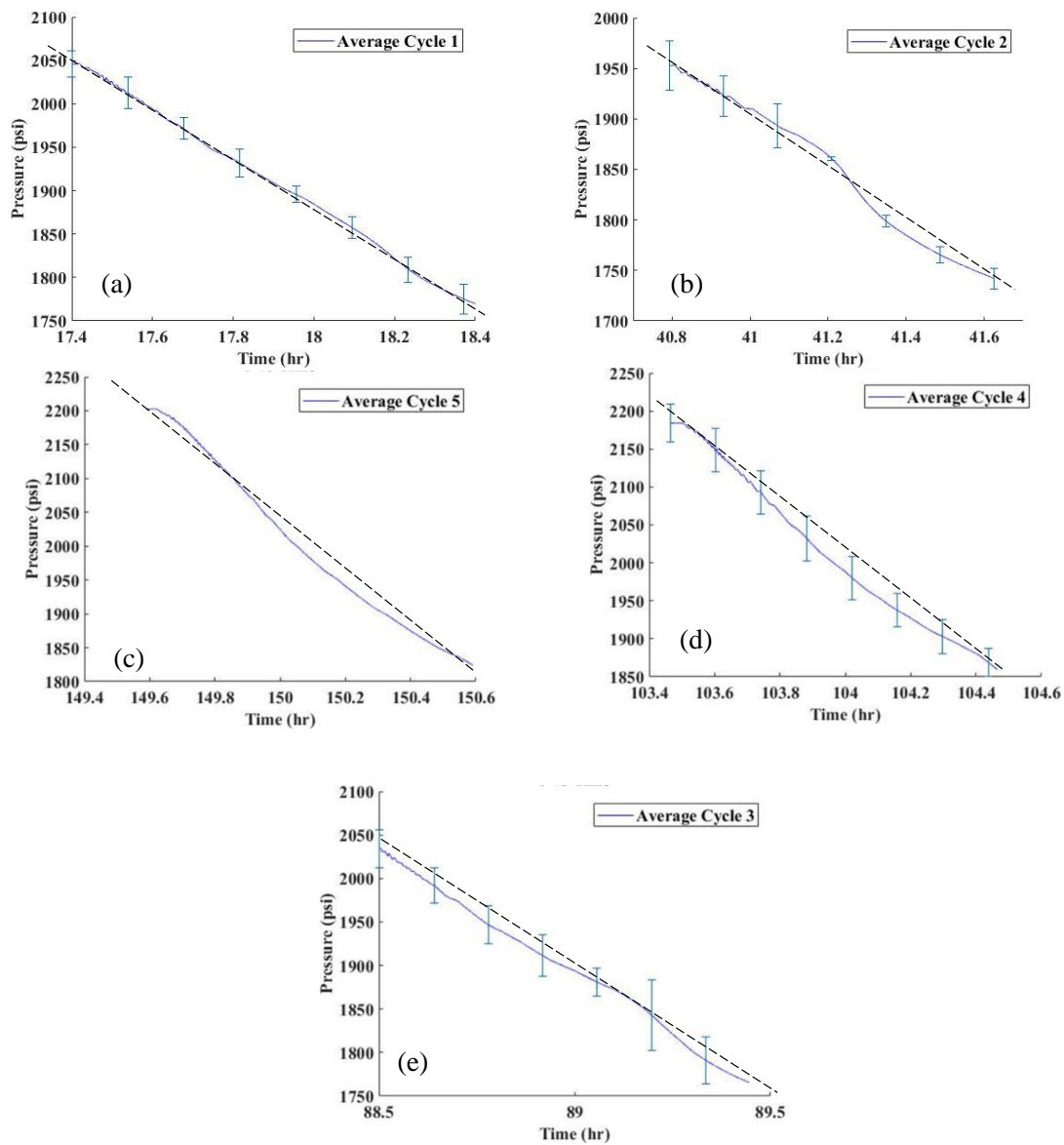
Figure III.2 The recorded pressure history during the cycles of cooling and heating. Reprinted with permission from "Modeling of Hydrate Formation Hysteresis in Porous Media" by Authors' Jeremy Adams, I. Yucel Akkutlu, George Moridis, 2019. Society of Petroleum Engineers, Copyright [2019] by Society of Petroleum Engineers.

This effect associated with the removal of the nucleation sites is seen even more clearly as the magnitude, and the general shape of the medium thermocouple reading resembles the first cycle. From a temperature point of view, the analysis should be focused on the short thermocouple. Based on the analysis, we conclude that during any calculations and predictions, the limited hydrate formation in the short thermocouple will provide a smoother and more predictable response. A side note on bulk hydrate formation is that it is highly random, [this has previously shown by Bagherzadeh et al., where the rates were measured using a magnetic resonance imaging method (Bagherzadeh et al., 2011)]. Randomness means that even when all conditions are kept the same, the hydrate formation rates are not constant. In the sand pack, which includes added complexities, the hydrate formation could experience larger variance in the formation rates. Due to this issue and the fact that hydrate produces heat when generated, the short thermocouple is the focus of the analysis. This is for two reasons, as just stated--the hydrate formation rate has a random aspect, but also the heat transfer is radial in this section due to it being near the edge of the sand pack. The long thermocouple is in a mostly water environment; thus, hydrate formation is minimal. The medium thermocouple is in the center of the sand pack; thus, it is affected by heat

transfer from all directions and is more insulated to the surroundings. Therefore, hydrate formation will produce complicated thermal profiles, such that under the analysis of experimental data only, it will be unclear as to which the major contributors are.

36

Therefore, the short thermocouple is used to analyze the system further and define hysteresis.

3.1.2 Time Series of Pressure

Figure III.2 shows the pressure response related to hydrate formation during the cycles. The black dashed line is a reference to a linear line to help us visually identify the severity of the deviations in the pressure profile*. While it looks minor, any observed deviation from linearity due to temperature drop indicates the hydrate formation. Remember, the hydrate formation started at the 18th hour, and there is a change in slope here confirming the hydrate formation.

Figure III.2 clearly shows an inflection point in all of parts a-f. The pattern (looking from left to right) for cycle 2 was as follows: the pressure drop was concave to just before 41 hours, convex for a short amount of time, concave for a good period and then back to convex, where it turns to a linear function to the end of the cycle. The hydrate formation rate increases when the slope steepens then slows down when the pressure levels off. The change in slope continues to vary, and thus the hydrate formation rate varies. Cycle 3 has almost the identical thermal gradient as that of the first cycle, but it has a drastically different pressure profile. There exist four inflection points on the pressure profile, and these points line up with the temperature spikes. The pattern for Cycle 3 increases in frequency and has a combination of linear parts and highly nonlinear parts as well. This is due to hydrate formation during Cycle 3. Pressure response to a temperature change is rapid and linear.

Cycle 4 is the cycle where we expect that the response should have reverted back to the original shape, and indeed it does so for the most part; the complexity of the previous cycle has been all but eliminated, with only slight oscillations, and one bump. This indicates a direct link between the temperature spikes and the pressure nonlinearities.

Cycle 5 shows a similar response with a pressure profile very similar to Cycle 4. The repeated melting and cooling can affect the saturations of the water and gas in the system and thus change the initial conditions; thus, the difference between Cycle 1 and Cycle 5 can be explained. In conclusion, the relaxation of the memory effect has occurred, and that there are small differences in saturation that prevent the exact return to the initial conditions.

3.1.3 Pressure versus Temperature Data and the Phase Diagram

To make a fair comparison of different thermal cycles, a clear basis for comparison is needed. There are a few obvious choices: pressure versus time, temperature versus time, or a set time from the initial cooling. These choices, however, do not represent a clear measure, which ensures that all the cycles are compared equally. What is needed in the investigation is a reference, and one that considers both the temperature and pressure so that there can be a standard measure. This reference is the equilibrium phase line in the pressure versus temperature plot. All cycles will be compared to starting from a certain distance from the line, using the pressure difference.

In Figure III.3, a location shown as blue circles represents an experimental value for pressure and temperature in time. The difference in pressure from the experimental and the equilibrium line could be either positive, which means that the system can form hydrates or negative, meaning that under equilibrium conditions, there is no hydrate formation. Eq. III-1 is the phase equilibrium curve shown in Figure III.3. The data for the curve is obtained from the Tough+Hydrate simulation software.

$$P_{eq} = a_1 T^5 + a_2 T^4 + a_3 T^3 + a_4 T^2 + a_5 T + a_6; \qquad \text{Eq. III-1}$$

The coefficients a_1-a_6 are given in Table III-1.

Knowing these coefficients, Eq. III-2 can be used to predict the pressure difference or the delta-pressure:

$$\Delta p = P - P_{eq}; \qquad \text{Eq. III-2}$$
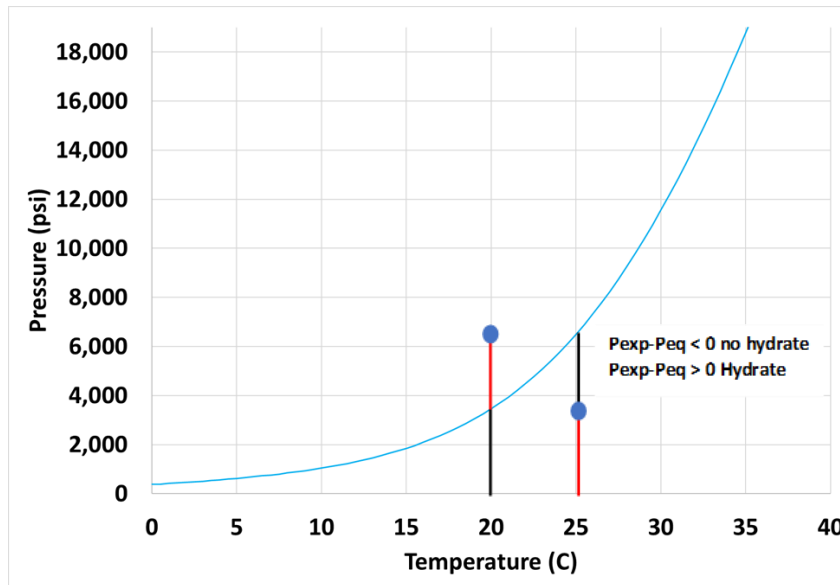
Figure III.3 Pressure-temperature phase diagram for methane hydrate showing delta-pressure and delta-temperature. Reprinted with permission from "Modeling of Hydrate Formation Hysteresis in Porous Media" by Authors' Jeremy Adams, I. Yucel Akkutlu, George Moridis, 2019. Society of Petroleum Engineers, Copyright [2019] by Society of Petroleum Engineers.

The recorded temperature and pressure values of the experiment used to calculate the delta-pressure values behave, as they should: they yield negative delta-pressure when they are below the equilibrium line, and positive when they are above the line. This is done for each cycle. The smallest common starting value observed is used for the reference point of all cycles. In this case, it is Cycle 2, which has the lowest starting temperature of 17 C, and thus the smallest delta- pressure at the start of any cycle. The value is -572 psi. The next step was to find this value (or as close as possible) in all the other cycles and to zero out the time when all cycles are equal to this value. This means that all the cycles start the same delta-pressure away from the equilibrium line, thus

Table III-1 The coefficients and their values used in Eq. III-1.

Coefficient	Value
a_1	-0.00056
a_2	0.05147
a_3	-1.025
a_4	11.93
a_5	2.282
a_6	406.6

considering both temperature and pressure. One other factor in ensuring that all cycles can be equally compared is to look at the driving force during the hydrate formation, which was the temperature difference between the thermocouple and the outside refrigerator.

To fairly compare each cycle, this temperature difference needs to be very close for the different cycles; if they were not close, that cycle should be set aside in the discussion of hysteresis. As we show in Figure III.4, there exists a large difference in delta-temperature between Cycle 2 and the other cycles; this is due to how close the starting temperature was to the hydrate formation line. There was not enough time for refrigerator temperature to equalize and produce a consistent result, so Cycle 2 will not

41
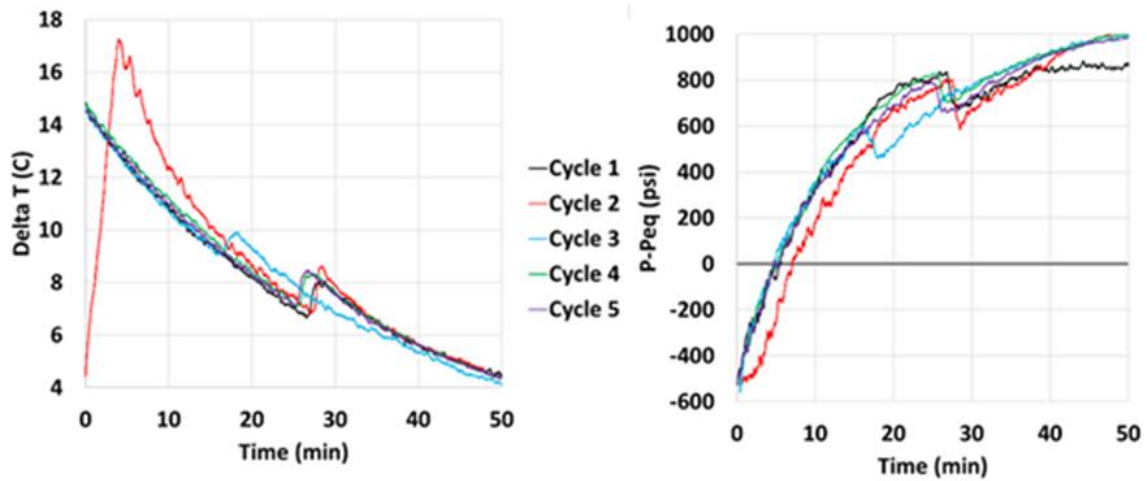
Figure III.4 Delta-temperature and delta-pressure time-series of the cycles. Reprinted with permission from "Modeling of Hydrate Formation Hysteresis in Porous Media" by Authors' Jeremy Adams, I. Yucel Akkutlu, George Moridis, 2019. Society of Petroleum Engineers, Copyright [2019] by Society of Petroleum Engineers.

be considered in the analysis of the hysteresis.

Another feature of the delta-pressure is that it mirrors the temperature profile, so a peak such as the ones observed in the temperature profiles will produce a valley, and a valley in temperature will produce a peak in the delta-pressure plot. This is also important because the trends of formation and melting can be easily observed. To find hysteresis, the values near zero delta-pressure are important, because a value of zero will determine when hydrate start forming.

Figure III.5 shows the delta- temperature, which is on the left, and the delta-pressure on the right. Clearly, the thermal gradient shows some variance but is very close for cycles 1, 3, 4, and 5--but Cycle 2 is very different. Since the cooling is slower, the initial formation time will be different.
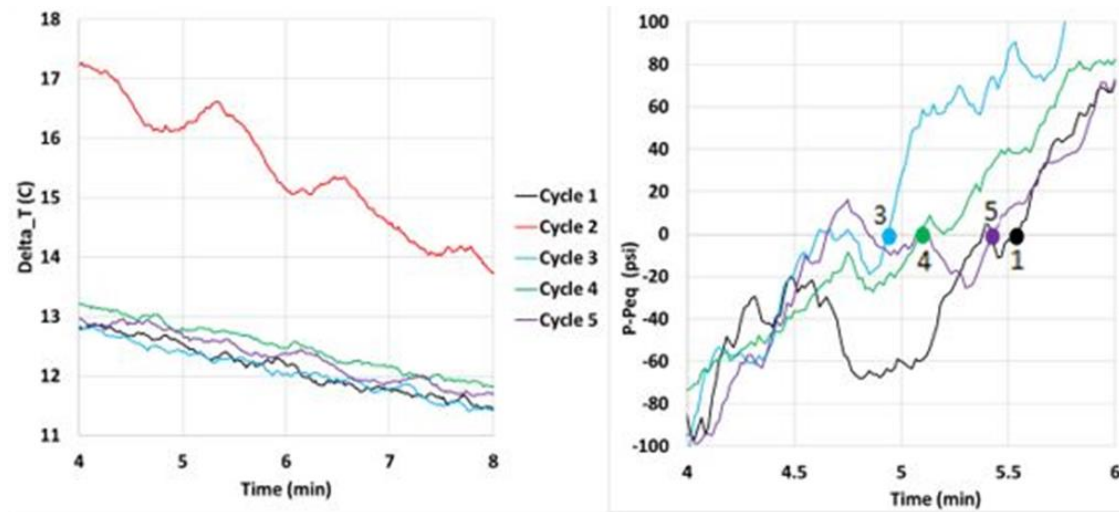
Figure III.5 Close-up view of the Delta-pressure near zero. Reprinted with permission from "Modeling of Hydrate Formation Hysteresis in Porous Media" by Authors' Jeremy Adams, I. Yucel Akkutlu, George Moridis, 2019. Society of Petroleum Engineers, Copyright [2019] by Society of Petroleum Engineers.

Thus, the analysis of cycles 1, 3, 4, and 5 can focus on hysteresis rather than thermal issues. The idea of hysteresis is that hydrate forms easier when there are repeated melting and cooling cycles. This is thought to be caused by a memory effect of the water so that the hydrate forms faster and easier the next time the temperature is near or at its freezing point. So logically, the hydrate should form easier as we proceed with the cycles. To test whether the melting temperature would influence the memory effect, the later cycles (Cycles 4 and 5) are designed so that the sand pack is heated to a much higher temperature than that of the first cycle.

The idea is that the higher melting temperature would erase the memory of water; hence the hydrate formation characteristics of the cycle should be similar to the first cycle.

Table III-2 Recorded maximum temperature and hydrate formation time for the cycles 1-5. Reprinted with permission from "Modeling of Hydrate Formation Hysteresis in Porous Media" by Authors' Jeremy Adams, I. Yucel Akkutlu, George Moridis, 2019. Society of Petroleum Engineers, Copyright [2019] by Society of Petroleum Engineers.

Cycle	1	3	4	5
Max. Temperature (C)	25	25	35	40
Formation Time (s)	332	296	305	325

With this understanding, now we visit Figure III.3 and observe that this pattern clearly exists on the right figure --Cycle 1 forms the slowest, then Cycle 5, then 4, then 3, with 3 being the fastest. Again, Cycle 2 should not be added to the discussion here due to its inconsistent thermal difference. As seen in Table III-2, a clear correlation exists between the maximum melting temperature of the cycle and the hydrate formation time. This is indicating that the hysteresis theory based on the memory effect of water is at work in our experiments.

The time difference between Cycles 1 and 3 is 30 seconds, which does not sound like much, but it is significant when one considers the small difference in thermal gradients in between the cycles. 10 percent difference in the gradients would only account for 15 seconds in the initial formation time. The experimentally observed differences are much larger than that.
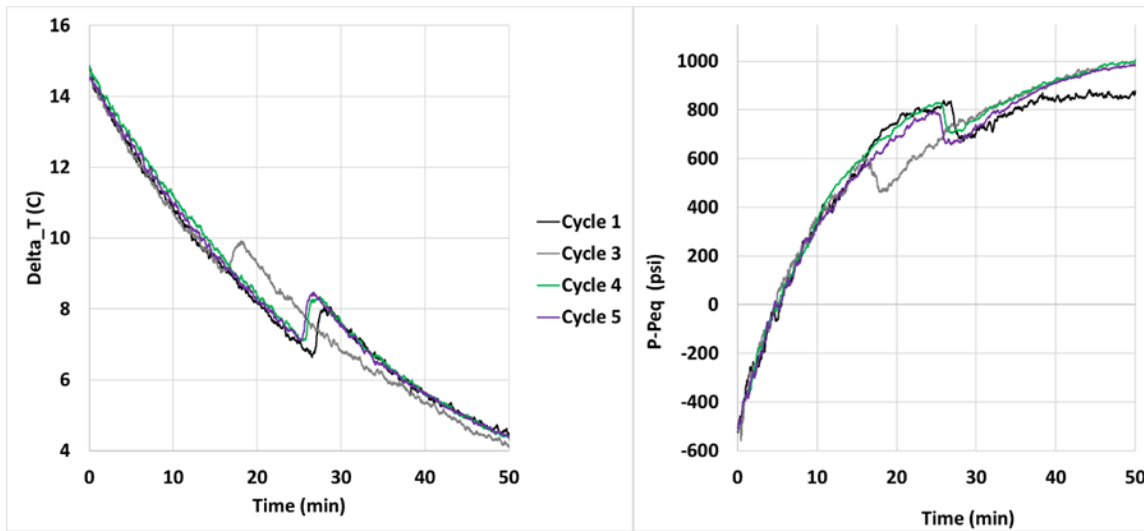
Figure III.6 Delta-pressure and delta-temperature history at large timescale. Reprinted with permission from "Modeling of Hydrate Formation Hysteresis in Porous Media" by Authors' Jeremy Adams, I. Yucel Akkutlu, George Moridis, 2019. Society of Petroleum Engineers, Copyright [2019] by Society of Petroleum Engineers.

Before continuing the discussion of the hysteresis, the thermal difference in Cycle 2 shows that the thermal distance to the outside temperature is important to the formation rate, the temperature, and pressure profiles. In Figure III.5, the temperature difference for Cycle 2 is 4 degrees larger than that of the other cycles; thus, the formation time is longer by 1 minute and a half. The percent difference in the thermal distance is -31 percent, and the difference in formation time for Cycle 2, when compared to cycle 1, is -27 percent; thus, there is nearly a one-to-one relation between the differences in thermal distance to the formation time. Accordingly, the difference between Cycle 1 and 3 temperature distances should produce a similar result in the formation times of Cycles 1 and 3. However, the formation time of the first cycle and the third cycle is larger than the

45

difference caused by the temperature difference. Thus, the hydrate hysteresis is clearly observed.

But this is only a small timeframe, so let's look at the larger picture and see what unfolds. In Figure III.6**,** large-scale differences in delta-pressure are shown as the time progresses. The valleys in the profiles are places where heating occurs due to hydrate formation. The heat causes the system to advance towards the hydrate equilibrium line-- the zero line. If the system is near the line, to begin with, it is foreseeable that heat generated by hydrate formation can cause the hydrate to melt. While not encountered in this work, it is an issue to be aware of. The locations of the valleys are indications of when significant hydrate is formed; heat generation is proportional to the amount of hydrate, and since there are valleys in the delta-pressure profile indicating a temperature spike in the time series, there has to be hydrate generated. Looking at the thermal difference can give more insight; the locations of the valleys in the delta-pressure and peaks in delta-temperature, show a change in the slope from cooling to heating-- meaning that there is more heat being generated than that taken away by cooling meaning that there is more heat being generated than that taken away by cooling. This is another indicator of hysteresis; not only does the initial formation time vary, and becomes easier for Cycle 3, it also forms hydrate faster than the other cycles by 10 minutes. This means that there is a significant difference in times and clearly shows the hysteresis. Further, the return to the first cycle indicates that there is a loss of the
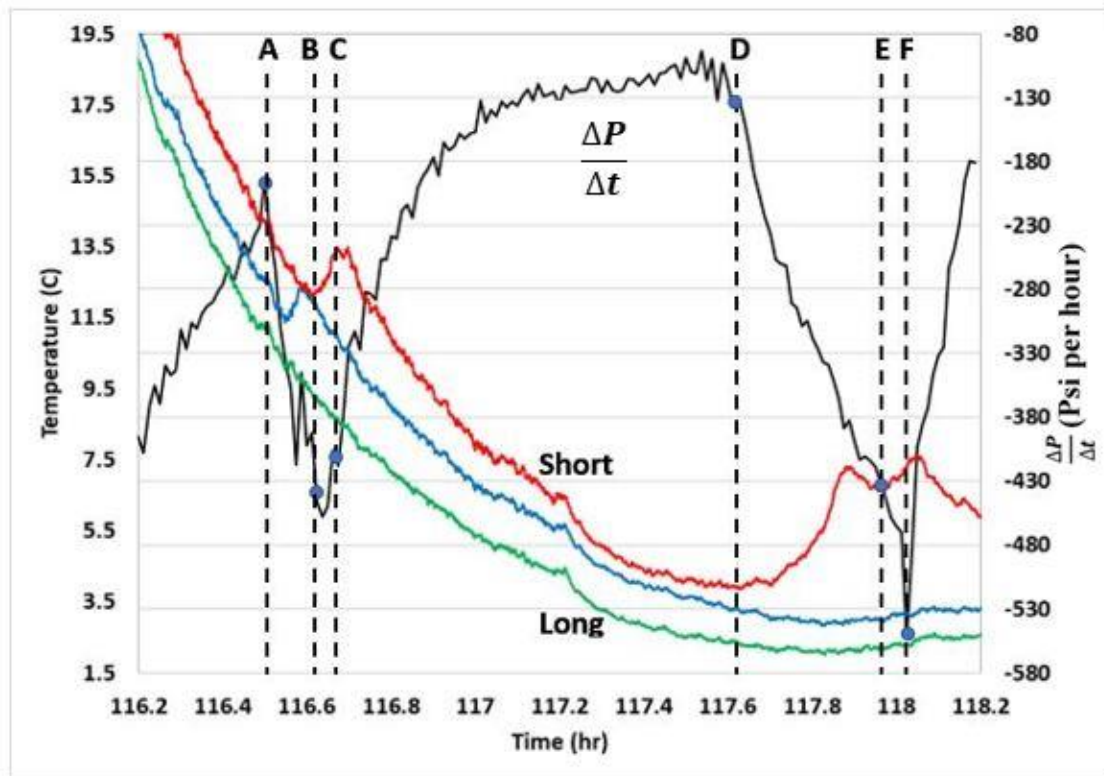
Figure III.7 Recorded histories of the temperature and time rate of pressure. Red, blue, and green are the temperature profiles recorded by the three thermocouples, and yellow is the time rate of pressure. Reprinted with permission from "Modeling of Hydrate Formation Hysteresis in Porous Media" by Authors' Jeremy Adams, I. Yucel Akkutlu, George Moridis, 2019. Society of Petroleum Engineers, Copyright [2019] by Society of Petroleum Engineers.

memory effect in cycle 4 and cycle 5, thus corroborating that hysteresis exists in a sand pack and that there is a temperature range at which it occurs.

In Figure III.7, the strong correlation between the temperature peaks and the hydrate consumption is shown. The time rate change of pressure is proportional to the hydrate formation because thermal effects are linear, and under a cooling environment, the pressure change should not increase but should be proportional to the cooling rate of the

47

system. However, in Figure III.7, a pressure change is not constant, nor is it just proportional to the cooling rate of the system. In Figure III.7, A is the location of the first major change in pressure rate and precedes the temperature peak by a small amount. It is seen that the pressure corresponds with all the thermocouples and not just one thermocouple. Thus, pressure represents the whole system, while the analysis of the temperature is restrained to the local area. Continuing to point B, the start of the lowest value of the pressure rate is observed. This corresponds with the medium thermocouple and recalling that the medium thermocouple is in the center of the sand pack and takes the longest to be affected by the thermal gradients, it makes sense that its temperature peak is later than the others.

By the time point, C is observed, the initial hydrate formation has leveled off, and there is an increasing pressure rate change until about 117.6 hours when a large increase in the medium thermocouple temperature is observed. Point D is the starting point of a drastic change in pressure rate, thus indicating large hydrate formation. At point E, the second temperature peak indicates further hydrate formation. At point F, the formation rate has subsided, and the pressure rate increases again.

3.1.4 Estimation of Hydrate Formation Rate and Amount

Thus, hydrate formation is observed at the temperature peaks, and the time of the temperature peaks corresponds with the onset of significant hydrate formation (Adams, Jeremy J., I. Yucel Akkutlu, and George J. Moridis, 2019)*. Therefore, these times can

be used to indicate hysteresis. The time derivative of pressure is not linear; thus, the

hydrate formation is nonlinear. This indicates that the system cannot be described by

singular activation energy, nor can it be described with a fixed reaction rate constant. A

possible change in the theory of hydrate formation would be not to use reaction rate

equations associated with the hydrate formation and melting; an approach that uses

Gibbs free energy (surface and bulk energy), maybe a better approach to hydrate

formation than the kinetic rate equations, due to the nature of hydrates being closer to a

mixture than a stoichiometric compound.

Knowing that the hydrate forms, the next question is how much has formed. To answer

this question, two fundamental information is needed, an equation of state for the

methane gas that takes the gas compressibility into account and predicts the gas pressure

in the sand pack from the temperature data, and pressure data from the experiment when

hydrates form. The difference between the real gas law and the experimental pressure

should be related to the hydrate formation. Redlich-Kwong equation of state (Eq.III-3) is

used for the study. To determine the initial moles of gas accurately and the volume of

methane used, the pressure and temperature data between 25 C and 16 C. The values for

the constants (a and b) are also fitted due to there being water in the system. This gives

TableIII-3, which shows the parameters that are used to predict the pressure.

$$\left(P + \frac{a}{\sqrt{T}\bar{V}(\bar{V}+b)}\right)(\bar{V} - b) = RT \hspace{3cm} \textbf{Eq. III-3}$$

To predict the amount of consumed methane, Newton-Raphson iteration is used to solve

for the number of moles at each experimental temperature and pressure. This means that

49

Table III-3 Initial conditions and coefficient for the Redlich-Kwong equation. Reprinted with permission from "Modeling of Hydrate Formation Hysteresis in Porous Media" by Authors' Jeremy Adams, I. Yucel Akkutlu, George Moridis, 2019. Society of Petroleum Engineers, Copyright [2019] by Society of Petroleum Engineers.

a	b	V (L)	n (mol)	$R \frac{L \cdot psi}{K \cdot mol}$
467.2337	0.02957	0.301	2.06	1.2059

only one variable is unknown and that for each set of temperatures, the moles of methane can be predicted. However, if this equation is solved by using the experimental values during the temperature spikes of the medium and short thermocouples, erroneous results will be seen. What is seen is that the number of moles of methane will increase due to the higher temperature, but it is known that the moles of gas is going down due to pressure decrease, therefore only the end of each cycle (when hydrate formation is almost zero) will the hydrate mass be calculated.

To calculate how much hydrate has formed, all that is needed is the relationship between moles of water and methane, which, assuming 100 percent hydration, is (CH_4) 5.75(H_2O), making the molecular mass of hydrate at 119.629 g/mole. From this data, the average hydrate formation rate can be calculated. The time period in between the time when hydrate begins to form and the end of the experiment represents the time of hydrate formation, and the total mass calculated at the end of the period divided by the period gives the average rate. Table III-4 shows the total mass of hydrate produced and the average rates. Note that the values vary; this is due to the period of time spent forming, which is different for each cycle.

Table III-4 The estimated hydrate amount formed and the rate of hydrate formation during each cycle. Reprinted with permission from "Modeling of Hydrate Formation Hysteresis in Porous Media" by Authors' Jeremy Adams, I. Yucel Akkutlu, George Moridis, 2019. Society of Petroleum Engineers, Copyright [2019] by Society of Petroleum Engineers.

Cycle	Hydrate Amount (g)	Hydrate Formation Rate (g/hr)	Cycle Period (Hrs)
1	61.19	3.59	17.01
2	61.74	2.60	23.68
3	41.09	1.76	23.30
4	61.74	2.64	23.38
5	62.30	4.06	15.36

Table III-5 The estimated water consumption in percent. Reprinted with permission from "Modeling of Hydrate Formation Hysteresis in Porous Media" by Authors' Jeremy Adams, I. Yucel Akkutlu, George Moridis, 2019. Society of Petroleum Engineers, Copyright [2019] by Society of Petroleum Engineers.

Cycle	Mass (g)	Percent Water Consumed
1	52.93	53.46
2	53.41	53.94
3	35.55	35.90
4	53.9	54.44
5	51.89	52.41

Important as well is the mass of the water. Given that there is 99ml of water or 99 grams of water in the system, the total conversion percentage can be calculated. From this data, which is Table III-5, a picture of what the water saturation profile can be deduced. This means that the potential to form hydrate is double of what was produced. So, this means that half of the water was not in contact with methane and validates the assumption that most of the water was at the bottom quarter of the sand pack with only a small amount in the upper section. Knowing the porosity, and the cross-sectional area, the portion of 100 percent saturated sand can be calculated to be 2.8 cm from the bottom of the sand pack, and the diagram can be seen in Figure III.8.

 The distribution of the other water is unknown.

3.1.5 Reaction Model in the presence of Hysteresis

In Table III-4, the measured values of the initial hydrate formation time values for the cycles are presented. In this part of the dissertation, we propose to develop a simple predictive tool for the initial hydrate formation time as a function of the melting temperature (Adams, Jeremy J., I. Yucel Akkutlu, and George J. Moridis, 2019)*. For this, we first normalize the recorded times in the presence of hysteresis by subtracting the initial time in the absence of hysteresis, Δt_{init}, which is the time that belongs to cycle 1. Following using the normalized initial times for Cycles 3, 4, and 5 and their corresponding melting temperatures to plot Figure III.8 and then linear fit the data points to predict the initial formation time based on the melting temperature as a straight-line relation.
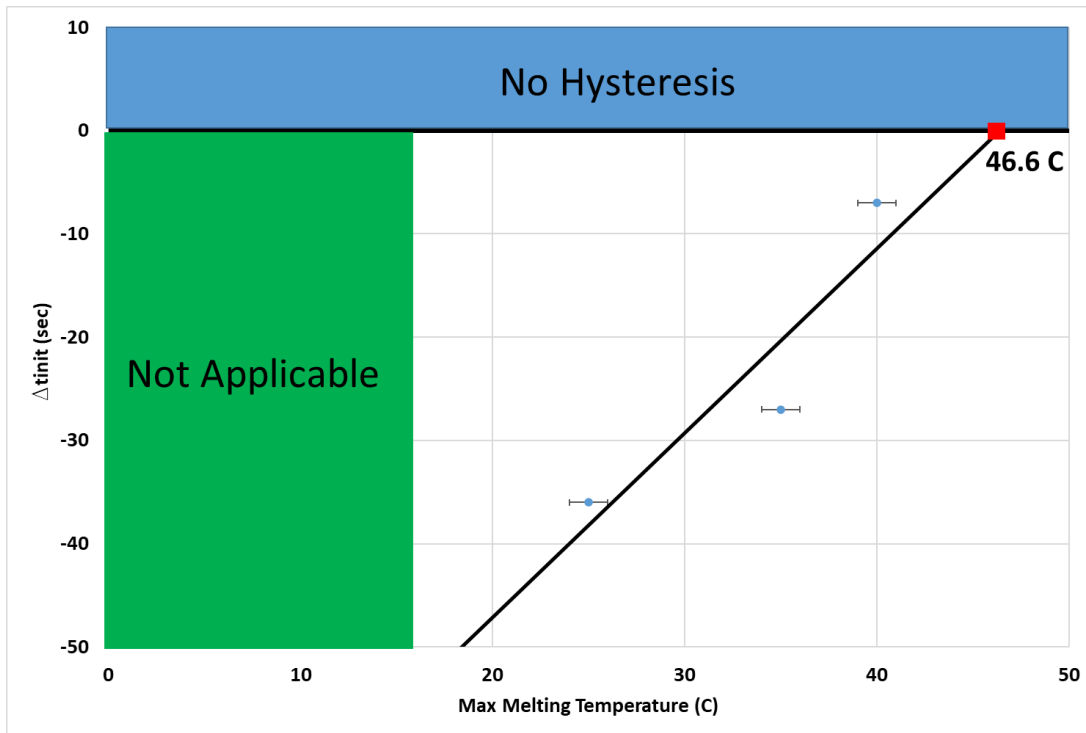
Figure III.8 Normalized initial formation time versus the maximum melting temperature for Cycles 3, 4, and 5. Reprinted with permission from "Modeling of Hydrate Formation Hysteresis in Porous Media.

In Figure III.8, the equation for Δt_{init} shows a clear trend the melting temperature has on the system. While the model (Eq. III-4) is simple, it shows that the higher the melting temperature is, the closer the system behavior to the first cycle in the absence of hysteresis (Δt_{init} =0). This develops at 46.4 C. On the other hand, when the melting temperature is lower; the initial hydrate formation develops sooner in the next cycle. This is true for melting temperatures, so the minimum temperature can only be the temperature just outside of the phase diagram, T_{Phase}, which is dependent on what pressure is used.

$$\Delta t_{init} = 1.7857 * T_{max,melt} - 82.857; \; T_{max,melt} > T_{Phase} \qquad \textbf{Eq. III-4}$$

The 36-second head starts that cycle 3 has over cycle 1 results in a 534-second head start in significant hydrate formation. The significant formation time is important because it signifies the start of the major thermal effects that hydrate has on the whole system. These thermal effects are what need to be understood so that a procedure to mitigate these effects can be developed and implemented.

Figure III.10 shows how the equilibrium pressure changes in the presence of the hysteresis. The higher the melting temperature is, the harder it is for the system initially form hydrates while at lower melting temperatures, the easier it is. The quadratic equation fits the data perfectly and is valid for temperatures from T_{Phase} up to 46.4C. Figure III.10 also shows the temperature at which hydrate forms when the hysteresis is present. As with the pressure, the same trend is seen, the higher the melting temperature is, the harder it is for hydrate to form while the lower melting temperature, the easier it is. Therefore, in order to implement the hysteresis, a shift in the pressure-temperature phase diagram is needed. This is done in equations Eq. III-5a and Eq. III-5b. To determine the change in the initial hydrate formation time that the hysteresis causes, the shift in the diagram are estimated in Eq. III-5a and Eq. III-5b.

$$T_{shift\,melt} = T_{eq} - (-6.57E^{-4}T_{melt}^2 + 3.31E^{-2}T_{melt} + 14.7) \qquad \text{Eq. III-5a}$$

$$P_{shift\,melt} = P_{eq} - (-1.67E^{-1}T_{melt}^2 + 8.39T_{melt} + 1770) \qquad \text{Eq. III-5b}$$

$$T_{eq}^* = T_{shift\,melt} + T_{eq} \qquad \text{Eq. III-6a}$$
$$P_{eq}^* = P_{shift\,melt} + P_{eq} \qquad \text{Eq. III-6b}$$
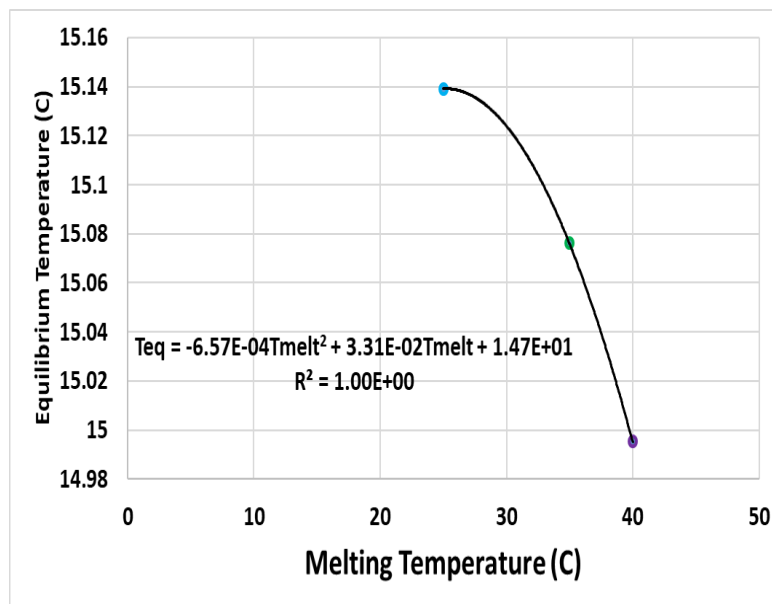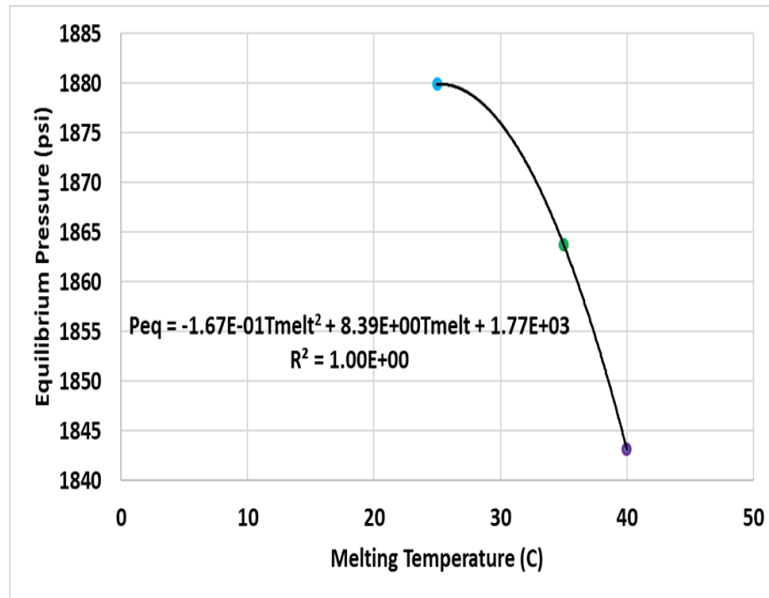
Figure III.9 Equilibrium pressure and temperature versus maximum melting temperature in presence of hysteresis. Reprinted with permission from "Modeling of Hydrate Formation Hysteresis in Porous Media. Reprinted with permission from "Modeling of Hydrate Formation Hysteresis in Porous Media" by Authors' Jeremy Adams, I. Yucel Akkutlu, George Moridis, 2019. Society of Petroleum Engineers, Copyright [2019] by Society of Petroleum Engineers.

T_{eq}^* and P_{eq}^* The modified equilibrium temperature and the modified equilibrium pressure, respectively, are then estimated using equations Eq. III-6a and Eq. III-6b. This represents a shift in the phase diagram to the right.

In Figure III.10, the flow chart for hydrate formation in the presence of hysteresis is illustrated. For the chart, we considered the hydrate formation algorithm for Tough+Hydrate based on the reaction rate equation of hydrate formation developed by Kim and Bishnoi [Kim, H. C., et al., 1987]. Kim and Bishnoi (1987) developed this equation by dissociating methane hydrate in a stirred-tank reactor by depressurization and the gas emitted captured and measured vs. time. This data was then used to develop Eq. III-7 by taking the dissociation rate and relating it to the difference in fugacity from equilibrium. There are two fugacities that are key to this equation, the first is the bulk fugacity of the methane at the hydrate equilibrium temperature and pressure, and the other is of methane when it is located very close to the surface of a hydrate particle. When this difference is negative, there is hydrate formation, and when it is positive, there is dissociation. The magnitude of the difference in fugacity is the major contributing factor of Eq. III-7. The other half of equation 7 is the traditional Arrhenius reaction rate equation, where there is the kinetic rate constant and activation energy. The kinetic rate of formation can be directly calculated using this formulation in a numerical simulation study. The necessary modification to the existing algorithm for the presence of the hysteresis is shown in red. The kinetic rate of hydrate formation is computed using the following formulation:

56

$$\frac{DQ}{dt} = k_o e^{-E_A/RT} A_s \left(P_{eq} \emptyset_{eq} - P_{CH_4} \emptyset \right) y_{CH_4} \qquad \text{Eq. III-7}$$

In Eq. III-7, the hysteresis comes into play through the driving force, which is represented by the parenthesis term. The drive basically represents the tendency of the water-gas system to form hydrate. In this case, it is measured as the difference in the fugacity values of methane on the surface of the hydrate particle at equilibrium and the methane in the bulk gas. In Eq. III-7, these fugacity values are represented by the fugacity coefficients multiplied by their respective pressures, (equilibrium pressure, and partial pressure for methane). The hysteresis should change the equilibrium fugacity of methane on the surface of the hydrate particle based on the shift in the equilibrium pressure and temperature. Currently, I am working on a thermodynamic model that captures hysteresis; the model will align with the residual cage theory of hysteresis and treat the cages as an additional compound in solution with water. Further details of my work are included in Appendix A.
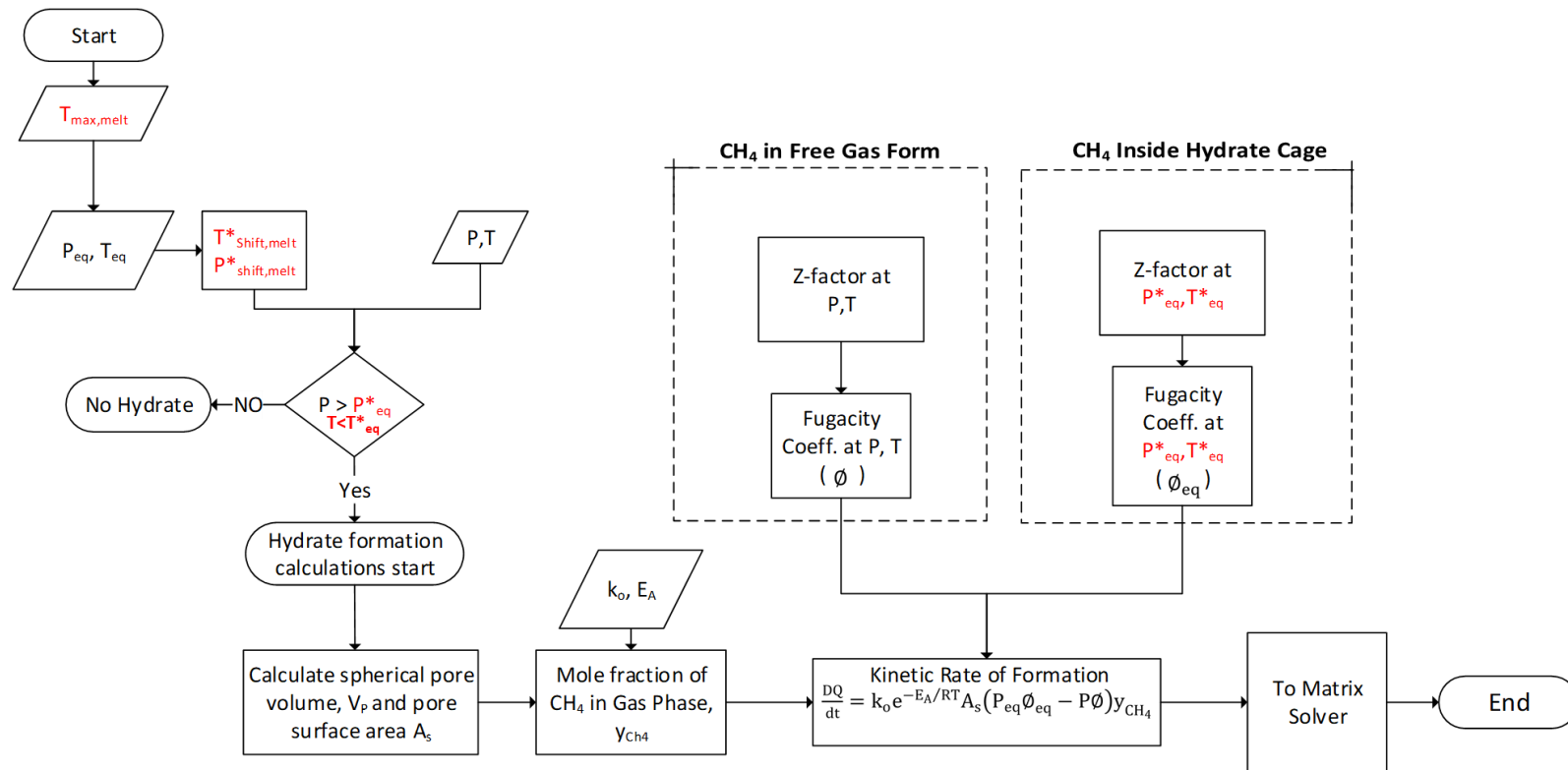
Figure III.10 Flow chart for Implementing Hysteresis into Tough+Hydrate. Necessary changes in the algorithm due to the presence of hysteresis is shown in red. Reprinted with permission from "Modeling of Hydrate Formation Hysteresis in Porous Media. Reprinted with permission from "Modeling of Hydrate Formation Hysteresis in Porous Media" by Authors' Jeremy Adams, I. Yucel Akkutlu, George Moridis, 2019. Society of Petroleum Engineers, Copyright [2019] by Society of Petroleum Engineers.

3.2 Gas Relative Permeability Discussion and results

3.2.1 Estimation of the Saturations using X-ray CT Scanning

To determine the saturations of water and hydrate, a medical x-ray CT scanner was used. The CT scanner uses constant size voxels, thus allowing for a simpler analysis of the corresponding images by being able to directly calculate the densities and, thus, the saturations of the sand pack by knowing the total number of voxels in the sand pack. The procedure is outlined below. Also, it should be noted that no doping agents were used to measure the densities.

CT scan data can be converted to density by using a calibration curve that relates the Hounsfield units to density in g/cm^3, thus allowing different calculations, such as saturations of water, hydrate, or porosity. To determine the water saturation in the sand pack from a CT image, the image is calibrated to a standard that relates densities of different materials to that of Hounsfield's units. Once this is done, the image is a map of density in g/cm^3, and a mass balance can be conducted. Eq. III-8 shows the mass balance in the absence of the methane hydrate phase.

$$\rho_{vox} = \frac{m_{vox}}{V_{vox}} = \frac{\rho_{sand}*V_{sand}+\rho_{Water}*V_p*S_w+\rho_{Ch4}*V_p*S_{CH4}}{V_{vox}} \qquad \text{Eq. \quad III-8}$$

Where ρ is the mass density and V_p is the pore volume of the sand-pack. Eq. III-8 can be changed to a mass base by multiplying both sides by the constant voxel volume, $V_{vox.}$ Eq. III-8 can then be reduced by eliminating the methane portion. This is possible due to the density of methane being relatively low. The value for methane is near zero on the

Table III-6 Parameters used for the estimation of saturations using x-ray CT.

V_{vox}	V_p	ρ_h	ρ_w
(cm³)	(cm³)	g/cm³	g/cm³
2.384e-5	8.583e-6	0.95	1.00

CT image. Thus, when the methane term drops out, Eq. III-9 is the resulting mass balance:

$$\rho_{vox} = \frac{m_{vox}}{V_{vox}} = \rho_{sand} * V_{sand} + \rho_{Water} * V_p * S_w \qquad \text{Eq. III-9}$$

Eq. III-10 is then solved for the water saturation S_{w1} in the absence of hydrate:

$$S_{w1} = \frac{V_{vox}\rho_{vox} - \rho_{sand} * V_{sand}}{\rho_{Water} * V_p} \qquad \text{Eq. III-10}$$

In the presence of hydrate:

$$\rho_{vox} = \frac{m_{vox}}{V_{vox}} = \frac{\rho_{sand} * V_{sand} + \rho_{Water} * V_p * S_{w2} + \rho_h * V_p * S_H}{V_{vox}} \qquad \text{Eq. III-11}$$

Here, S_{w2} is the water saturation in the sand pack presence of hydrate. Taking the difference of Eq. III-11 and Eq. III-9 results in Eq. III-12:

$$(\rho_{vox2} - \rho_{vox1})V_{vox} = (m_{w2} - m_{w1}) + m_H \qquad \text{Eq. III-12}$$

The difference in the masses of the two water saturations is the water content of the hydrate. It can be shown that the ratio of the molecular weights of the hydrate and the water is as in Eq. III-13:

$$m_W = \frac{M_W}{M_H} = \frac{1}{1.1469m_W}$$ **Eq. III-13**

In the voxel we have:

$$(m_{w2} - m_{w1}) = m_W$$ **Eq. III-14**

Taking Eq. III-14 and substituting into Eq. III-13 results in Eq.III-15:

$$m_H = \frac{\Delta\rho_{vox}V_{vox}}{1.87194}$$ **Eq. III-15**

Then, the hydrate saturation can be determined from the CT scan as:

$$S_H = \frac{V_{vox}*\Delta\rho_{vox}}{1.87194\rho_H*V_p}$$ **Eq. III-16**

Once the hydrate saturation is determined, the free water content in the sand pack can be calculated too. With some algebra Eq. III-16 can be obtained for the water saturation in the presence of hydrate:

$$S_{w2} = \frac{1.1469m_{w1} - m_H}{1.1469\rho_{Water}*V_p}$$ **Eq. III-17**

Eq. III-10 is used to map the water saturations. Eq. III-16 represents hydrate saturation. The densities of the sand-pack before and after the hydrate formation are subtracted from each other, i.e., with the hydrate minus no hydrate. This results in a positive value for hydrate and zero or negative for no hydrate. The mass of hydrate is then solved by assuming the hydration number is equal to 6, and the residual water is calculated by Eq. III-17, by which this residual water will be used in the relative permeability measurements.

Table III-7 shows the constants used for the calculations above.

3.2.2 Experimental Results

3.2.2.1 Steady-State Single-phase (Gas) Flow Experiments

Now, we discuss the steady-state single-phase (gas) flow experiments for the sand pack. First is the gas flow in the absence of hydrate. Note that gas flows in the presence of water with a fixed saturation value. Figure III.14 shows the graphical representation of Darcy's equation as a straight line with the slope equal to 5.9757e-8. The y-axis is the fluid flow rate divided by the cross-sectional area of the sand pack perpendicular to the flow, and the x-axis is the pressure-square difference divided by the length of the sand pack. The slope is then the mobility (k/μ) of the sand-pack. Taking the viscosity of methane at 18C equal to 10.6x10-6 Pascal-second, the permeability of the sand pack without hydrate was measured as 0.660 Darcy. Figure III.14 (bottom) shows the water saturation distribution in the sand pack with no hydrate after the gas flow experiment was completed. (In the CT images presented in chapter 3, the inlet of flow is on the left, and the outlet is on the right.) The water saturation in the sand pack can be considered uniform; the only exception is the high-water saturation area to the right of the center,
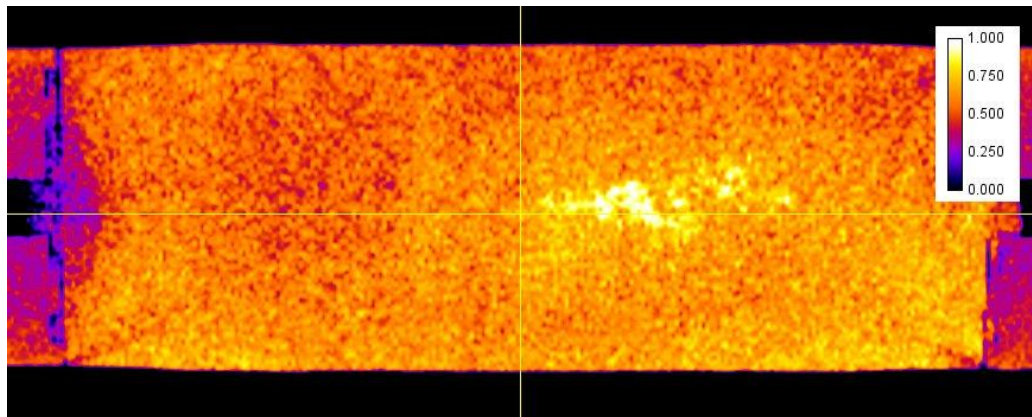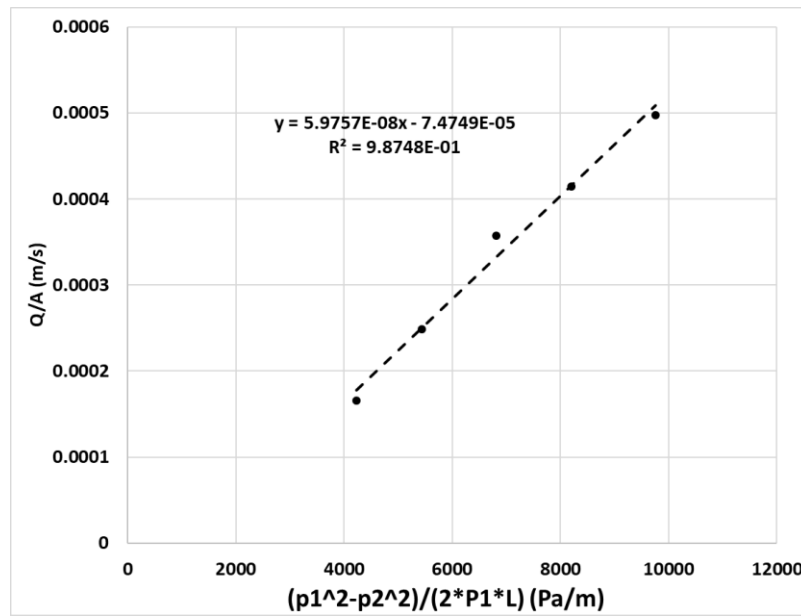
Figure III.11 TOP: Rate versus applied pressure drop during the steady-state single-phase (gas) flow without hydrate in the sand pack. The slope is the mobility and used to estimate the absolute permeability of the sand. BOTTOM: Water saturation distribution in the sand pack at the end of the gas flow experiment.
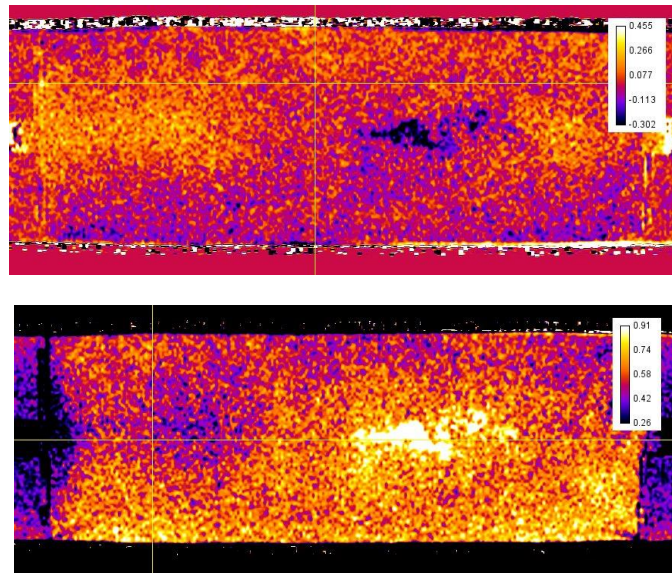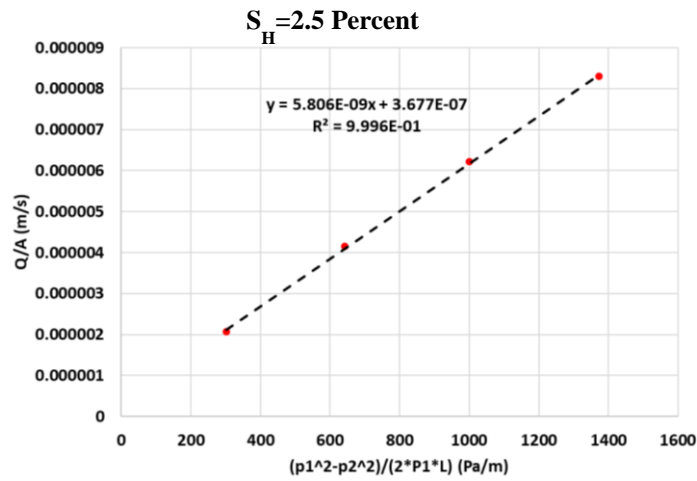
Figure III.12 TOP: Rate versus applied pressure drop during the steady-state single-phase (gas) flow with hydrate in the same sand pack in Figure III.2. Again, the slope is used to determine the permeability of the sand. MIDDLE: Saturation of hydrate in the sand pack after the hydrate formation. Hydrate forms at higher water saturations. Dark region near the center has less hydrate saturation due to low gas availability; therein, the water saturation is near 100%. BOTTOM: Residual water saturation in the sand pack after the hydrate formation. This shows a lowered water value when compared to (a).
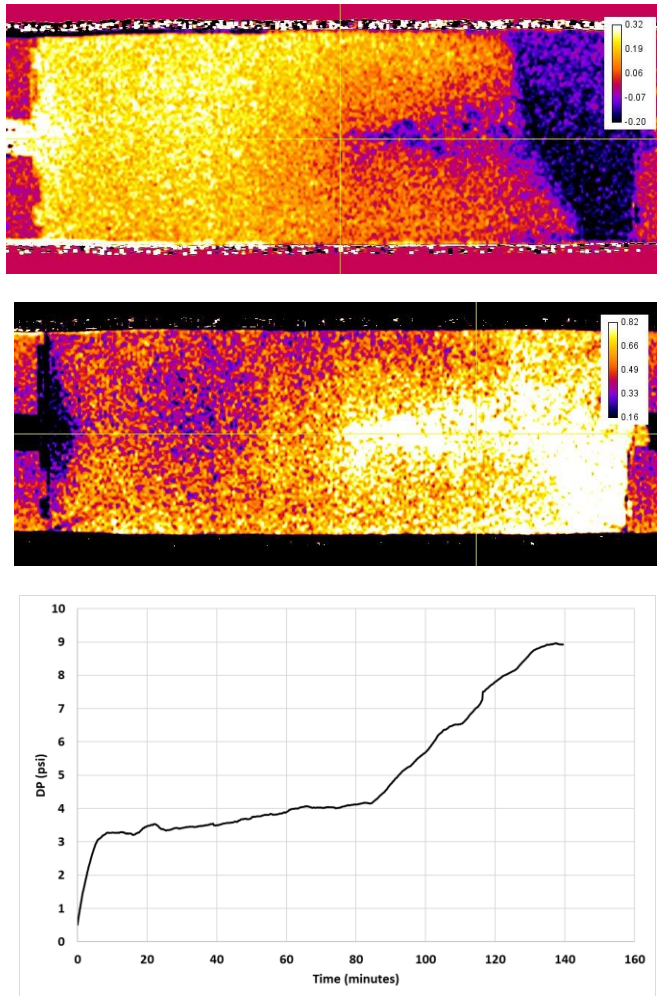
Figure III.13 (TOP) Hydrate saturation in the sand pack after one pore volume of water is injected into the sand pack. The line between light and dark is a dissociation Figure III.13 Continued: front caused by the pressure drop at the outlet of the sand pack. (MIDDLE) Residual water saturation in the same sand pack, showing at the downstream region on the right, the melted hydrate area with high water saturation. In contrast, the hydrate-bearing upstream region on the left has lower water saturation. (BOTTOM) Differential pressure response during the single-phase (gas) flow. This shows that the system was blocked by the hydrates completely, and no flow through the sand pack was occurring.

65

shown as the origin of the coordinate system in yellow. The sand pack is estimated to have an average of 58% water saturation. This leaves a 42% gas saturation for the circulation at different rates during the permeability estimation.

Figure III.15 includes the steady-state single-phase (gas) flow and permeability measurements for the sand pack in the presence of methane hydrate. This experiment belongs to the scanned sand in Figure III.14. Using the same approach, the permeability is now estimated to be 0.064 Darcy, which indicated a one-order magnitude reduction in the permeability of the sand pack. Indeed, the hydrate formation causes a significant reduction in permeability. The data includes only four flow rates due to limitations on the cooling rate of the injecting fluid heat exchanger. Figure III.15 (middle) shows the hydrate saturation once the sand pack was cooled, and hydrate crystallization took place. Here, the bright orange and white-colored areas are hydrate rich regions, and the blue and red are dryer areas. The formation of hydrate causes a change in the pore network filled with water and gas. This leads to increases in the capillary pressure and draws the water to the hydrate rich regions, thus causing a non-uniform saturation profile. The average hydrate saturation in the sand pack is 2.5 percent.

In order to see the impact of higher hydrate saturation on the flow, we increased the water saturation in the sand pack. Figure III.16 Top shows the sand pack now with an average 18% hydrate saturation. The gas flow experiment at this hydrate saturation showed that the sand pack was no longer permeable. This resulted from injecting a

66
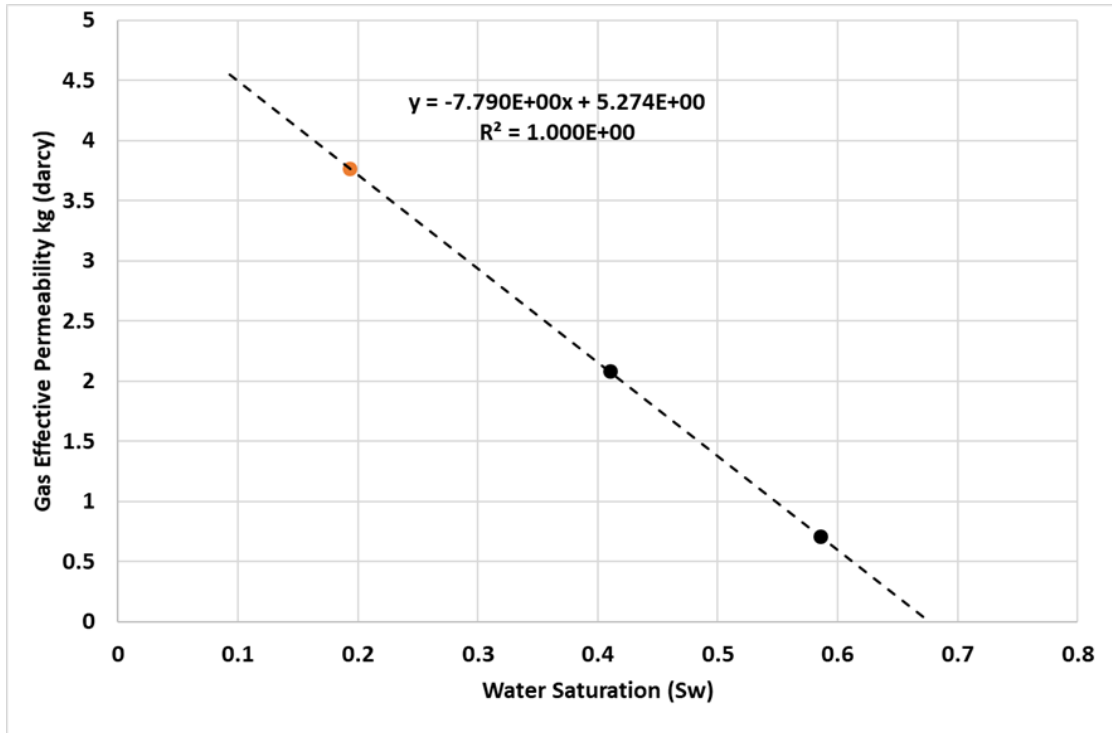
Figure III.14 Effective gas permeability versus water saturation using single-phase flow experiments. Orange data point is a different sand pack than the black points, thus a different packing. The results show that the packing has a negligible impact on the effective gas permeability estimation.

significant volume of water into the system and increasing the average water saturation

and forming hydrate to such an extent that the flow system became impermeable to gas

Figure III.16 Middle shows the high levels of water saturation (Sw2) in the sand pack.

Figure III.16 Bottom shows the transient nature of the differential pressure measured

during the gas injection. Clearly, the pressure is not stabilized and kept increasing during

the flow measurement, which is indicating the lack of filtration in the sand pack.
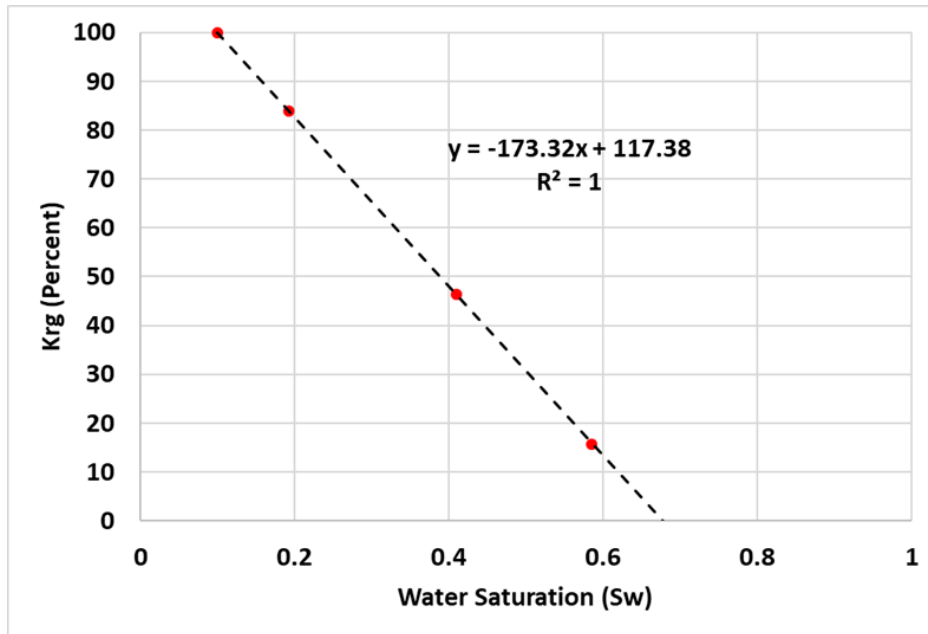
Figure III.15 Relative permeability to gas in the sand pack in the absence of hydrates using single-phase flow experiments. Critical gas saturation is predicted at 10% irreducible water saturation at 67%.

The hydrate in the sand pack is melted, and the system is returned to the 20C and 500 psi to perform the flow measurements at various water saturation levels in the absence of methane hydrate. First, we measure the effective gas permeability as a function of the water saturation. The following discusses the construction of the relative gas permeability curve.

FigureIII.17 shows the measured effective gas permeability values as a function of the water saturation. Since the sand was sifted the permeability variations are expected to be low due to packing. As expected, the results showed a linear relationship between the effective gas permeability and gas saturation. When the gas saturation in the sad pack
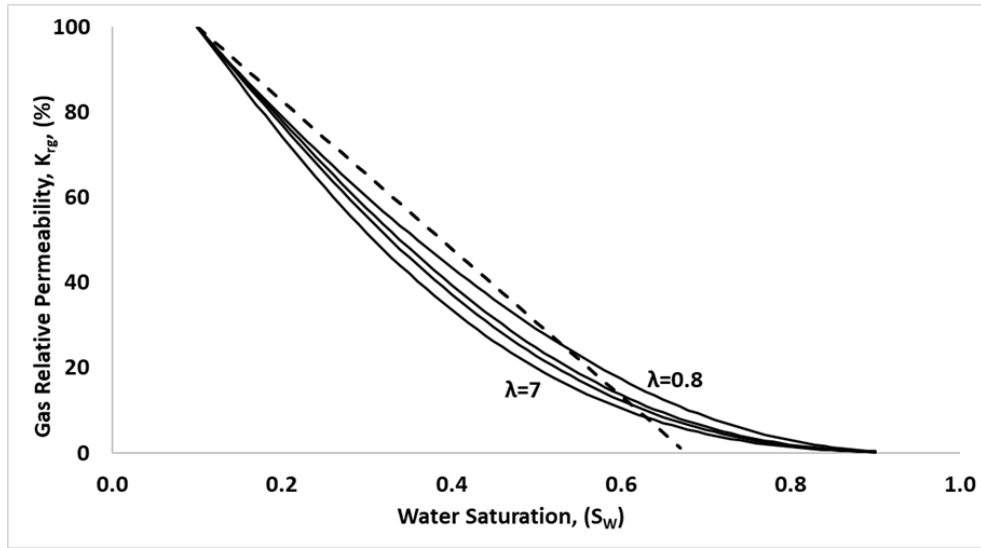
Figure III.16 Comparison of the laboratory-measured single-phase (gas) flow data to Brooks and Corey model curves with varying pore size distribution index values $\lambda=0.8$, 2, 3, and 7.
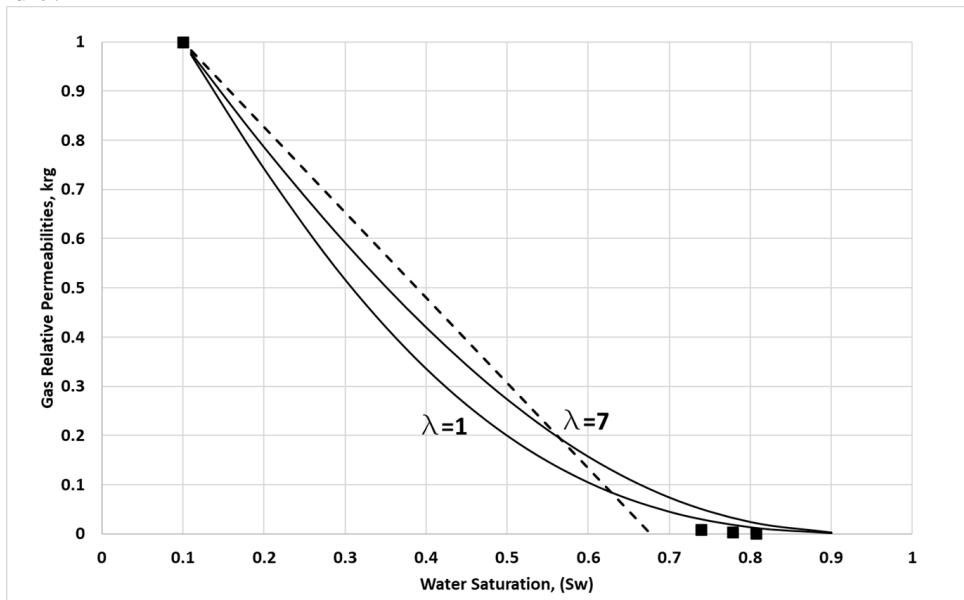
Figure III.17 Comparison of the laboratory-measured single-phase (gas) flow data to Li et al. (2004) model curves with varying pore size distribution index values $\lambda=1$, and 7.

To estimate the relative permeability values, a reference effective gas permeability value

was increased, the effective gas permeability improved. We suggest formulating this

relationship using linear regression as follows:

$$k_g = 7.8 * S_g - 2.53 \qquad\qquad \textbf{Eq. III-18}$$

was needed, which is often the effective gas permeability at the irreducible water saturation. 10% water saturation was chosen as the irreducible water saturation of the sand pack from the literature (Naar et al., 1962) due to constraints in time and scope of the experiment. Using Eq. III-18, the resulting gas effective permeability at the irreducible water saturation is predicted using 4.49 Darcy.

Figure 17 shows the Li et al. (2004) relative permeability model, which, in this case, is similar to the Brooks and Corey correlation. The advantage of Li et al. (2004) model is the maximum and entry capillary pressure values can be estimated.

At this point, the relative permeability is defined as the effective permeability divided by the permeability at irreducible water saturation:

$$k_{rg} = \frac{k_g}{k_{g\,@S_{w,irr}}} = \frac{k_g}{4.49} \qquad\qquad \textbf{Eq. III-19}$$

Figure III.16 shows the gas relative permeability in the sand pack in the absence of methane hydrates using the steady-state single-phase (gas) flow experiment.

When the gas relative permeability of the sand pack in the absence of hydrate is compared to the Brooks and Corey equation (shown below as Eq. III-20),
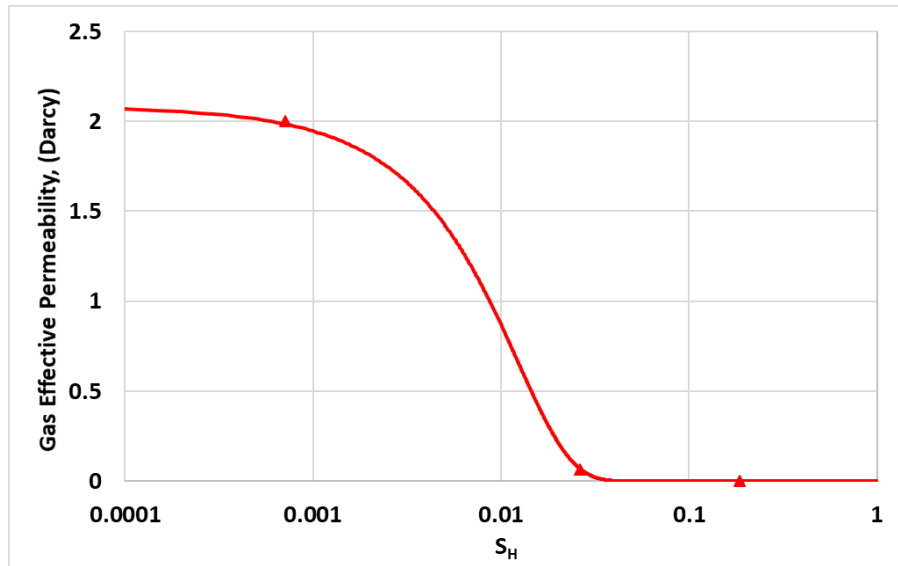
Figure III.18 Effective gas permeability versus hydrate saturation based on the steady-state single-phase (gas) flow experiments.
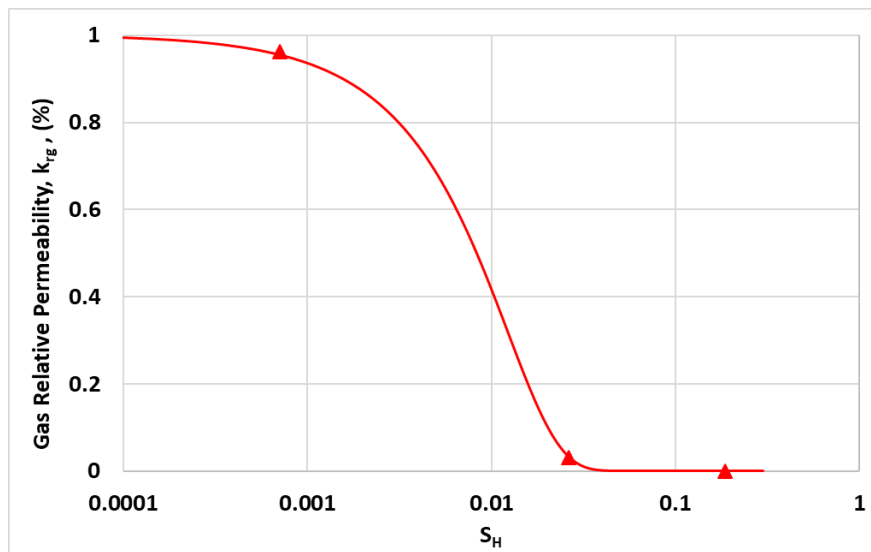
Figure III.19 Relative gas permeability versus hydrate saturation at different average water saturation in the sand pack. From left to right, relative permeability goes from 100% permeability at Sw =41% to 1.42% permeability at Sw =57%, 0% permeability at Sw =43%.
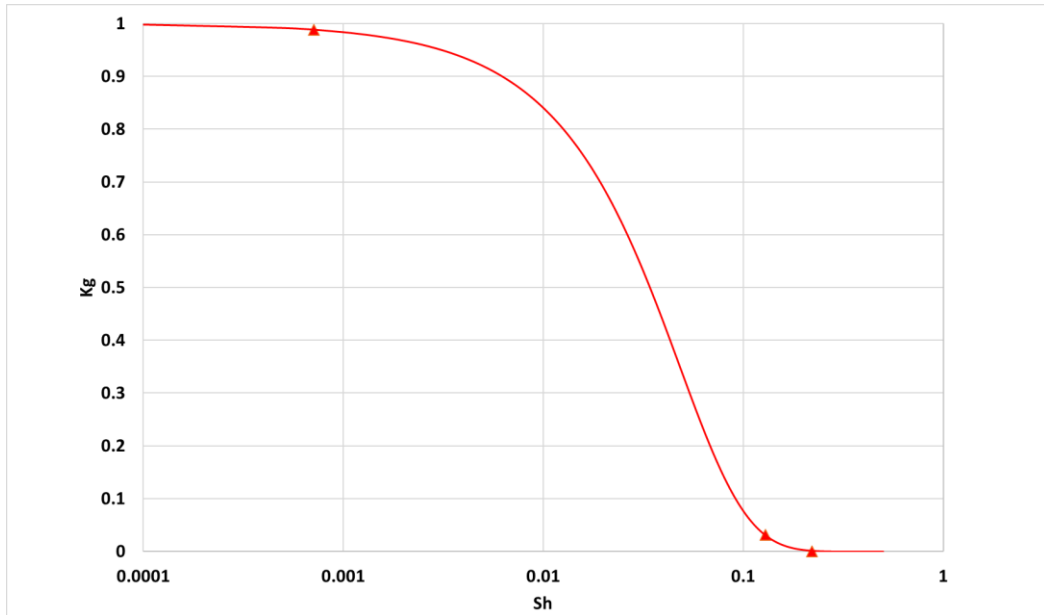
Figure III.20 Relative gas permeability versus hydrate saturation using hyperbolic tangent at different average water saturation in the sand pack. From left to right, relative permeability goes from 100% permeability at Sw =41% to 1.42% permeability at Sw =57%, 0% permeability at Sw =43%.

$$k_{rg} = \left(\frac{1-S_w}{1-S_{wirr}}\right)^2 \left[1 - \left(\frac{S_w-S_{wirr}}{1-S_{wirr}}\right)^{\frac{2+\lambda}{\lambda}}\right] \qquad \text{Eq. III-20}$$

we found out that the shape of the experimental relative permeability curve (which is linear) is not the same as the model curves, see Figure III.16. The experimental values, shown as black dashed line, appear to be a straight-line approximation to the Brooks and Corey model. Varying pore size distribution index (λ) values are used for comparison. The model does not match the relative gas permeability behavior of the sand pack

Table III-7 The values of Eq. III-23

$x = \frac{a}{b} * S_H$	Eq. III-22	Eq. III-23
0	0	0.00
0.1	1.179847	1.61
0.2	2.359693	3.21
0.3	3.53954	4.82
0.4	4.719386	6.43
0.5	5.899233	8.03
0.6	7.07908	9.64
0.7	8.258926	11.25
0.8	9.438773	12.85
0.9	10.61862	14.46

reasonably. We will re-visit the model comparison later, while we discuss the multi-phase flow experiment results.

Figure III.18 shows the effective gas permeability as a function of the hydrate saturation. A severe drop in effective permeability is observed at relatively low values of hydrate saturation during the gas flow experiments.

73

$$k_g = k_{g@S_H=0} \times \left[1 + erf\left(-\frac{a}{b} * S_H\right)\right] \qquad \text{Eq. III-21}$$

$$k_{rg} = \left(\frac{k_{g@S_H=0}}{k_{g@S_H=0, S_{wirr}}}\right)\left(1 + tanh\left(-\frac{a}{b}S_H\right)\right) \qquad \textbf{Eq. III-23}$$

Here a/b=11.8 and has the units of (pore volume)/ (hydrate volume).

In Figure III.18, the effective permeability at S_H =0 is equal to 2.0072 Darcy at the corresponding water saturation $S_{W1}=S_{W2}=41\%$. This value is the effective gas permeability obtained using Eq. III-21 (or Figure III.19). Table 7 column 2 shows some values of equation III-22.

Figure III.19 shows the relative permeability to gas versus hydrate saturation in the presence of hydrate using the single-phase flow experiments. The best fit for this data is the following exponential decline:

$$k_{rg} = \left(\frac{k_{g@S_H=0}}{k_{g@S_H=0, S_{wirr}}}\right)\left[1 + erf\left(\frac{a}{b} * S_H\right)\right] \qquad \textbf{Eq. III-22}$$

Using the hyperbolic tangent, we can get the same results as the error function, but with a better result at higher hydrate saturation, this is due to the hyperbolic tangent not going to zero as fast as the error function, thus allowing the models to show very low flow rate.

A: ERF
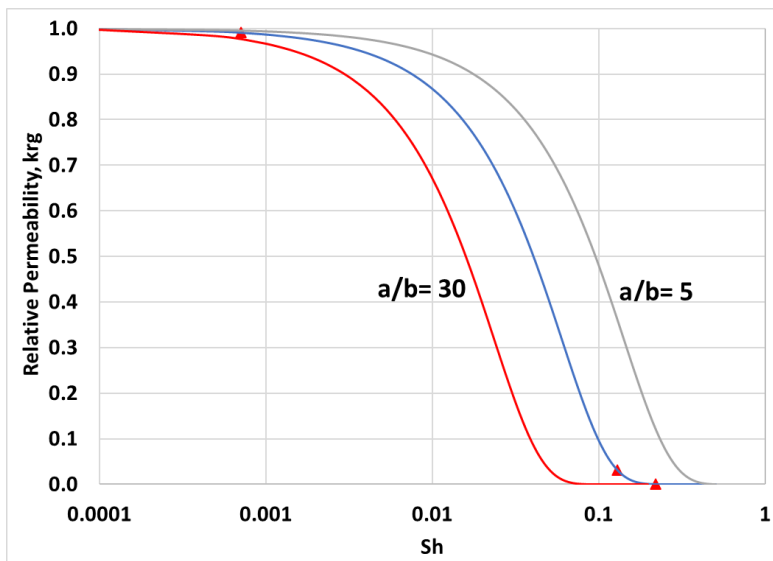
B: tanh
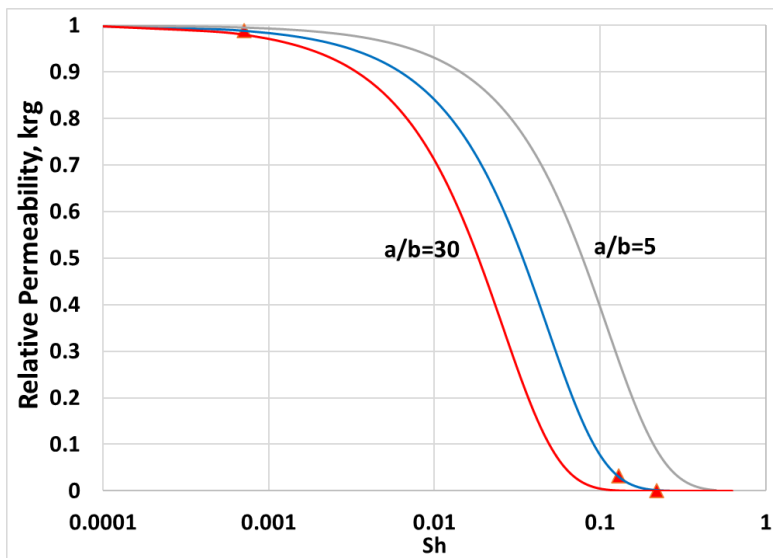
Figure III.21: Relative permeability correlations using the A: The Error Function where a/b from left to right is 30, 12 and 5 and B: The Hyperbolic Tangent Function, where a/b from left to right is 30, 17 and 5.

Figure III-21 shows how Eq III-22 and Eq. III-23 change when using different values of the a/b ratio. Table III-7 column 3 shows some of the values for the equation

75

representing hydrate relative permeability decrease as a function of hydrate saturation using equation III-23. Figure III-21 shows how Eq III-22 and Eq. III-23 change when using different values of the a/b ratio. Note that relative permeability reduction develops at significantly lower hydrate saturation levels, as a/b ratio of the porous medium is increased. This indicates that the ratio could physically be related to the total pore volume (or porosity) such that increasing pore volume will require a larger volume of hydrates forming and filling up the pores, which lead to plugging of the critical flow paths of the porous medium, such as pore throats.

Thus, it can be concluded here that the presence of hydrate has a significant effect on the relative permeability of the gas, but as the hydrate is removed, the system returns to that relative permeability in the absence of hydrate. Next, we will discuss the results for the steady-state multiphase flow experiments.

3.2.3 Steady-State-Multi-Phase (Gas/Water) Flow Experiments

Now we shall discuss the steady-state multiphase flow experiment results. Figure III.22 shows the water saturation distribution of the sand pack at the end of the three separate stages of flow experiments where different rates of water and gas are injected. Figure III.22A shows the saturation distribution after 3 pore volumes of fluids were injected at the flow rates of 8 ml/min methane to 4 ml/min of water. The water saturation in the

A. 8ml/min Gas-4ml/min Water
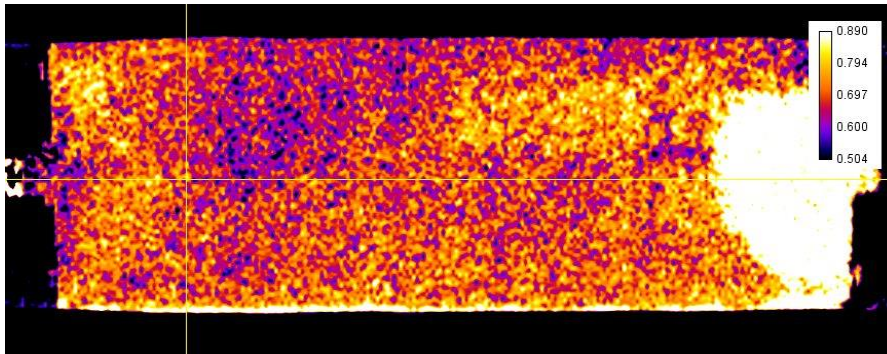
B. 6ml/min Gas-6ml/min Water.
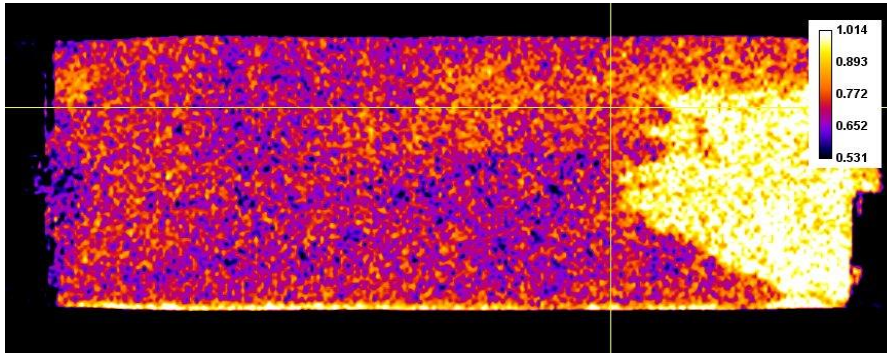
C. 4ml/min Gas-8ml/min Water
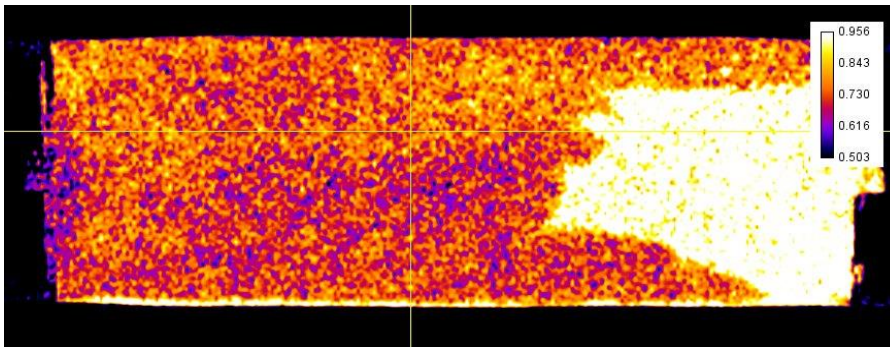
Figure III.22 Water saturation distribution at the end of three stages of steady-state two-phase simultaneous gas/water flow experiments at room temperature, in the absence of methane hydrate.
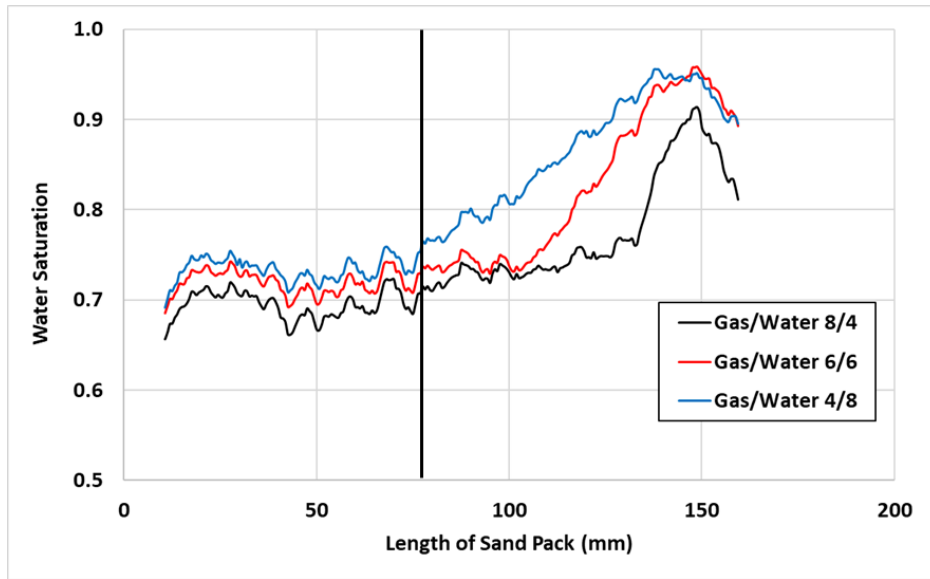
Figure III.23 Average water saturation profile along the main direction of flow during the relative permeability tests that were performed at three different rates at room temperature. Only values left of the 75 mm line will be used due to non-realistic water saturations near the outlet (left).

Table III-8 Average Water saturation values used in the Permeability Analysis.

Injection Rates as Ratio, Q_g/Q_w	8ml/min Gas, 4ml/min Water	6ml/min Gas, 6ml/min Water	4ml/min Gas, 8ml/min Water
Average Water Saturation, %	74	78	81

sand pack ranges from 89 % with the white voxel to about 55 percent with the blue

voxel. This also shows that the saturation profile is not uniform; the bright spot is seen to

be coalescing water phase preferentially exiting through the center of the sand pack.

Figure III.22B shows the case when water and gas phases are injected at the same rate,

78

both at 6 ml/min. See how the overall saturations change, there are fewer blue voxels and, more orange voxels indicating a global saturation increase. The bright cone near the outlet is also increasing in length, thus indicating that this phenomenon could be linked to the flow ratio at the inlet, not to the total amount of water injected. Increasing water injection rate causes the water flowing through new flow paths (new saturation branches) to merge, and the average water saturation to increase. Figure III.22C shows the impact of further increasing water rate on the water saturation field. Note that the water cone on the right is getting larger. Figure III.23 shows an increase in water saturation near the outlet of the sand pack. The end cap of the sand pack at the outlet is on the axis of the sand pack, thus, causes the water to merge close to the exit. This causes an increase in the saturation and the marked increase in differential pressure. Since the development of the water cone is associated with the outlet boundary, the values of saturation that can be used during the multi-phase flow experiments will only contain the values in the absence of the cone, including the saturation within 10mm-75mm portion of the sand pack. This separation is indicated in Figure III.23 with a vertical line. Table III-8 shows the average water saturation values corresponding to that portion of the sand pack, where the saturation varies somewhat more uniformly, but in the presence of some fluctuations.
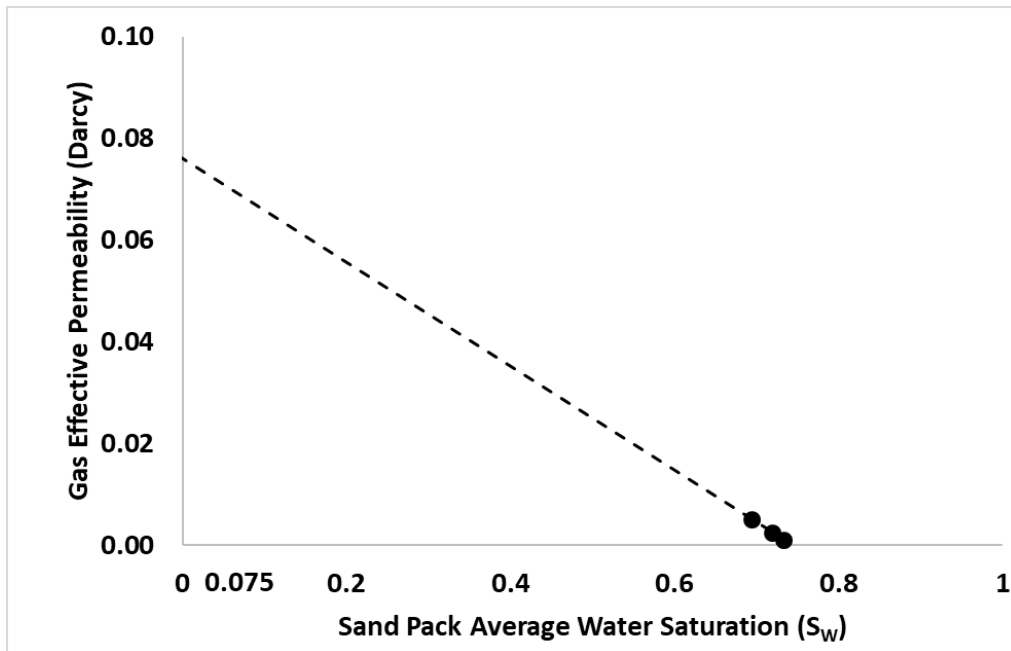
Figure III.24 Gas effective permeability with no hydrate obtained using multi-phase flow experiments.

Figure III.24 shows the effective gas permeability in the absence of hydrate using the multi-phase flow experiment. Note that the domain of water saturation is very narrow and in near 70% water saturation. The three points at different injection rates of gas and water give a perfectly straight line for effective permeability. Extrapolating to 10% irreducible water saturation gives the gas permeability equal to 0.07 Darcy. This value is significantly lower than that using the single-phase gas flow experiment data. We use this value for the calculation of the relative permeability values. The result is shown in FigureIII.25.
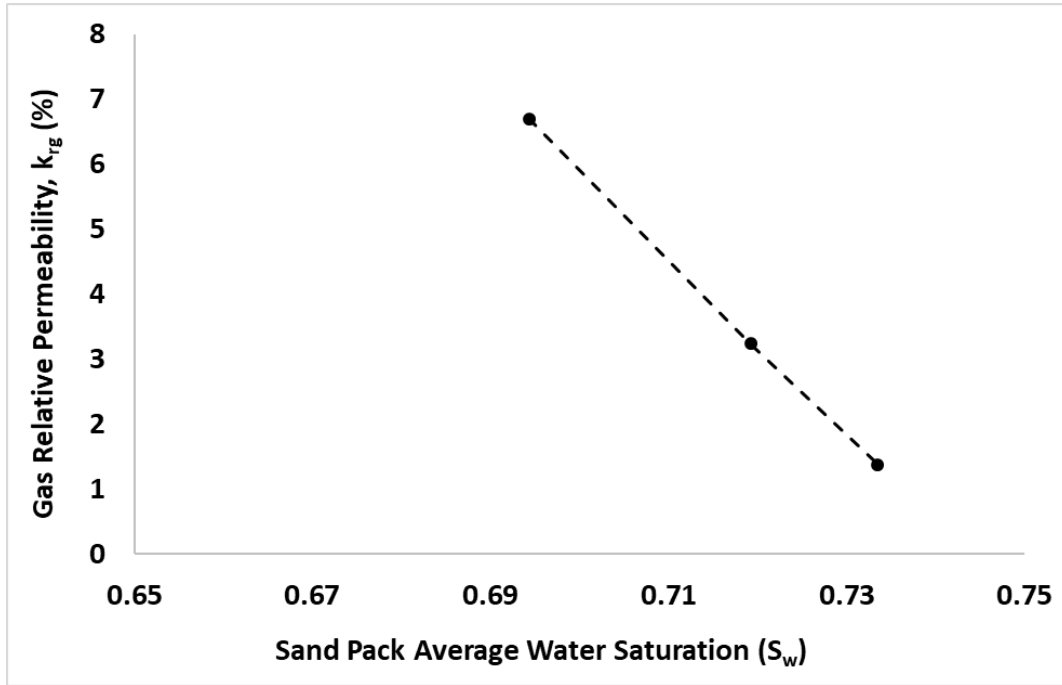
Figure III.25 Relative permeability to gas in the sand pack in the absence of hydrates using multi-phase flow experiments.

Figure III.26 shows the gas relative permeability of the sand pack versus water saturation compared to the Brooks and Corey model. Clearly, the model matches the relative permeability in the absence of hydrates reasonably for λ value close to 7, which corresponds to unconsolidated sand.

$$k_g = -0.1022S_W + 0.0759 \hspace{3cm} \text{Eq. III-23}$$

$$k_{rg} = -136.22S_W + 101.26 \hspace{3cm} \text{Eq. III-24}$$

Figure III.26 shows a comparable model to the brooks' and Corey Correlation. And since this is so close to the Brooks and Corey Correlation, it corroborates our findings.

Based on the experimental results, the following final discussions can be made. Of the two different methods that are described in Sections III.3.4.2 and 3.4.4.1, Section

III.3.4.1 (single-phase steady-state flow) experiments are recommended due to direct measurement of the effective and relative permeability values in the presence of hydrate. The steady-state multi-phase (gas/water) flow experiments work well with no hydrate present, but when hydrate is present the two components either form new hydrate, or the hydrate present dissociates. These develop locally in the sand pack and are due to either a chemical imbalance or temperature differences. In our experiments, they have led to erratic saturations when the relative permeability cannot be measured in the presence of hydrates. So, this chapter recommends using the method laid out in section III.3.4.1.

The Li and Horne Model is a good alternative, and as shown in figure III-27, the shape is similar to the brooks' and Corey correlation as in figure III-26.

For a sand pack with similar characteristics, the following equations can be used to determine the effective and relative permeability:
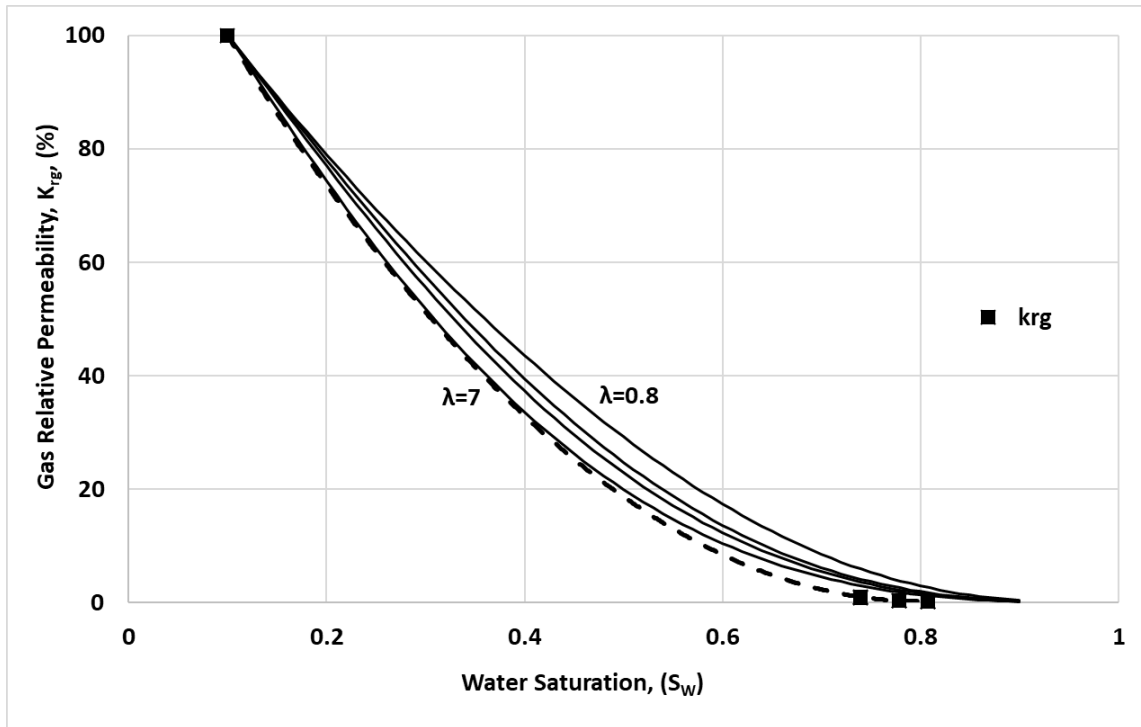
Figure III.26 Comparison of the laboratory-measured relative permeability data in the absence of hydrate to Brooks and Corey model type curves with varying pore size distribution index values λ=7, 3, 2, 0.8.

$$k_{rg} = 202.75S_W{}^2 - 325.02S_W + 130.47 \qquad \text{Eq. III-25}$$
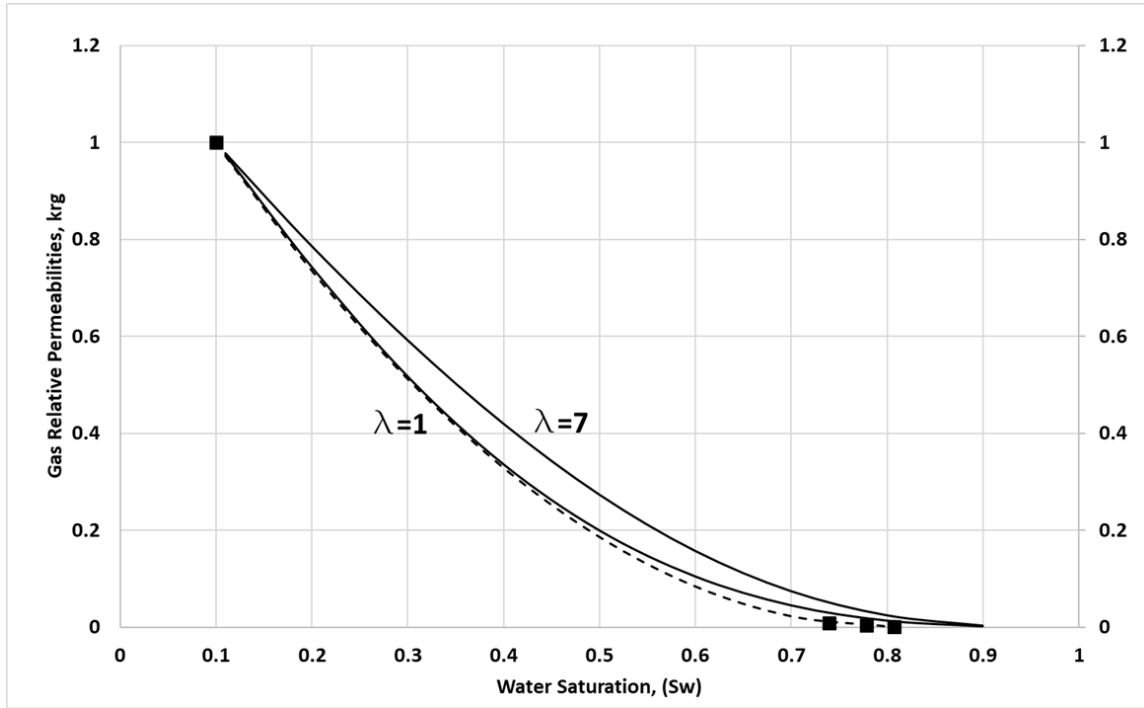
Figure III.27 Comparison of the laboratory-measured relative permeability data in the absence of hydrate to Li and Horne model type curves with varying pore size distribution index values λ=7, 1.

In the absence of hydrate:

$$k_g(S_W) = -0.1022S_W + 0.0759 \qquad \text{Eq. III-26}$$

$$k_{rg}(S_W) = -136.22S_W + 101.26 \qquad \text{Eq. III-27}$$

In the presence of hydrate:

$$k_g(S_H) = k_{g@S_H=0} \times \left[1 + erf\left(-\frac{a}{b} * S_H\right)\right] \qquad \text{Eq. III-28}$$

$$k_{rg}(S_H) = \left(\frac{k_{g@S_H=0}}{k_{g@S_H=0,S_{wirr}}}\right)\left[1 + erf\left(\frac{a}{b} * S_H\right)\right] \qquad \text{Eq. III-29}$$

$$k_{rg}(S_H) = \left(\frac{k_{g@S_H=0}}{k_{g@S_H=0,\,S_{wirr}}}\right)\left(1 + Tanh\left(-\frac{a}{b}S_H\right)\right) \qquad \text{Eq. III-30}$$

To use Eq. III-28and Eq. III-29, it is important to first determine the effective and relative permeability values as in Eq. III-26 and Eq. III-27. Eq. III-28 and Eq. III-29 is used for the effective and relative permeability values in the presence of hydrate, and the value at zero hydrate saturation needs to be on the same line is in Eq. III-26 and Eq. III-27, this ensures that the values are consistent and representative of the system. Equivalently, Eq. III-30 can be used as well to describe the system and, in some cases, maybe better since it goes to zero slower than the error function.

CHAPTER IV

CONCLUSIONS

4.1 Phase Equilibria

In this article, the presence of hysteresis during hydrate formation in porous media is shown using an experimental approach. The measured pressure and temperature time series are dependent on the past runs, which is, by definition, a hysteresis. Furthermore, the change in the temperature and pressure profiles are dependent on the hydrate formation rate. Further corroborating the existence of hydrate formation at the temperature peaks is the time derivative of the pressure, in which the decrease in pressure drop corresponds with the increase in temperature, and increases when the temperature decreases; thus, the hydrate rate has a direct effect on the pressure change. Therefore, any equations formulated need to have second-order effects to capture this dependence. Thermal effects come into play that is not present in the bulk experiments. Thermal confinement was a major factor of the temperature peaks that were observed, which indicates when the hydrate is forming rather rapidly. Furthermore, these temperature peaks are at the location of a valley in the temperature profile. Thus, a perfectly insulated system would produce a greater thermal peak than one that is not insulated. This feature could be used as a metric of when hydrates are forming or when they are not forming significantly. Melting temperatures clearly matter, and the closer the system is to the equilibrium line, the more pronounces the thermal effects become; conversely, the further away the starting point is, the more important the hysteresis

effects are. As a certain point (35 C) was reached for the melting temperature, most effects of the hysteresis were eliminated, and by only 40 C, there was negligible difference between the runs. This means that for thermally dissociated media, the system must be heated quite high to eliminate secondary hydrate formation.

Hydrate mass was estimated by solving for the number of moles of bound gas in the system from the Redlich-Kwang equation of state at the observed pressure and temperature and then using the stoichiometric relation for methane hydrate. Furthermore, it was found that most runs produced the same mass, indicating that there was not a large water saturation difference between the runs. There was a small region (around 2.8 cm) that was 100 percent saturated with water, thus preventing the entirety of the available water from forming into hydrate.

A simple predictive model was developed and shown to follow the trends of the experimental data. The model results are important because initial hydrate formation time is proportional to the significant hydrate formation, which is when the forming hydrate starts affecting the system thermally. Correlations of melting temperature versus equilibrium pressure and melting temperature versus equilibrium temperature are shown so that the phase diagram can be modified to account for hysteresis by shifting the values of the phase diagram by the shifted values. This relation is then implemented into the Kim and Bishnoi kinetic model that the simulation software Tough+Hydrate uses. Future work could be to study hysteresis under constant temperature while varying pressure to form and dissociate the hydrate, and to investigate the dissolved gas amount during and after hydrate formation. Also, to increase the number of maximum melting temperatures,

for example, 17-45 C, would make a finer grid (more cycles) of the melting temperatures to the formation times (both initial and significant formation).

4.2 Gas Relative Permeability in the Presence of Hydrate

In conclusion, hydrates restrict the flow of water and gas when in a single-phase or in 2 phases. The complex interaction that arises from 2-phase flow in a hydrate-bearing sand pack adds challenges to the measurements of relative permeability and effective permeability due to the temperature and pressure requirements. Furthermore, capillary pressure can cause water to travel to the high hydrate regions causing non-uniform hydrate saturations, but if the hydrate is formed in layers, this effect is mitigated. Hydrate restricts the flow of gas by 10 times when there is an increase of hydrate from zero to 2.5 percent average. The low hydrate saturation indicates that it forms in the pore throats rather than pore body filling. Variation in hydrate saturation follows the initial water saturation, and any water saturation changes are due to the injection of water. Hydrate at 18 percent stops all flow, and pressure on the outlet side decreased to below the equilibrium pressure and start dissociation. The use of single-phase gas flow in the measurement of gas relative permeability is recommended due to the complex formation and dissociation effects have when injecting both water and methane. Furthermore, the water-gas interaction as a two-phase flow in the auxiliary pipes cloud the results of the sand pack, thus again, the single gas-phase measurements are the clear winner here.

REFERENCES

Azzi, A., et al., 2010, Gas-liquid two-phase flow division at a micro-T-junction, *Chemical Engineering Science* 65.13: 3986-3993.

Bagherzadeh, S. A., Moudrakovski, I. L., Ripmeester, J. A., & Englezos, P. (2011). Magnetic Resonance Imaging of Gas Hydrate Formation in a Bed of Silica Sand Particles. *Energy & Fuels, 25*(7), 3083-3092. doi:10.1021/ef200399a

Buchanan, P., Soper, A. K., Thompson, H., Westacott, R. E., Creek, J. L., Hobson, G., & Koh, C. A. (2005). Search for memory effects in methane hydrate: structure of water before hydrate formation and after hydrate decomposition. *The Journal of chemical physics, 123*(16), 164507.

Folas, Georgios K., et al. "Application of the cubic-plus-association equation of state to mixtures with polar chemicals and high pressures." *Industrial & engineering chemistry research* 45.4 (2006): 1516-1526.

Chen, Guang-Jin, and Tian-Min Guo. "Thermodynamic modeling of hydrate formation based on new concepts." *Fluid Phase Equilibria* 122.1-2 (1996): 43-65.

Huang, Stanley H., and Maciej Radosz. "Equation of state for small, large, polydisperse, and associating molecules: extension to fluid mixtures." *Industrial & Engineering Chemistry Research* 30.8 (1991): 1994-2005.

Gupta, A., Lachance, J., Sloan, E. D., & Koh, C. A. (2008). Measurements of methane hydrate heat of dissociation using high pressure differential scanning calorimetry. *Chemical Engineering Science, 63*(24), 5848-5853. doi:https://doi.org/10.1016/j.ces.2008.09.002

Delli, M.L., and Grozic, J.L.H., 2014, Experimental determination of permeability of porous media in the presence of gas hydrates, J. *Petroleum Science and Engineering* 120: 1-9

Honarpour, M., Mahmood, S.M., 1988, Relative-permeability measurements: An overview, *Journal of petroleum technology* 40.08: 963-966.Kim, B. Y., & Akkutlu, I. Y. (2017). *A New Laboratory Setup for Phase Equilibria Studies of Methane Hydrate in Porous Media.* Paper presented at the Advances in Laboratory Testing and Modelling of Soils and Shales.

Johnson, A., Patil, S., Dandekar, A., 2011, Experimental investigation of gas-water relative permeability for gas-hydrate-bearing sediments from the Mount Elbert Gas Hydrate Stratigraphic Test Well, Alaska North Slope, *Marine and Petroleum Geology* 28.2: 419-426.

Kneafsey, T.J., et. al., 2010, Permeability of laboratory-formed methane-hydrate-bearing sand: measurements and observations using X-ray computed tomography.

Lee, J. D., Susilo, R., & Englezos, P. (2005). Kinetics of structure H gas hydrate. *Energy & Fuels, 19*(3), 1008-1015.

Lekvam, K., & Ruoff, P. (1997). Kinetics and mechanism of methane hydrate formation and decomposition in liquid water. Description of hysteresis. *Journal of Crystal Growth, 179*(3), 618-624. doi:https://doi.org/10.1016/S0022-0248(97)00166-8

Linga, P., Haligva, C., Nam, S. C., Ripmeester, J. A., & Englezos, P. (2009). Gas Hydrate Formation in a Variable Volume Bed of Silica Sand Particles. *Energy & Fuels, 23*(11), 5496-5507. doi:10.1021/ef900542m

Max, M.D., 2003, ed. *Natural Gas Hydrate in Oceanic and Permafrost Environments*. Vol. 5, Springer Science & Business Media.

McGuire, P. L. (1981). *Methane hydrate gas production : evaluating and exploiting the solid gas resource*.

Moridis, G. J., Collett, T. S., Boswell, R., Kurihara, M., Reagan, M. T., Koh, C., & Sloan, E. D. (2009). Toward Production From Gas Hydrates: Current Status, Assessment of Resources, and Simulation-Based Evaluation of Technology and Potential. *SPE Reservoir Evaluation & Engineering, 12*(05), 745-771. doi:10.2118/114163-PA

Moridis, G. J., Kowalsky, M. B., & Pruess, K. (2007). Depressurization-Induced Gas Production From Class-1 Hydrate Deposits. *SPE Reservoir Evaluation & Engineering, 10*(05), 458-481. doi:10.2118/97266-PA

Moridis, G.J., Sloan, E.D., 2007, Gas production potential of disperse low-saturation hydrate accumulations in oceanic sediments, *Energy Conversion & Management* 48.6: 1834-1849.

Naar, J., Wygal, R.J., Henderson, J.H., 1962, Imbibition relative permeability in unconsolidated porous media, Society of Petroleum Engineers Journal 2.01: 13-17.

Ohmura, R., Ogawa, M., Yasuoka, K., & Mori, Y. H. (2003). Statistical study of clathrate-hydrate nucleation in a water/hydrochlorofluorocarbon system: Search for the nature of the "memory effect". *The Journal of Physical Chemistry B, 107*(22), 5289-5293.

Oyama, H., Konno, Y., Masuda, Y., & Narita, H. (2009). Dependence of Depressurization-Induced Dissociation of Methane Hydrate Bearing Laboratory Cores on Heat Transfer. *Energy & Fuels, 23*(10), 4995-5002. doi:10.1021/ef900179y

Pini, R., Benson, S.M., 2013, Simultaneous determination of capillary pressure and relative permeability curves from core-flooding experiments with various fluid pairs, *Water Resources Research* 49.6: 3516-3530.

Rees, E. V., Kneafsey, T. J., & Seol, Y. (2011). Methane hydrate distribution from prolonged and repeated formation in natural and compacted sand samples: X-ray CT observations. *Journal of Geological Research, 2011*.

Rodger, P. M. (2000). Methane hydrate: melting and memory. *Annals of the New York Academy of Sciences, 912*(1), 474-482.

Seol, Y., & Myshakin, E. (2011). Experimental and Numerical Observations of Hydrate Reformation during Depressurization in a Core-Scale Reactor. *Energy & Fuels, 25*(3), 1099-1110. doi:10.1021/ef1014567

Seol, Y., Kneafsey, T.J., 2011, Methane hydrate induced permeability modification for multiphase flow in unsaturated porous media, *Journal of Geophysical Research: Solid Earth* 116.B8.

Yamamoto, K., Terao, Y., Fujii, T., Ikawa, T., Seki, M., Matsuzawa, M., & Kanno, T. (2014). *Operational overview of the first offshore production test of methane hydrates in the Eastern Nankai Trough*. Paper presented at the Offshore Technology Conference, Houston, Texas. https://doi.org/10.4043/25243-MS

Kontogeorgis, Georgios M., and Georgios K. Folas. *Thermodynamic models for industrial applications: from classical and advanced mixing rules to association theories*. John Wiley & Sons, 2009.

Michelsen, Michael L., and Eric M. Hendriks. "Physical properties from association models." *Fluid phase equilibria* 180.1-2 (2001): 165-174.

Kim, H. C., et al. "Kinetics of methane hydrate decomposition." *Chemical engineering science* 42.7 (1987): 1645-1653.

Li, Kewen, and Roland N. Horne. "Universal capillary pressure and relative permeability model from fractal characterization of rock." *Twenty-Ninth Workshop on Geothermal Reservoir Engineering, Stanford University, California. Vol. SGP-TR-75*. 2004.

Plug, W-J., and J. Bruining. "Capillary pressure for the sand–CO2–water system under various pressure conditions. Application to CO2 sequestration." *Advances in Water Resources* 30.11 (2007): 2339-2353.

Sloan Jr, E. Dendy, Carolyn A. Koh, and Carolyn Koh. Clathrate hydrates of natural gases. CRC press, 2007.

Brooks, R., and T. Corey. "Hydraulic Properties of Porous Media." Hydrology Papers, Colorado State University 24 (1964): 37.

Adams, Jeremy J., I. Yucel Akkutlu, and George J. Moridis. "Modeling of Hydrate Formation Hysteresis in Porous Media." *SPE Europec featured at 81st EAGE Conference and Exhibition*. Society of Petroleum Engineers, 2019.

APPENDIX A

THERMODYNAMIC MODEL OF HYDRATE FORMATION WITH

HYSTERESIS

Theory

In this section of the dissertation, I introduce a statistical thermodynamic model that considers methane hydrate formation in the presence of hysteresis. The approach couples the reaction model of [Chen, Guang-Jin,1996] to form stoichiometric hydrate with the cubic-plus-association equation of state (CPA EoS).

Chen and Guo [Chen, Guang-Jin,1996] reaction model considers a two-step statistical thermodynamic process. Firstly, a quasi-chemical reaction is defined in two types of cavities: a large cavity and a linked cavity. Secondly, they considered the absorption of the gas molecule into the empty linked cavities, resulting in a complete hydrate. The CPA EoS is then used to determine the fugacity and activity coefficients of the gas and liquid phases, respectively. As a final step, the P-T phase diagram is constructed, when the chemical potential or fugacity values of the two phases are equal.

The CPA EoS takes any cubic equation of state (most common ones are the Soave-Redlich-Kwong (SRK) or Peng-Robinson EoS models) and adds an association term inherited from the Wertheim perturbation theory. The associative contribution is significant for liquids and polar compounds that have strong hydrogen bonding or other nonbonding forces, such as electrolytes.

The phase diagram is determined by assuming a temperature and pressure and calculating all the required fugacities of the system at that pressure and temperature.

This is a repetitive process when the iterating calculations continue until the set tolerances in the calculated fugacities are satisfied. Figure IV.1 shows the flow diagram of the reaction model coupled with the CPA EoS.

The first step in the approach is to estimate the pressure or temperature of the P-T phase diagram of methane hydrate. The iterative process is applied at each pressure or temperature of interest. Consider that x_i and y_i are the mole fraction of the species in the liquid phase and the mole fraction in the gas phase, respectively. The first step is to calculate the activity of water, which is the ratio of the fugacity coefficients of the water-melt hydrate cluster? (or water-gas?) a mixture to that of the pure water using the CPA EoS. The parameters for pure liquid are found from linear regression.

$$\gamma_w = \frac{\rho_w}{\rho_w^0} \qquad \text{Eq. IV-1}$$

This allows for the fugacity relating to the structure to be calculated in the next step, which is dependent on the number of gas molecules per water molecule, as seen in Eq. III-7. Equations IV-2 through IV-4 are the contributions of pressure and temperature.

$$f^0(a_w) = a_w^{-1/\lambda_2} \qquad \text{Eq. IV-2}$$

$$f^0(P) = exp\left(\frac{\beta P}{T}\right) \qquad \text{Eq. IV-3}$$

$$f^0(T) = A' exp\left(\frac{B\prime}{T - C\prime}\right) \qquad \text{Eq. IV-4}$$

Assume Initial Values of P

Flash Calculation CPA EoS

xi, yi

´Ywi

$f^0(aw)$

$f^0(T)$

$f^0(P)$

f^0

f

$|fi-f| \leq e$

Save T

Choose another P

No
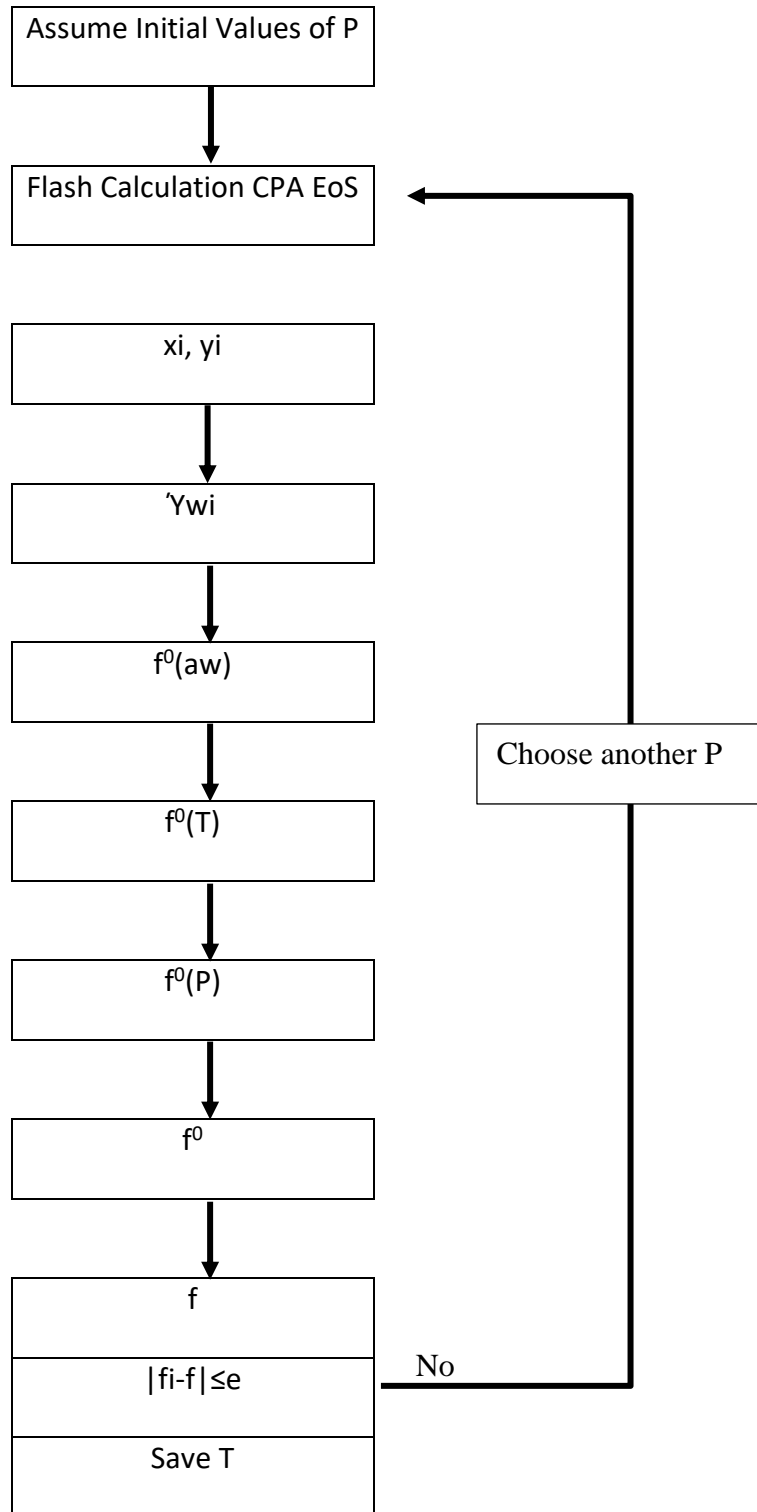
Figure IV.1 Chen and Guo reaction model [Chen, Guang-Jin,1996] coupled with CPA EoS [Folas, 2006].

Equation IV-5 represents the contribution of temperature, pressure, and water activity to

the fugacity of the gas in the cages, and the contribution of the occupancy of the linking

cages. λ_2 is the number of gas molecules per water molecules in the basic hydrate.

$$f^0 = f^0(T)f^0(P)f^0(a_w) \qquad \text{Eq. IV-5}$$

$$f = f^0(1 - \theta)^\alpha \qquad \text{Eq. IV-6}$$

$$\sum_j \theta_j^* = \frac{\sum_j f_j^g C_j}{1 + \sum_j f_j^g C_j} \qquad \text{Eq. IV-7}$$

λ_1 is the number of linked cavities per water molecule. a_w is the fraction of λ_1 to λ_2.

The i phase represents the gas or the liquid or the hydrate phase. Before continuing the

description of the CPA EoS and its application and how it is solved is required.

The pressure explicit version of the CPA EoS is as follows:

$$p = \frac{RT}{v-b} - \frac{a}{v(v+b)} - \frac{1}{2}\frac{RT}{v}\left[1 + \rho\frac{\partial \ln g}{\partial \rho}\right]\sum_i x_i \sum_{A_i}(1 - X_i^A) \qquad \text{Eq. IV-8}$$

Here, the last term on the right-hand side of Eq. IV-8 is the associative term of

the Wertheim perturbation theory.

Figure IV.2 Diagram showing partially melted hydrate cage with attractive sites for gas absorption and clathrate formation [Huang, 1991]

x_i denotes mole fraction of component i in the liquid, X_i^A is the fraction of sites A on

molecules i which do not form bonds with other active sites. These are based on further

97

equations that dictate association strength and the radial distribution functions and reduced density. *a(T)* is the energy parameter of the traditional SRK EoS, and **b** is the co-volume constant of the traditional SRK EoS.

The specifics of the terms in the CPA EoS are as follows. The fraction of the non-bonding sites is calculated using:

$$X_i^A = \frac{1}{1 + \rho \sum_j x_j \sum_{B_j} X_j^B \Delta^{A_i B_j}}$$

Eq. IV-9

Figure IV-2 shows a diagram of water and the possible location of hydrogen bonding sights using the 4C method, which states where bonding can take place and the probability of bonding occurs, [Huang, 1991]. For water the bonding probability is assumed to be symmetric. Let's take an example of how to expand Eq. III-16. The summation is over all sites other than the site being calculated and produces the system of equations as seen in III-17

$$\begin{bmatrix} X_1^A - \dfrac{1}{1 + \rho_{l,v} * x_1 * (X_1^B \Delta^{A_1 B_2} + X_1^C \Delta^{A_1 C_2} + X_1^D \Delta^{A_1 D_2}) + \rho * x_2 * (X_2^B \Delta^{A_2 B_2} + X_2^C \Delta^{A_2 C_2} + X_2^D \Delta^{A_2 D_2})} = 0 \\ X_1^B - \dfrac{1}{1 + \rho_{l,v} * x_1 * (X_1^A \Delta^{B_1 A_2} + X_1^C \Delta^{B_1 C_2} + X_1^D \Delta^{B_1 D_2}) + \rho * x_2 * (X_2^A \Delta^{B_2 A_2} + X_2^C \Delta^{B_2 C_2} + X_2^D \Delta^{B_2 D_2})} = 0 \\ X_1^C - \dfrac{1}{1 + \rho_{l,v} * x_1 * (X_1^A \Delta^{C_1 A_2} + X_1^B \Delta^{C_1 B_2} + X_1^D \Delta^{C_1 D_2}) + \rho * x_2 * (X_2^A \Delta^{C_2 A_2} + X_2^B \Delta^{C_2 B_2} + X_2^D \Delta^{C_2 D_2})} = 0 \\ X_1^D - \dfrac{1}{1 + \rho_{l,v} * x_1 * (X_1^A \Delta^{D_1 A_2} + X_1^B \Delta^{D_1 B_2} + X_1^C \Delta^{D_1 C_2}) + \rho * x_2 * (X_2^A \Delta^{D_2 A_2} + X_2^B \Delta^{D_2 B_2} + X_2^C \Delta^{D_2 C_2})} = 0 \end{bmatrix}$$

Eq. IV-10

Eq. IV-10 describes the association strength between similar molecules, such as the interaction between two water molecules and between other associating molecules. For

the case with methane and water system, the only fully associating compound is water, and since the association is assumed to be symmetric that means that the $\Delta^{A_i B_j}$ terms are equal for the water-water inaction, thus Eq.IV-10 simplifies to Eq. IV-11

$$\begin{bmatrix} X_1^A - \dfrac{1}{1+\rho_{l,v}*x_1*\Delta^{A_1 B_2}*(X_1^B+X_1^C+X_1^D)} = 0 \\[2ex] X_1^B - \dfrac{1}{1+\rho_{l,v}*x_1*\Delta^{A_1 B_2}*(X_1^A+X_1^C+X_1^D)} = 0 \\[2ex] X_1^C - \dfrac{1}{1+\rho_{l,v}*x_1*\Delta^{A_1 B_2}*(X_1^A+X_1^B+X_1^D)} = 0 \\[2ex] X_1^D - \dfrac{1}{1+\rho_{l,v}*x_1*\Delta^{A_1 B_2}*(X_1^A+X_1^B+X_1^C)} = 0 \end{bmatrix} \qquad \text{Eq. IV-11}$$

Eq. IV-12 is the term for the association strength between sites. This is the most important part of the CPA EoS since this defines the molecular interaction between molecules.

Association Strength $\Delta^{A_i B_j}$ in Eq. III-17 is calculated using

$$\Delta^{A_i B_j} = g(\rho)^{ref} \left[exp\left(\frac{\varepsilon^{A_i B_j}}{RT}\right) - 1 \right] b_{ij} \beta^{A_i B_j} \qquad \text{Eq. IV-12}$$

where

$$b_{ij} = \frac{b_i + b_j}{2} \qquad \text{Eq. IV-13}$$

and $g(\rho)$ is the radial distribution function defined as follows:

$$g(\rho) = \frac{1}{1-1.9\eta} \qquad \text{Eq. IV-14}$$

We defined the reduced density function

$$\eta = \frac{b\rho}{4} \qquad \text{Eq. IV-15}$$

$\varepsilon^{A_i B_j}$ is the association energy, $\beta^{A_i B_j}$ is the association volume.

For the terms A_iB_j appearing in Eq. III-9 through Eq. III-12, the conventional van der Wall's mixing rule applies.

$$a(T) = a_0 \left(1 + c_1\left(1 - \sqrt{T_r}\right)\right)^2 \qquad \text{Eq. IV-16}$$

$$a_{mix} = \sum_i \sum_j x_i x_j a_{ij} \qquad \text{Eq. IV-17}$$

$$a_{ij} = \sqrt{a_i a_j}(1 - k_{ij}) \qquad \text{Eq. IV-18}$$

$$b = \sum_i b_i x_i \qquad \text{Eq. IV-19}$$

For cross-association of mixtures, the energy and radial distribution are as follows

$$b_{ij} = \frac{\varepsilon^{A_iB_i} + \varepsilon^{A_jB_j}}{2} \qquad \text{Eq. IV-20}$$

$$\beta^{A_iB_j} = \sqrt{\beta^{A_iB_i} * \beta^{A_jB_j}} \qquad \text{Eq. IV-21}$$

$$\Delta^{A_iB_j} = \sqrt{\Delta^{A_iB_i} * \Delta^{A_jB_j}} \qquad \text{Eq.}$$

IV-22

This, however, is the beginning of the complexities of the solution, Eq. III-14 cannot be used directly in calculating vapor-liquid equilibrium since it is not a cubic equation of state. Thus, the reduced Helmholtz version of the CPA EoS is required. Equation III-23 is the equation for fugacity and can use the residual Helmholtz energy to split between the cubic EoS and the associative portion. From [Kontogeorgis and Folas, 2009], the procedure to calculate the fugacity is as follows:

The fugacity is defined as

$$RTln(\hat{\vartheta}_i) = \left(\frac{\partial A^r}{\partial n_i}\right)_{T,V,n} - ln(Z) \qquad \text{Eq. IV-23}$$

$$Z = \frac{PV}{nRT} \qquad \text{Eq. IV-24}$$

$$A^r(T,V,n) = A^R_{cubic}(T,V,n) + A^R_{Association}(T,V,n) \qquad \text{Eq.}$$

IV-25

The full derivation can be found in the book from [Kontogeorgis and Folas, 2010]

$$ln\hat{\vartheta}_i = -ln\left(1 - \frac{B}{V}\right) - n * \left(-\frac{1}{V-B}\right)B_i - \frac{n^2 a_{mix}}{T} * \left(-\frac{\frac{1}{RB}ln\left(1+\frac{B}{V}\right)+V\left(-\frac{1}{RV(V+B)}\right)}{B}\right)B_i -$$

$$\frac{\frac{1}{RB}ln\left(1+\frac{B}{V}\right)}{T}D_i \qquad \text{Eq.}$$

IV-26

where

$$B = \sum_i n_i b_{ii} \qquad \text{Eq. IV-27}$$

$$B_i = \frac{2\sum_j n_j b_{ij} - B}{n} \qquad \text{Eq. IV-}$$

28

$$D_i = 2\sum_j n_j a_{ij} \qquad \text{Eq. IV-29}$$

To determine the fugacity of the associative portion of the CPA Eos, Michelsen and Hendriks have developed a function to determine the derived properties of the association term such as the fugacity [Michelsen and Hendriks, 2001]. This function is called the Q function and is a function of n, T, V, $\varkappa$. This is done by finding the stationary point of the function (a stationary point is where the derivative is zero). The

derivation of the fugacity part can be found in the book from [Kontogeorgis and Folas, 2009].

$$Q_{sp} = \sum_i n_i \sum_{A_i} \left(ln(\chi_{A_i}) - \frac{1}{2}\chi_{A_i} + \frac{1}{2} \right) = \frac{A^r_{association}(T,V,n)}{RT} \qquad \text{Eq. IV-30}$$

$$\frac{\partial}{\partial n_i} \left(\frac{A^r_{association}}{RT} \right)_{T,V,n_j} = \sum_{A_i} \chi_{A_i} - \frac{1}{2}\sum_i n_i \sum_{A_i}(1 - \chi_{A_i})\frac{\partial \ln g}{\partial n_i} \qquad \text{Eq. IV-31}$$

$$\frac{\partial \ln g}{\partial n_i} = 0.475V \left(\frac{1}{V-0.475B} \right)^2 \qquad \text{Eq. IV-32}$$

However, notice that the total system volume is needed, and not the molar volume. This requires an addition procedure, which is the determination of the system volume. The use if the Q function then needed again. From the Q function, it can be derived (see the book from [Kontogeorgis and Folas, 2009]) that the volume can be found by minimizing the following equation:

$$F(V) = P - \left[\frac{nRT}{V} + n\frac{B}{V(V-B)} - \frac{n^2 a_{mix}}{T}\frac{1}{RV(V+B)} - \frac{1}{2V}\left(1 + \right. \right.$$

$$\left. \left. 0.475V^2 \left(\frac{1}{V-0.475B} \right)^2 \right) \sum_i n_i \sum_{A_i}(1 - \chi_{A_i}) \right] \qquad \text{Eq. IV-33}$$

To solve Eq. III.39 a good guess is needed, and the analytical solution to the Cubic EoS is normally used. Assuming that the moles of the system are 1 mole, the corresponding volumes of the vapor and liquid phases can be determined, and this total volume is then used as the initial guess of Eq. III-39. Then the final volume is found by minimizing Eq. III-39 and updating Eq. III-13 on each loop. Then this volume is sent to the Eq. III-30 to find the corresponding fugacities. Once the fugacity of each component is equalized, the

mole fractions of each component are determined and saved. The given terms are the

pressure-temperature and moles of the total mixture; thus, the given pressure and

temperature will be the experimental pressure-temperature data of methane hydrate.

To account for hysteresis, the $\varkappa$ terms are changed so that the residual cages act as

another compound, so the modified version will be Eq. IV-34

$$
\begin{bmatrix}
X_1^A - \dfrac{1}{1 + \rho_l * x_1 * \Delta^{A_1 B_2}(X_1^B + X_1^C + X_1^D)} = 0 \\[4pt]
X_1^B - \dfrac{1}{1 + \rho_l * x_1 * \Delta^{A_1 B_2}(X_1^A + X_1^C + X_1^D)} = 0 \\[4pt]
X_1^C - \dfrac{1}{1 + \rho_l * x_1 * \Delta^{A_1 B_2}(X_1^A + X_1^B + X_1^D)} = 0 \\[4pt]
X_1^D - \dfrac{1}{1 + \rho_l * x_1 * \Delta^{A_1 B_2}(X_1^A + X_1^B + X_1^C)} = 0 \\[4pt]
X_2^A - \dfrac{1}{1 + \rho_l * x_1 * \Delta^{A_1 B_2}(X_1^B + X_1^C + X_1^D) + \rho_l * x_2 * \Delta^{A_2 B_2}(X_2^B + X_2^C + X_2^D)} = 0 \\[4pt]
X_2^B - \dfrac{1}{1 + \rho_l * x_1 * \Delta^{A_1 B_2}(X_1^A + X_1^C + X_1^D) + \rho_l * x_2 * \Delta^{B_2 C_2}(X_2^A + X_2^C + X_2^D)} = 0 \\[4pt]
X_2^C - \dfrac{1}{1 + \rho_l * x_1 * \Delta^{A_1 B_2}(X_1^A + X_1^B + X_1^D) + \rho_l * x_2 * \Delta^{C_2 A_2}(X_2^A + X_2^B + X_2^D)} = 0 \\[4pt]
X_2^D - \dfrac{1}{1 + \rho_l * x_1 * \Delta^{A_1 B_2}(X_1^A + X_1^B + X_1^C) + \rho_l * x_2 * \Delta^{D_2 A_2}(X_2^A + X_2^B + X_2^C)} = 0
\end{bmatrix}
$$

Since hysteresis only occurs in the liquid phase, Eq.34 is only applied to the liquid

phase, while Eq. III-18 and the procedure from Eq. IV-1- IV-34 can be implemented

following the procedure in figure III-11 can be used.

Future Work implementation of CPA and Hydrate model to Hysteresis

The previous section showed the theory and the outline of the CPA EoS and the

proposed model for hysteresis by considering the residual hydrate cages as an additional

component; the next steps are to implement this approach into code and fit the model to

experimental data.